Integrated Quantum Optics: Experiments towards integrated quantum-light sources and quantum-enhanced sensing

Hoff, Ulrich Busk; Andersen, Ulrik Lund

Publication date:
2015

Document Version
Publisher's PDF, also known as Version of record

PhD thesis

Integrated Quantum Optics

Experiments towards integrated quantum-light sources and quantum-enhanced sensing

Ulrich Busk Hoff

M. Sc., University of Copenhagen 2007

A Thesis Submitted in Partial Fulfilment of the Requirements
for the Degree of Doctor of Philosophy in Physics

Department of Physics
Technical University of Denmark

Thesis version 1.0

Ulrich Busk Hoff
Wednesday 8th April, 2015
Kgs. Lyngby, Denmark

Principal supervisor:
Professor Ulrik L. Andersen

Thesis,
submitted: April 8, 2015

To Tina and Bertram,
– a truly classic couple with whom I am deeply entangled.

Integrated quantum optics – experiments towards integrated quantum-light sources and quantum-enhanced sensing.

Abstract The work presented in this thesis is focused on experimental application and generation of continuous variable quantum correlated states of light in integrated dielectric structures. Squeezed states are among the most exploited continuous variable optical states for free-space quantum-enhanced sensing and communication protocols, but for these developments to be applicable for future technologies they must be transformed to an integrated architecture compatible with current electro-optical technology. So far only little work has been done in this direction, but two such contributions are made in this thesis: Firstly, we present proof-of-principle demonstration of interfacing squeezed light with an on-chip optomechanical resonator, demonstrating a quantum-enhanced sensitivity to the vibrations of the micromechanical object. Secondly, work on developing an integrated source of squeezed light is presented and an optimized device design is proposed. The devices have been fabricated and tested optically and preliminary interrogations of the output quantum noise have been performed.

Integreret kvanteoptik – eksperimentelle studier med henblik på generering og anvendelse af kvanteoptiske tilstande i integrerede strukturer.

Dansk resumé Denne afhandling har fokus på eksperimentelle anvendelser og generering af kvantekorrelerede lystilstande i integrerede dielektriske strukturer. Kvantestøjsreducerede tilstande er blandt de hyppigst anvendte til kvanteforstærkede måleteknikker og kommunikationsprotokoller, men en praktisk implementering af sådanne teknikker i kommende teknologi fordrer, at de realiseres i en integreret platform kompatibel med den gængse elektro-optiske fabrikationslinje. Antallet af arbejder med dette fokus er sparsomt, men to sådanne bidrag er indeholdt i nærværende afhandling: Vi har for første gang koblet kvantestøjsreducerede optiske tilstande til en integreret optomekanisk ræsonator, resulterende i en kvanteforstærket måling af et mikromekanisk objekts termisk eksiterede vibrationer. I et særskilt forskningsprojekt har vi arbejdet mod at udvikle en integreret kilde til kvantestøjsreduceret lys, og vi har på baggrund af et omfattende numerisk og teoretisk arbejde fremsat et optimeret design. Optiske mikroræsonatorer er blevet fabrikeret i henhold til designet, og indledende undersøgeler af strukturernes faktiske anvendelighed som kilder til kvantestøjsreducerede optiske tilstande er blevet udført. Dette arbejde er endnu ikke afsluttet.

Acknowledgements

The work presented in this thesis was carried out in the Quantum Physics and Information Technology (QPIT) section at the Institute of Physics, Technical University of Denmark between August 2011 and April 2015, with financial support from The Danish Council for Independent Research (Sapere Aude program).

Under the inspiring, enthusiastic, and kind supervision of section leader Professor Ulrik L. Andersen I have had the pleasure of learning how to become a researcher in the field of experimental quantum optics, and I am deeply grateful to him for taking me on board. I highly appreciate the confidence he has shown in my work, the freedom I have been given to follow own ideas, and the office door that has always been open for questions and advice. My only regret is that a Ph.D study is only three years.

Faced with the task of establishing two completely new experimental activities and taking them towards the research front-line, those three years have indeed often seemed dreadfully short and my own incapabilities discouragingly vast. To my good luck, the QPIT section is characterized by a strong team spirit and an abundance of talented people with the will and ability to teach. I am thankful for all the help that has flown my way from the QPIT as a whole, but a few people deserve particular mentioning:

Throughout my time in QPIT I have enjoyed the friendship and advice of assisting professor Alexander Huck. Despite never working on the same research activities, he has always shown great interest in my project and generously offered his help and guidance.

A warm (and only slightly grumpy) thank you goes to Bo Melholt Nielsen with whom I shared an office and custody over a Moccamaster for the first half of my studies. He was instrumental in establishing a suitable lab infrastructure in the Microlab, which we rigged from scratch for hosting the experimental setup for on-chip squeezed light generation.

When Bo left his postdoc position in the group for a job in industry, his seat was overtaken by Tobias Gehring, who's profound skills in quantum optical experimentation I have profited almost inappropriately from. Being in electronics viz he has been the driving force of a new QPIT era of high quality electronics homebrew, and the essential lineup of electronics developed for my work is entirely thanks to him.

Through my efforts in optomechanics I have had the great pleasure of collaborating with the group of associate professor Warwick Bowen from the University of Queensland, and in particular PhD student Glen I. Harris. He enabled the optomechanics experiments reported on in this thesis by bringing with him a batch of microtoroidal resonators when he visited QPIT in 2011. I learned a lot on optomechanics while he was here, and I earned a good friend too.

For a two months period, over new year 2013-2014, I visited the group of Professor Ian Walmsley at Oxford University. I am thankful to Steve Kolthammer for helping arrange the visit and for sharing his appreciation of NIM logic. Also, I would

like to thank Tim Bartley for teaching me a lot of “good stuff” on ultrafast laser experiments and how to tweak the moody old OPA. Finally, I really enjoyed working together with Thomas Hiemstra on the SFWM source which we still have high hopes for.

Aside from all the good friends and colleagues in science, an absolutely essential driving force throughout my entire thesis work has been the support, care, and love of my wife, Tina. I owe you and Bertram three years of family life and I intend to make that up to you!

List of scientific dissemination

Peer-reviewed journal articles

[1] U. B. Hoff, G. I Harris, L. S. Madsen, H. Kerdoncuff, M. Lassen, B. M. Nielsen, W. P. Bowen, and U. L. Andersen. Quantum-enhanced micromechanical displacement sensitivity, *Optics Letters*, 38(9):1413-1415, 2013.

[2] H. Kerdoncuff, U. B. Hoff, G. I. Harris, W. P. Bowen, and U. L. Andersen. Squeezing-enhanced measurement sensitivity in a cavity optomechanical system, *Annalen der Physik*, 527:107-114, 2015. Special issue: Quantum and Hybrid Mechanical Systems.

[3] U. B. Hoff, B. M. Nielsen, and U. L. Andersen. An integrated source of broadband quadrature squeezed light. *arXiv:quant-ph/1504.01054. Submitted to Optics Express, March 2015*

Peer-reviewed conference contributions

[4] G. Harris, M. Taylor, U. B. Hoff, J. Janousek, V. Daria, J. Knittel, H. Kerdoncuff, B. Hage, U. L. Andersen, H. Bachor, and W. P. Bowen. Squeezed light in optomechanical systems. *Proceedings of Frontiers in Optics*, FW5C.4. Optical Society of America, 2012.

[5] U. B. Hoff, G. I. Harris, L. S. Madsen, H. Kerdoncuff, M. Lassen, B. M. Nielsen, W. P. Bowen, and U. L. Andersen. Squeezing-enhanced optomechanical transduction sensitivity. *Proceedings of the Conference on Lasers and Electro-Optics Europe (CLEO EUROPE) and International Quantum Electronics Conference (IQEC)*. IEEE, 2013.

[6] U. B. Hoff, G. I. Harris, L. S. Madsen, H. Kerdoncuff, M. Lassen, B. M. Nielsen, W. P. Bowen, and U. L. Andersen. Squeezing-enhanced optomechanical transduction sensitivity. *International Conference on Squeezed States and Uncertainty Relations (ICSSUR)*, Nuremberg, 2013.

[7] T. Hiemstra, A. Eckstein, U. Hoff, J. Spring, B. Metcalf, P. Humphreys, T. Bartley, P. L. Mennea, J. C. Gates, P. G. R. Smith, S. Kolthammer, and I. A. Walmsley. Generating telecom-band pure heralded single photons on a silica chip. *Accepted for poster presentation at CLEO/Europe-EQEC 2015.*

Other project presentations

[8] QNLO 2012, Quantum and Nonlinear Optics, summer PhD school, Sandbjerg, Denmark, August 2012 (poster)

[9] DTU Conference, Kgs. Lyngby, Denmark, December 2012 (poster and speed-talk)

Public outreach

[10] U. L. Andersen and U. B Hoff. Kvantefysikere vil revolutionere informationssamfundet. *ForskerZonen, Videnskab.dk*, January 2013. Translated title: Quantum physicists aim to revolutionize the information society.

Contribution to publications

I have been the main contributor to publications **1**, **3**, **5**, and **6**. The work presented in **2** was initiated by me but extended and finalized by H. Kerdoncuff. Publication **4** concerns experimental work which I contributed to, but I did not contribute to the writing. Likewise, I made large contributions to the experimental work presented in **7** but not to the writing. Publication **10** was written with equal contributions from me and Professor U. L. Andersen.

Contents

List of Tables

List of Figures

Preface

The work presented in this thesis has been conducted within the research field of quantum optics, with a particular focus on application and generation of continuous variable squeezed states of light in integrated structures. The work has been divided over two separate research projects, which will be introduced separately in the corresponding Parts II and III of the thesis. Part I constitutes a general introduction to theoretical and experimental concepts in quantum optics, relevant to both projects.

Quantum sensing with cavity optomechanics

The optomechanics experiment was established and the presented work carried out during the first third of my PhD studies. This was primarily done in collaboration with Glen I. Harris (visiting PhD student, Univerversity of Queensland, Brisbane) and Hugo Kerdoncuff (PhD student). Lars S. Madsen (PhD student) assisted on operation of the squeezed light source and Mikael Ø. Lassen (postdoc) and Bo M. Nielsen (postdoc) provided daily supervision of the laboratory work.

The work is presented in Part II and covers the developed theoretical model for squeezing enhanced transduction, the established experimental setup for squeezed-light interfacing of microtoroidal resonators, and obtained proof-of-principle results.

Integrated source of single-mode quadrature squeezed light

The work on establishing the experiment for integrated squeezed light generation covered the last two thirds of my PhD studies, and the first year of work was done in collaboration with Bo M. Nielsen, while Ying-Wei Lu (postdoc) worked on the microfabricational aspect of the project. In the latter part of the work, Tobias Gehring (postdoc) was instrumental in developing detection and servo electronics and Timur Iskhakov (postdoc) made contributions to the optical setup.

The work is presented in Part III and covers basic considerations on the investigated integrated structure, an in-depth numerical and theoretical feasibility study and design identification, experimental characterization of device properties, and a discussion of various quantum optical detection schemes by which the integrated source has been interrogated.

Part I

Elements of quantum optics

Overview

The present Part I of this thesis serves as an introduction to central theoretical and experimental aspects of continuous variable quantum optics, the framework in which the experimental efforts on cavity optomechanics (Part II) and on-chip squeezed light generation (Part III) have been carried out.

Noise is a central topic throughout the thesis and in Chapter 1 we start by briefly discussing the fundamental difference between classical and quantum noise and the implications of noise on measurements in the two realms of physics in general. Taking a more specialized point of view, we then focus our attention on the optical domain. First, the classical description of light is reviewed and we briefly cover the mechanism of optical guiding in dielectric structures, the nonlinear optical Kerr effect, optical modulation, and the concept of sidebands which is central for continuous variable quantum optics. Finally, a discussion of the quantized electromagnetic field is provided, and the field quadratures, which will be our preferred representation of the optical field state throughout this thesis, are introduced.

Chapter 2 introduces a selection of concepts and methods essential for the experimental work presented in later chapters. A particular focus is on description of the various detection techniques for interrogation of optical quantum noise which has been implemented in the experimental setups. Also, the effect of optical loss is discussed, as it presents one of the main challenges to be overcome in conducting experiments with squeezed light and quantum correlated continuous variable states of light in general.

Theoretical concepts 1

> And God said: "$[a, a^\dagger] = 1$. Go forth, be fruitful, and multiply (but don't commute)". And there was light, and quantum noise...
>
> – R. Schoelkopf
> in *Noise and Quantum Measurement* [114]

1.1 Classical and quantum noise

Quantum mechanics is often accused of being confusing, counter intuitive, impossible to grasp... and maybe there is something to it? At least many of the predictions and consequences of quantum mechanics are in contrast to our everyday perception of Nature, adequately described by classical Newtonian physics. One such point of clear distinction between classical and quantum physics is the role of *noise*, which is central to the work presented in this thesis. To highlight the contrast we start by briefly reviewing a number of underlying principles of classical and quantum measurements.

1.1.1 Classical measurement

Classically, a physical system $\mathcal{S}$ can be represented by a set of system variables $\{A, B, C, ...\}$, generally dependent on time and/or other system parameters. The state of the system, representing the observes knowledge, is defined by a set of probability distributions $p(a) = \Pr[A = a]$, describing the probability that variable A has value a. By performing measurements of the system variables the observer gradually improves his knowledge, and conditioned on the measurement outcomes the system state is correspondingly updated via Bayesian inference. In principle, all system variables can be measured simultaneously and with arbitrary precision. And in the case of an *ideal* measurement the outcome is exactly the value of A, say a', leaving the system in a state of maximal knowledge $p(a) = \delta_{a,a'}$ (in case of a discrete variable) about this variable. Performing a set of ideal measurements of all system variables results in complete knowledge about the system. Since in Newtonian physics the evolution of the system, and the whole Universe for that matter, is governed by a set of deterministic equations of motion, complete knowledge about the system at one instant in time can be propagated in time to predict,

with certainty, the state of the system at any future time. Thus, complete knowledge at one time entails complete knowledge at all times. From an experimental point of view, any measurement of a system variable A inevitably involves coupling some sort of apparatus or meter $\mathcal{M}$ to the system and thereby, through a tailored physical process, establishing a correlation between the meter variable Y and the particular system variable. In practice, we are thus limited to indirect measurements of A through observation of the meter variable. Furthermore, the meter is generally prone to technical noise which will introduce uncertainty on the measurement outcome, allowing ideal measurements to be performed only in the academic limit of a perfectly noiseless meter. It is important to note, however, that there is no fundamental limit to the measurement precision and how well the state of a system can be determined. Uncertainties are only introduced through the limited technical abilities of the observer.

1.1.2 Quantum measurement

According to the canonical quantization procedure of Dirac [36], the transition from classical to quantum description of a system is made by replacing the classical representation of observable quantities as canonical conjugate variables $\{X_i, P_j\} = \delta_{ij}$, by conjugate Hermitian Hilbert space operators obeying the canonical commutation relation $[\hat{X}_i, \hat{P}_j] = i\hbar\delta_{ij}$. Also, system states are represented by vectors in Hilbert space $|\phi\rangle$, termed *kets*, which are quantum states of maximal knowledge. Due to their Hermitian property, each observable has a complete set of eigenstates $\{|\psi_i\rangle\}$ enabling spectral decomposition into a diagonal form

$$\hat{A} = \sum_i a_i \hat{\Pi}_i, \tag{1.1}$$

where $\hat{\Pi}_i = |\psi_i\rangle\langle\psi_i|$ is the projector onto the a_i-eigenspace of $\hat{A}$. The spectrum of eigenvalues $\{a_i\}$ – discrete or continuous – are the possible outcomes of a measurement of $\hat{A}$ and the corresponding measurements are described by the collection of projectors $\{\hat{\Pi}_i\}$. For an arbitrary *a priori* state $|\Psi\rangle$ measurement of $\hat{A}$ will yield the result a_i with probability

$$\Pr(a_i) = \langle\Psi|\hat{\Pi}_i|\Psi\rangle, \tag{1.2}$$

projecting the system into the conditional *a posteriori* state

$$|\Psi'\rangle = \frac{\hat{\Pi}_i|\Psi\rangle}{\sqrt{\langle\Psi|\hat{\Pi}_i|\Psi\rangle}}. \tag{1.3}$$

Since any arbitrary state can be expanded on the full set of eigenstates of $\hat{A}$ as $|\Psi\rangle = \sum_i \lambda_i|\psi_i\rangle$ with normalization $\sum_i |\lambda_i|^2 = 1$, the probability of measuring a_i is equivalently given by $\Pr(a_i) = |\lambda_i|^2$. This highlights the inherent probabilistic structure of quantum mechanics, embodied in *Born's rule*, which is in sharp contrast

to classical physics. Quantum mechanics does not allow us to predict with certainty the result of a measurement event but only the probabilities with which a number of possible outcomes will occur. The fact that predictions can only be of a probabilistic character means that questions regarding the outcome of particular measurement events are not allowed. Is it only meaningful to consider probabilities for ensembles of measurements performed on identically prepared systems. Even when the system is prepared in a pure quantum state of maximal knowledge is the outcome of a measurement not uniquely defined in general. This is only the case when the system is prepared in an eigenstate of the measured observable. In all other cases the system is randomly projected into one of the eigenstates of the measured observable – this is commonly termed the *projection postulate of quantum mechanics*.

Knowing the outcome probability (Eq. 1.2) the statistical properties of measurements of $\hat{A}$ can be characterized further by calculating the first and second moments, which in case of Gaussian states provides full characterization. The first and second momenta, mean value and variance, respectively, are given by

$$\langle \hat{A} \rangle = \sum_i a_i \mathrm{Pr}(a_i) = \sum_i a_i \langle \psi | \hat{\Pi}_i | \psi \rangle = \langle \psi | \hat{A} | \psi \rangle \tag{1.4}$$

$$\mathrm{Var}(\hat{A}) = \langle (\hat{A} - \langle \hat{A} \rangle)^2 \rangle = \langle \hat{A}^2 \rangle - \langle \hat{A} \rangle^2. \tag{1.5}$$

Using the spectral decomposition of $\hat{A}$ and the Cauchy-Schwarz inequality it is straightforward to show that $\langle \psi | \hat{A}^2 | \psi \rangle \geq \langle \psi | \hat{A} | \psi \rangle^2$ meaning that in general, $\mathrm{Var}(\hat{A}) \geq 0$, even for a state of maximal knowledge. This is a truly quantum feature, known as projection noise or *quantum noise*, clearly in contrast to classical physics.

1.1.3 The Heisenberg uncertainty relation

A related and very important aspect of quantum measurements is the simultaneous measurability of observables. In order for two observables $\hat{A}$ and $\hat{B}$ to be simultaneously measurable for a given state $|\psi\rangle$ the a posteriori state should be independent of the order in which the measurements are performed, meaning that the conditional state should be a common eigenstate for the two observables, for all possible measurement outcomes. This is equivalent to the requirement that there exist an orthonormal basis with respect to which both $\hat{A}$ and $\hat{B}$ are diagonal, for which a necessary and sufficient condition is that the two observables commute, $[\hat{A}, \hat{B}] = 0$. In general, simultaneous measurements are constrained by the relation [94]

$$|\langle \psi | [\hat{A}, \hat{B}] | \psi \rangle|^2 \leq 4 \langle \psi | \hat{A}^2 | \psi \rangle \langle \psi | \hat{B}^2 | \psi \rangle \tag{1.6}$$

To clarify the impact of this constraint on the fluctuations of measurement outcomes, we substitute the observables by their fluctuation parts, $\delta \hat{A} = \hat{A} - \langle \hat{A} \rangle$. Using the above expression for the variance and the fact that the mean values are classical commuting quantities leads to the familiar form of *Heisenberg's uncertainty relation*

$$\mathrm{Var}(\hat{A}) \cdot \mathrm{Var}(\hat{B}) \geq \frac{|\langle [\hat{A}, \hat{B}] \rangle|^2}{4}, \tag{1.7}$$

quantifying the ultimate precision for simultaneous measurements of non-commuting observables.

1.2 Classical description of light

Taking a step back, we will in the following review the classical description of light propagation in dielectric media. Well aware that the contents of this Section is already covered in much finer detail in a broad range of textbooks, e. g. [64, 22, 90], it has been included, nevertheless, motivated by the intension of making the present thesis a self-contained presentation of the field within which the work has been conducted.

1.2.1 Maxwell's equations

The classical description of light, and propagating electromagnetic fields in general, is fully captured by *Maxwell's equations*. In the present thesis we will only be concerned with light propagation in vacuum and dielectric media, containing no free charges and no free currents, and furthermore, we assume that the materials are non-magnetic. In this case Maxwell's equations take the simplified form:

$$\nabla \times \mathbf{E} = -\frac{\partial \mathbf{B}}{\partial t}, \qquad \nabla \times \mathbf{H} = \frac{\partial \mathbf{D}}{\partial t}, \tag{1.8}$$

$$\nabla \cdot \mathbf{D} = 0, \qquad \nabla \cdot \mathbf{B} = 0, \tag{1.9}$$

where $\mathbf{E}$ and $\mathbf{H}$ are the electric and magnetic field amplitude vectors, and $\mathbf{D}$ and $\mathbf{B}$ are the electric and magnetic flux densities. The field amplitudes and flux densities are related by the constitutive equations

$$\mathbf{D} = \epsilon_0 \mathbf{E} + \mathbf{P}, \qquad \mathbf{B} = \mu_0 \mathbf{H}, \tag{1.10}$$

where $\mathbf{P}$ is the induced electric polarization, ϵ_0 the vacuum permittivity, and μ_0 the magnetic permeability of free space. The polarization captures the response of a medium to the applied electric field, and we will return to that shortly. For now, however, it will suffice to say that the polarization vector consists of parts both linear and nonlinear in the applied field strength, and that the two can be conveniently separated by invoking the lumped notation $\mathbf{P} = \mathbf{P}^{(1)} + \mathbf{P}^{\mathrm{NL}}$. Here $\mathbf{P}^{(1)} = \epsilon_0 \chi^{(1)} \mathbf{E}(t)$ is the linear contribution and the higher-order terms are denoted by the collective quantity $\mathbf{P}^{\mathrm{NL}}$. In the following, we will only be concerned with fields propagating in a linear medium, and we further assume the medium to be isotropic and lossless such that the permittivity can be regarded as a scalar quantity, $\epsilon(\omega) \in \mathbb{R}$. By including the frequency dependence we allow for dispersion in the material. In this case $\mathbf{D} = \epsilon_0 \epsilon_r(\omega) \mathbf{E}$.

The electric and magnetic fields can be determined by a vector potential $\mathbf{A}(\mathbf{r}, t)$ as

$$\mathbf{B} = \nabla \times \mathbf{A}, \qquad \mathbf{E} = -\frac{\partial \mathbf{A}}{\partial t}. \tag{1.11}$$

Invoking the Coulomb gauge condition $\nabla \cdot \mathbf{A} = 0$, it is straightforward[1] to show that the vector potential satisfies the wave equation

$$\nabla^2 \mathbf{A} - \frac{n^2(\omega)}{c^2} \frac{\partial^2 \mathbf{A}}{\partial t^2} = 0, \tag{1.12}$$

where we have defined the speed of light in vacuum $c = 1/\sqrt{\epsilon_0 \mu_0}$ and used that the refractive index is given by $n(\omega) = \sqrt{\epsilon_r(\omega)} = \sqrt{1 + \chi^{(1)}(\omega)}$. Following [90] the vector potential can be Fourier expanded in terms of plane wave modes as

$$\mathbf{A}(\mathbf{r}, t) = \mathcal{A}_0 \sum_{\mathbf{k}} \boldsymbol{\alpha}_{\mathbf{k}}(t) e^{i\mathbf{k}\cdot\mathbf{r}}, \tag{1.13}$$

where $\boldsymbol{\alpha}_{\mathbf{k}}(t)$ is a dimensionless amplitude, $\mathcal{A}_0 = (\epsilon_0 n^2(\omega_k) V)^{-1/2}$ a normalization constant, and V the expansion volume. Also, we have defined the wavevector $|\mathbf{k}| = n(\omega_k) \cdot \omega_k / c = 2\pi/\lambda$, where λ is the wavelength in the medium. Inserting (1.13) into (1.12) we find that the plane wave amplitudes are given by the harmonic oscillator equation

$$\left[\frac{\partial^2}{\partial t^2} + \omega_k^2 \right] \boldsymbol{\alpha}_{\mathbf{k}}(t) = 0, \tag{1.14}$$

which has solution

$$\boldsymbol{\alpha}_{\mathbf{k}}(t) = \sum_{s=1}^{2} \mathbf{p}_{\mathbf{k},s} \left[\alpha_{\mathbf{k},s} e^{-i\omega_k t} + \alpha^*_{-\mathbf{k},s} e^{i\omega_k t} \right]. \tag{1.15}$$

The vector part of the amplitude is decomposed in terms of unit polarization vectors $\mathbf{p}_{\mathbf{k},s}\,(s = 1, 2)$ forming an orthonormal basis, $\mathbf{p}_{\mathbf{k},s} \cdot \mathbf{p}_{\mathbf{k},s'} = \delta_{ss'}$, and satisfying the transversality condition $\mathbf{k} \cdot \mathbf{p}_{\mathbf{k},s} = 0$. Substituting (1.15) into (1.13) we get the expansion

$$\mathbf{A}(\mathbf{r}, t) = \mathcal{A}_0 \sum_{\mathbf{k}} \sum_{s=1}^{2} \mathbf{p}_{\mathbf{k},s} \left[\alpha_{\mathbf{k},s} e^{i(\mathbf{k}\cdot\mathbf{r} - \omega_k t)} + \alpha^*_{\mathbf{k},s} e^{-i(\mathbf{k}\cdot\mathbf{r} - \omega_k t)} \right]. \tag{1.16}$$

Using (1.11) the multimode plane wave expansion of the electric field is given by

$$\mathbf{E}(\mathbf{r}, t) = i\mathcal{E}_0 \sum_{\mathbf{k}} \sum_{s=1}^{2} \mathbf{p}_{\mathbf{k},s} \left[\alpha_{\mathbf{k},s} e^{i(\mathbf{k}\cdot\mathbf{r} - \omega_k t)} - \alpha^*_{\mathbf{k},s} e^{-i(\mathbf{k}\cdot\mathbf{r} - \omega_k t)} \right], \tag{1.17}$$

and from the determining relation for $\mathbf{B}$ in (1.11) a similar expression for the magnetic field can be derived. Since the light-matter interactions of relevance to the present thesis exclusively involves coupling through the electric field, we will not

[1] It deserves mentioning that in deriving (1.12) we have also assumed that ϵ is homogeneous, or more specifically that $\nabla\epsilon = 0$. For a guided wave, as will be discussed in the following, this is obviously not true, since it is exactly the spatial variation in ϵ that provides the guiding mechanism.

devote further attention to the magnetic field and henceforth we will describe light solely in terms of the electric field vector.

In continuous wave (cw) experiments, as we are concerned with in this thesis, the optical field is commonly described by a monochromatic single mode with frequency $\omega_{k'}$, given by just a single term in the $\mathbf{k}$-sum in (1.17). The amplitude $\alpha_{\mathbf{k},s}$ describes the spectral envelope of the mode, and in the case of a strictly monochromatic wave it reduces to $\alpha_{\mathbf{k},s} = \delta(\omega_k - \omega_{k'})$. This is of course unphysical, as the Fourier transform time-bandwidth relation requires such a wave to have an infinite duration, but nonetheless it is good approximation that conveniently simplifies the description.

1.2.2 Spatial modes and guided-wave propagation

According to (1.17) the energy of the light field is generally distributed over a number of spatially distinct modes described by mode functions $u_{\mathbf{k},s}(\mathbf{r}) = \mathcal{E}_0 \mathbf{p}_{\mathbf{k},s} e^{i\mathbf{k}\cdot\mathbf{r}}$. From an experimental point of view, it is of great importance to know and control the number of involved modes and most often it is desired to constrain the field to just a single mode – usually the fundamental one. This is so because unintentional coupling to higher-order modes is associated with optical loss.

Inserting (1.16) into (1.12) it is readily seen that each mode function satisfies the Helmholtz equation

$$\left[\nabla^2 + k_0^2 n^2(\omega_k)\right] u_{\mathbf{k},s}(\mathbf{r}) = 0, \tag{1.18}$$

where $k_0 = 2\pi/\lambda_0$ is the free-space wave number. In a homogeneous medium the vector components of the electric field are uncoupled, and in this case the Helmholtz equation can be solved for the individual field components. Assuming further that the transverse mode is slowly varying in the propagation direction, such that the paraxial approximation can be assumed, stable solutions for the mode function are e.g. the common Gaussian beam families, Hermite-Gaussian and Laguerre-Gaussian modes [75]. Throughout the experimental work conducted during this thesis, free-space modes were always prepared in the fundamental TEM_{00} mode.

Things are more involved in the case of guided wave propagation in optical fibers and waveguides, where guidance is provided by spatial inhomogeneity of the medium, and particularly so in the case of strong guidance. The guiding property of fibers and waveguides can be understood in terms of total internal reflection at the interface between two dielectric materials with different refractive indices. From a simplistic ray-optics point of view, *Snell's law* and the *Law of reflection*,

$$n_1 \sin\theta_i = n_2 \sin\theta_e, \qquad \theta_i = \theta_r, \tag{1.19}$$

cf. Fig. 1.1(a), directly provides a condition for total internal reflection of a ray propagating in the high-index core medium (n_1) incident on the interface to the low-index cladding medium (n_2): setting the exit angle to $\theta_e = 90°$ yields

$$\theta_i^c = \sin^{-1}\left(\frac{n_2}{n_1}\right). \tag{1.20}$$

For angles of incidence θ_i larger than the critical angle θ_i^c total internal reflection of the ray will occur, and the ray will be reflected off the interface at an angle $\theta_r = \theta_i$, relative to the interface normal. Real solutions to (1.20) only exist for $n_1 > n_2$, meaning that the ray should be incident on the interface from the high-index side. This suggests a visualization of the guided field as a ray repeatedly undergoing total internal reflections as it propagates down the guiding structure, as illustrated in Fig. 1.1(b). Similarly, the whispering gallery modes of optical microresonators can be understood in terms of total internal reflection under a gracing angle at the dielectric-air interface, resulting in a highly localized optical field at the interface, Fig. 1.1(c).

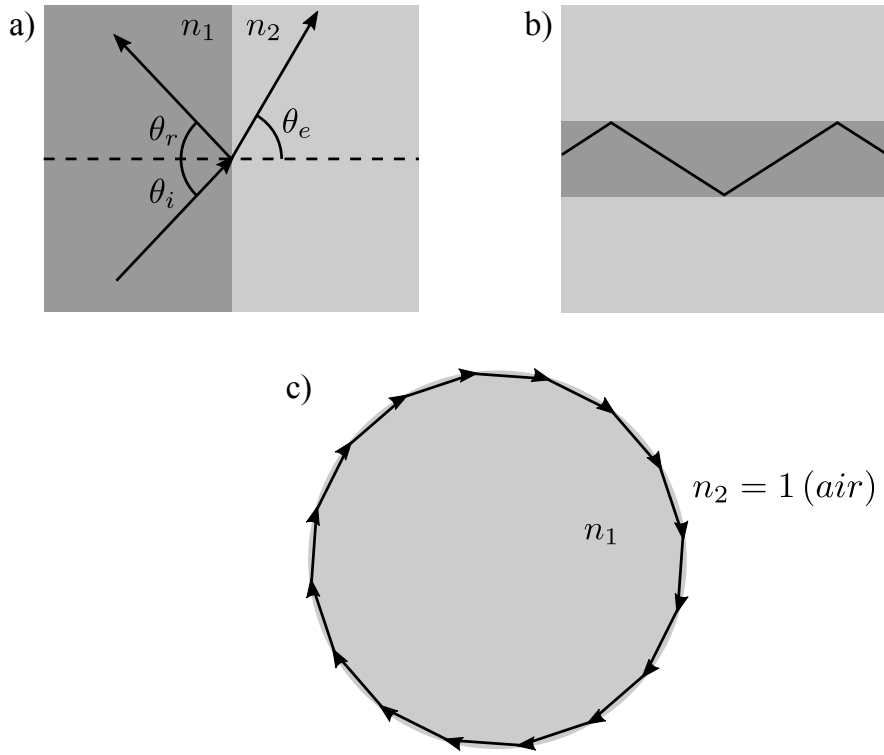

Figure 1.1: (a) For a ray incident on a dielectric interface from the high-index side ($n_1 > n_2$) under an angle of incidence θ_i, part of the ray will be refracted into the low-index medium at an angle θ_e, while another part is reflected back into the high-index medium at an angle $\theta_r = \theta_i$. (b) The guiding property of an inhomogeneous dielectric medium can be understood in terms of repeated total internal reflections of rays inside the high-index region, for which the angle of incidence is larger than the critical angle for the particular interface. (c) In microresonators, total internal reflection at the dielectric-air interface, under a gracing angle of incidence, leads to formation of whispering gallery modes that are highly localized at the interface.

Though providing an intuitive understanding this picture is, however, an over-simplified description of the guiding mechanism. As an illustration of it's inadequacy

we note that according to the above reasoning a continuum of modes should be supported by the waveguide, corresponding to all rays with $\theta_i > \theta_i^c$. Experience from the lab immediately tells us that this is incorrect. The actual *discrete* spectrum of supported modes is a consequence of self-consistency, requiring that the total phase shift experienced by the reflected field as it zig-zigs down that guide exactly equals a multiple of 2π for a full reflection cycle [74]. This results in a transverse resonance condition, and in the two-dimensional case of a rectangular waveguide, finding the allowed modes amounts to solving the eigenvalue problem given by the Helmholtz equation. The sought-for eigenvalues are the propagation constants $\beta = k_0 n_{eff}$ of the guided modes, where n_{eff} is the effective mode index, and the possible values are bounded by the refractive indices of the guiding structure, $k_0 n_2 < k_0 n_{eff} < k_0 n_1$. Finding the eigenmodes is in general a non-trivial task, and in order to do so we will resort to numerics as described in Section 11.1.

1.2.3 Nonlinear optics

In the previous sections we considered, for clarity, only light propagation in linear media. However, the nonlinear optical response exhibited by certain materials is of uttermost importance to the work presented in this thesis, as it is the mechanism by which the quantum noise properties of light can be manipulated experimentally.

In general the j'th component of the polarization vector $\mathbf{P}$ is given by a Taylor expansion in the electric field amplitude:

$$P_j = \epsilon_0 \left[\sum_k \chi^{(1)}_{jk} E_k + D^{(2)} \sum_{k,l} \chi^{(2)}_{jkl} E_k E_l + D^{(3)} \sum_{k,l,m} \chi^{(3)}_{jklm} E_k E_l E_m + ... \right], \qquad (1.21)$$

where the three first terms included here describe linear response, second order nonlinearity, and third order nonlinearity. The expansion coefficients $\chi^{(n)}$ are the susceptibility tensors of rank $n+1$ describing mixing of n fields, in general oscillating at different frequencies. A common notation, explicitly showing the frequency dependence of the susceptibility is (for the third-order term) $\chi^{(3)}_{jklm}(-\omega_4; \omega_1, \omega_2, \omega_3)$, describing generation of a polarization component oscillating at $\omega_4 = \omega_1 + \omega_2 + \omega_3$ due to mixing of fields $E(\omega_1)$, $E(\omega_2)$, and $E(\omega_3)$. The factor $D^{(n)}$ accounts for possible degeneracies among the interacting fields, taking the values:

$$D^{(2)} = \begin{cases} 1 & \text{for indistinguishable fields} \\ 2 & \text{for distinguishable fields} \end{cases} \qquad (1.22)$$

$$D^{(3)} = \begin{cases} 1 & \text{all fields indistinguishable} \\ 3 & \text{two fields indistinguishable} \\ 6 & \text{all fields distinguishable} \end{cases} \qquad (1.23)$$

Observation of nonlinear optical response from a media generally requires a very strong driving electromagnetic field and thus the effects are not observable in everyday life. But in an experimental setting the combination of specifically selected

materials and the high optical intensity available by laser sources can indeed lead to significant effects. When driven sufficiently hard, the perturbation of the electron cloud in the material, constituting the induced polarization, is so large that it causes the electrons to oscillate at frequencies other than the driving one and the polarization becomes a source for new frequency components. For non-centrosymmetric crystals exhibiting a second order nonlinearity (second term in (1.21)) one possible consequence is *parametric down-conversion* in which a photon from the driving field at frequency ω_p is converted into two photons at $\omega_p/2$. This process is the underlying one for most common sources of squeezed light, including the one exploited for the experiments described in Part II. For centrosymmetric materials the lowest non-vanishing nonlinearity is of third order (third term in (1.21)) and such materials are generally known as Kerr media.

Kerr media

As mentioned, the underlying mechanism for nonlinear optical effects in Kerr media is the third order tensor susceptibility $\chi^{(3)}_{ijkl}$, supporting a great variety of four-photon mixing processes, collectively termed *four-wave mixing* (FWM). In general, FWM processes involve conversion of two pump photons at ω_p into a pair of photons at signal and idler frequencies ω_s and ω_i, respectively, with the convention that $\omega_s > \omega_i$. The interacting field frequencies are related by $2\omega_p = \omega_s + \omega_i$, required by energy conservation, and in order for the process to occur efficiently the phase matching condition $\Delta\beta = 2\beta_p - \beta_s - \beta_i \approx 0$ must be fulfilled; here expressed in terms of the guided mode propagation constants $\beta_i = n_{eff}(\omega_i)k_{0,i}$ where n_{eff} is the effective mode index. For this reason, the dominant interaction is the intrinsically phase matched *self-phase modulation* (SPM) process[2] corresponding to the case of complete degeneracy of the partaking fields and resulting in an intensity dependent refractive index $n(I) = n_0 + n_2 I$. In this case the pump field experiences a self-induced phase shift $\phi_{nl} = 2\pi n_2 IL/\lambda = \gamma_{nl} L P_p$ over a propagation length L, where $\gamma_{nl} = \omega n_2/cA_{eff}$ is the nonlinear parameter, A_{eff} the effective mode area, and P_p the pump power. It is well-known that this type of FWM is capable of generating self-induced single-mode squeezing [10, 118] and it is also the interaction of interest in Part III of this thesis, covering recent work on developing integrated resonant systems for squeezed-light generation. However, in the context of nonlinear optics in integrated resonators a more commonly discussed interaction is *non-degenerate four-wave mixing* (NDFWM) where an intense pump field interacts with two or a multiple of weaker non-degenerate signal and idler fields, each of the fields being resonant on separate longitudinal resonator modes. Parametric oscillators [83, 103] and Kerr-frequency combs [55] have previously been demonstrated using this interaction, and generation of squeezing, both below and above threshold, is discussed in [63].

[2] Unfortunately, there is a large ambiguity in the nomenclature of third order processes in the literature, e.g. terms *optical Kerr effect*, *degenerate four-wave mixing*, and *self-phase modulation* are used synonymously. Here the latter is adopted to highlight the single mode nature of the interaction.

1.3 Modulation and sidebands

An ideal monochromatic continuous wave laser beam is just a sinusoidal signal with constant amplitude and a cyclic phase, but as soon as modulations are introduced on the beam, information can be encoded and carried optically. The ability to encode an decode information on light via modulation and demodulation is the backbone of continuous variable optical communication – both classical and quantum – and it is central to the experimental work presented in Parts II and III of this thesis.

Modulating a signal in general means that a particular time dependence $f(t)$ is deliberately imposed on the signal amplitude or phase, or both, resulting in the information contained in f being copied over to the signal. In the following we will study, how exactly information is encoded through amplitude and phase modulations.

1.3.1 Amplitude and phase modulation

Consider a classical monochromatic optical laser beam represented by $E(t)e^{i\omega_c t}$ where ω_c is the carrier frequency and E a slowly-varying envelope. Amplitude modulation (AM) of the beam introduces a sinusoidal time dependence to the amplitude E which can be expressed as

$$\begin{aligned} E_{AM}(t) &= E(t)(1+\xi\sin(\Omega t))e^{i\omega_c t} \\ &= E(t)\left(e^{i\omega_c t} + \frac{\xi}{2i}e^{i(\omega_c+\Omega)t} - \frac{\xi}{2i}e^{i(\omega_c-\Omega)t}\right), \end{aligned} \tag{1.24}$$

where Ω and ξ are the modulation frequency and depth, respectively. We observe, that as a consequence of the modulation, new frequency components oscillating at $\omega_c \pm \Omega$ are generated. Those are the modulation induced upper and lower sidebands.

In an analogous way, phase modulation introduces a time dependence of the form $\xi\sin(\Omega t)$ to the optical phase,

$$\begin{aligned} E_{PM}(t) &= E(t)e^{i(\omega_c t+\xi\sin(\Omega t))} \\ &\approx E(t)e^{i\omega_c t}(1+i\xi\sin(\Omega t)) \\ &= E(t)\left(e^{i\omega_c t} + \frac{\xi}{2}e^{i(\omega_c+\Omega)t} - \frac{\xi}{2}e^{i(\omega_c-\Omega)t}\right), \end{aligned} \tag{1.25}$$

where in the second step we have used that the modulation depth is usually very small, $\xi \ll 1$. Again, we observe that the modulation leads to creation of sidebands at the modulation frequency, relative to the carrier, but this time the relative phase between carrier and upper (lower) sideband is shifted by $\pi/2$ ($-\pi/2$), compared to amplitude modulation. A representation of the modulated field that will be helpful in later parts of the thesis, is to visualize the field components in a spectrally resolved phase space (see Fig. 1.2) where each frequency component is resolved into its time dependent amplitude and phase quadratures. In doing so, we assume that the field

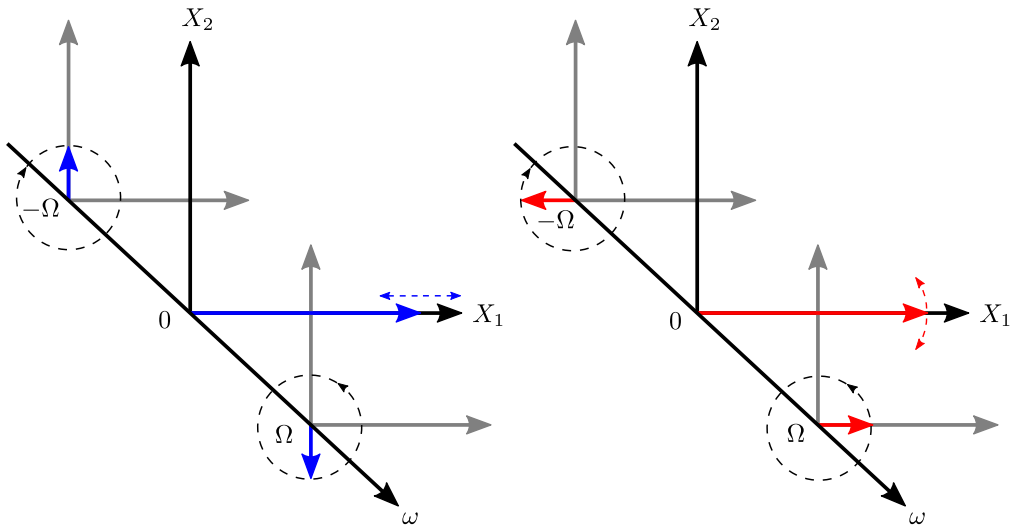

Figure 1.2: Phase space representation of amplitude and phase modulation sidebands in a frame rotating at the carrier frequency. The temporal evolution of the individual components are indicated with dashed arrows. In the case of amplitude modulation (left) the relative phase of the sideband components is such that their vector sum has a harmonically varying component along the amplitude quadrature while the phase quadrature component is always zero. Due to the $\pm\pi/2$ phase shift the result is exactly the opposite for phase modulation (right).

dynamics is transformed into a frame rotating at the optical carrier frequency. This eliminates the free evolution of the carrier, while the upper (lower) sideband rotates in counter-clockwise (clockwise) direction.

1.4 Quantum description of light

As outlined in Section 1.1.2, the quantum mechanical counterpart of a classical representation can be derived via the canonical quantization procedure. In the previous treatment of the classical electromagnetic field we have seen that the field mode amplitudes $\alpha_k(t)$ satisfy the harmonic oscillator equation of motion, suggesting that individual field modes should be quantized in terms of quantum mechanical harmonic oscillators [110]. However, as a cautious remark, simply substituting the complex amplitudes with operators would be against the canonical quantization procedure since the classical mode amplitudes – being complex quantities – do not represent physical observables. Furthermore, the canonical quantization procedure builds on the Hamiltonian formulation of classical mechanics in which the system dynamics is governed by the Hamiltonian, representing the total energy of the system. A quantum mechanical representation of the electromagnetic field should therefore be deduced from the quantized field energy rather than head-over-heals replacing the mode amplitudes by operators. We will not spend more time on the

details of quantization but without further ado simply state the quantized analog of the classical electric field vector (1.17), which can be found in most quantum optics textbooks, e.g. [90, 44]:

$$\hat{\mathbf{E}}(\mathbf{r},t) = i\sum_{\mathbf{k}}\sum_{s=1}^{2}\sqrt{\frac{\hbar\omega_k}{2\epsilon_0 n^2(\omega_k)V}}\mathbf{p}_{\mathbf{k},s}\left[\hat{a}_{\mathbf{k},s}e^{i(\mathbf{k}\cdot\mathbf{r}-\omega_k t)} - \hat{a}^\dagger_{\mathbf{k},s}e^{-i(\mathbf{k}\cdot\mathbf{r}-\omega_k t)}\right]. \tag{1.26}$$

Here $\hat{a}_{\mathbf{k},s}$ and $\hat{a}^\dagger_{\mathbf{k},s}$ are the non-Hermitian annihilation and creation operators for the k'th mode, satisfying the bosonic commutation relations [26]

$$[\hat{a}_{\mathbf{k},s}, \hat{a}^\dagger_{\mathbf{k}',s'}] = \delta_{\mathbf{k}\mathbf{k}'}\delta_{ss'}, \tag{1.27}$$

$$[\hat{a}_{\mathbf{k},s}, \hat{a}_{\mathbf{k}',s'}] = 0, \tag{1.28}$$

$$[\hat{a}^\dagger_{\mathbf{k},s}, \hat{a}^\dagger_{\mathbf{k}',s'}] = 0. \tag{1.29}$$

The total field energy is given by the Hamiltonian operator

$$\hat{H} = \sum_{\mathbf{k}}\sum_{s=1}^{2}\hbar\omega_k\left[\hat{a}^\dagger_{\mathbf{k},s}\hat{a}_{\mathbf{k},s} + \frac{1}{2}\right], \tag{1.30}$$

where $\hat{n}_{\mathbf{k}s} = \hat{a}^\dagger_{\mathbf{k},s}\hat{a}_{\mathbf{k},s}$ is the number operator, counting the number of photons in the $\{\mathbf{k}s\}$-mode. The constant term accounts for the energy of the vacuum fluctuations which are a direct consequence of (1.27).

1.4.1 Field quadratures

Being non-Hermitian, the annihilation and creation operators are not measurable themselves, but their real and imaginary parts are. This leads to the definition of amplitude $\hat{X}_1$ and phase $\hat{X}_2$ quadrature operators for each individual field mode

$$\hat{X}_1 = \hat{a} + \hat{a}^\dagger, \tag{1.31}$$

$$\hat{X}_2 = -i(\hat{a} - \hat{a}^\dagger), \tag{1.32}$$

which are obviously Hermitian. Furthermore, it is useful to define a generalized quadrature as an arbitrary linear combination of the above two

$$\hat{X}_\theta = \hat{a}e^{-i\theta} + \hat{a}^\dagger e^{i\theta} = \hat{X}_1\cos\theta + \hat{X}_2\sin\theta. \tag{1.33}$$

The commutator for the amplitude and phase quadratures has the canonical form

$$[\hat{X}_1, \hat{X}_2] = 2i, \tag{1.34}$$

and for this reason they are commonly considered as the electric field equivalents to the canonical position and momentum operators of the quantum harmonic oscillator.

From (1.7) the uncertainty relation between the quadratures is given by

$$\mathrm{Var}(\hat{X}_1)\cdot\mathrm{Var}(\hat{X}_2) \geq 1, \tag{1.35}$$

with the equality corresponding to *minimum uncertainty states.*

1.4.2 Operator linearization

In describing quantum mechanically the fluctuations of a bright field, we will find it convenient to separate the field operator into a mean value component $\langle\hat{a}\rangle = \alpha$, given by the classical field mode amplitude, and a noise operator $\delta\hat{a}$ with $\langle\delta\hat{a}\rangle = 0$, such that [56, 11]

$$\hat{a}(t) = \alpha + \delta\hat{a}(t). \tag{1.36}$$

The assumption of a bright state means that the carrier amplitude α is much larger than any fluctuations or modulations represented by the noise operator. Thus it is justified to neglect any terms of second order and higher in the fluctuations in calculating operator products, resulting in a linearized description of quantum noise. For example:

$$\begin{aligned}\hat{n} &= \hat{a}^\dagger(t)\hat{a}(t) \\ &= \left(\alpha + \delta\hat{a}^\dagger(t)\right)\left(\alpha + \delta\hat{a}(t)\right) \\ &= \alpha^2 + \alpha\left(\delta\hat{a}^\dagger(t) + \delta\hat{a}(t)\right) + \delta\hat{a}^\dagger(t)\delta\hat{a}(t) \\ &= \alpha^2 + \alpha\delta\hat{X}_1(t),\end{aligned} \tag{1.37}$$

where we have arbitrarily assumed α to be real and defined the amplitude fluctuation quadrature as in Section 1.4.1.

The above separation of the field oparator leads to a convenient phase space visualization of quantum states, often termed *the ball-on-stick picture*, where the mean value is represented by a vector in phase space and the fluctuations are included as a ball with diameter corresponding to the state fluctuations, positioned at the tip of the vector.

1.4.3 Sideband representation

As described in details in [79], the above linearization allows for establishing a Fourier space correspondence between the quantum mechanical annihilation and creation operators and the classical upper and lower sidebands, respectively. In Section 1.3 we have seen that classical modulation of a carrier results in creation of upper and lower sidebands, and in general any modulation can be decomposed into amplitude and phase modulation. Justified by the established correspondence we transfer this picture to the quantum regime describing quantum noise in terms of a continuum of uncorrelated fluctuating sidebands. Thus, we represent the linearized field operator (1.36) as the sum of a carrier component at frequency ω_c and fluctuating sideband modes at frequencies $\pm\Omega$ relative to the carrier:

$$\hat{a}(t) = \alpha e^{i\omega_c t} + \frac{1}{\sqrt{2}}\left(\delta\hat{a}_- e^{i(\omega_c-\Omega)t} + \delta\hat{a}_+ e^{i(\omega_c+\Omega)t}\right). \tag{1.38}$$

The individual sideband fluctuation operators obey the canonical boson commutation relations $[\delta\hat{a}_\pm, \delta\hat{a}_\pm^\dagger] = 1$, and the introduced factor of $1/\sqrt{2}$ ensures that it is

also maintained for $\hat{a}(t)$. Using (1.38) the number operator takes the form

$$\hat{n}(t) = \hat{a}^\dagger(t)\hat{a}(t) \tag{1.39}$$

$$= \alpha^2 + \frac{\alpha}{\sqrt{2}}\left(\delta\hat{a}_+ e^{i\Omega t} + \delta\hat{a}_- e^{-i\Omega t} + \delta\hat{a}_+^\dagger e^{-i\Omega t} + \delta\hat{a}_-^\dagger e^{i\Omega t}\right) \tag{1.40}$$

$$= \alpha^2 + \frac{\alpha}{\sqrt{2}}\left(\delta\hat{a}_+ e^{i\Omega t} + \delta\hat{a}_+^\dagger e^{-i\Omega t}\right) + \frac{\alpha}{\sqrt{2}}\left(\delta\hat{a}_- e^{-i\Omega t} + \delta\hat{a}_-^\dagger e^{i\Omega t}\right) \tag{1.41}$$

$$= \alpha^2 + \frac{\alpha}{\sqrt{2}}\left(\delta\hat{X}_1^+ \cos(\Omega t) - \delta\hat{X}_2^+ \sin(\Omega t)\right) + \frac{\alpha}{\sqrt{2}}\left(\delta\hat{X}_1^- \cos(\Omega t) + \delta\hat{X}_2^- \sin(\Omega t)\right) \tag{1.42}$$

$$= \alpha^2 + \frac{\alpha}{\sqrt{2}}\Big[\left(\delta\hat{X}_1^+ + \delta\hat{X}_1^-\right)\cos(\Omega t) + \left(\delta\hat{X}_2^- - \delta\hat{X}_2^+\right)\sin(\Omega t)\Big], \tag{1.43}$$

from which we observe that fluctuations in the photon number at frequency Ω appears as a consequence of simultaneous beating of the carrier with each of the upper and lower sidebands at the particular frequency. Comparing with (1.37) we see that this is exactly equal to the amplitude quadrature fluctuations:

$$\delta\hat{X}_1(t) = \frac{\left(\delta\hat{X}_1^+ + \delta\hat{X}_1^-\right)}{\sqrt{2}}\cos(\Omega t) + \frac{\left(\delta\hat{X}_2^- - \delta\hat{X}_2^+\right)}{\sqrt{2}}\sin(\Omega t) \tag{1.44}$$

In general, any arbitrary quadrature fluctuations can be found by considering the case where the carrier is phase shifted by θ relative to the sidebands, yielding

$$\delta\hat{X}_\theta(t) = \frac{\left(\delta\hat{X}_\theta^+ + \delta\hat{X}_\theta^-\right)}{\sqrt{2}}\cos(\Omega t) + \frac{\left(\delta\hat{X}_{\theta-\pi/2}^+ + \delta\hat{X}_{\theta+\pi/2}^-\right)}{\sqrt{2}}\sin(\Omega t). \tag{1.45}$$

From the usual definition of the spectral variance $\mathrm{Var}(O(\Omega)) = \left\langle |O(\Omega)|^2 \right\rangle_T$ we find

$$\mathrm{Var}(\delta\hat{X}_\theta(\Omega)) = \frac{1}{4}\Big[\mathrm{Var}\left(\delta\hat{X}_\theta^+ + \delta\hat{X}_\theta^-\right) + \mathrm{Var}\left(\delta\hat{X}_{\theta-\pi/2}^+ + \delta\hat{X}_{\theta+\pi/2}^-\right)\Big]. \tag{1.46}$$

If the upper and lower sidebands are uncorrelated, e.g. for a coherent state, the normalized quadrature variance is recovered, $\mathrm{Var}(\delta\hat{X}_\theta(\Omega)) = 1$.

1.4.4 Quantum states of light

Having quantized the electromagnetic field we now turn to a brief introduction of a number of quantum optical states that are essential to the work presented in later chapters. A phase space illustration of the states is given in Fig. 1.3.

Fock states

A primary example is the energy eigenstates of the field Hamiltonian, which are equivalently eigenstates of the individual single mode number operators. The defining relations are

$$\hat{n}|n\rangle = n|n\rangle, \qquad \langle n'|n\rangle = \delta_{n'n}, \qquad \sum_n |n\rangle\langle n| = 1, \tag{1.47}$$

where the eigenvalue n is the number of excitations (photons) in the mode. This class of states is known as number states or Fock states. The action of the annihilation and creation operators on the number states is,

$$\hat{a}|n\rangle = \sqrt{n}|n-1\rangle, \qquad \hat{a}^\dagger|n\rangle = \sqrt{n+1}|n+1\rangle, \qquad |n\rangle = \frac{(\hat{a}^\dagger)^n}{\sqrt{n!}}|0\rangle, \tag{1.48}$$

where the important *vacuum state* $|0\rangle$ is defined by

$$\hat{a}|0\rangle = 0. \tag{1.49}$$

The fluctuations of the quantum vacuum state – which does not contain any photons – pose a fundamental limit to the precision of any classical field measurement. Evaluating the mean and variance of the amplitude and phase quadratures we find

$$\langle \hat{X}_1 \rangle = \langle \hat{X}_2 \rangle = 0, \qquad \mathrm{Var}(\hat{X}_1) = \mathrm{Var}(\hat{X}_2) = 1. \tag{1.50}$$

This is a very important result as it identifies the standard quantum limit for field quadrature measurements, also known as the *the shot noise limit*. Also, the vanishing mean values show that the phase of the vacuum state – as well as any number state – is completely undefined.

Coherent states

Secondly, we consider the coherent states which are defined as the eigenstates of the annihilation operator

$$\hat{a}|\alpha\rangle = \alpha|\alpha\rangle, \qquad \langle\alpha|\hat{a}^\dagger = \alpha^*\langle\alpha|. \tag{1.51}$$

An interpretation of the generally complex eigenvalue $\alpha = |\alpha|e^{i\theta}$ is provided by evaluating the expectation value of the number operator

$$\langle\hat{n}\rangle = \langle\alpha|\hat{n}|\alpha\rangle = \langle\alpha|\hat{a}^\dagger\hat{a}|\alpha\rangle = \alpha^*\alpha = |\alpha|^2. \tag{1.52}$$

For a propagating field the power is proportional to the photon number flux, and by analogy with the classical case we can thus associate α with the field amplitude. For the photon number variance we find similarly

$$\mathrm{Var}(\hat{n}) = \langle\alpha|\hat{a}^\dagger\hat{a}\hat{a}^\dagger\hat{a} - \hat{a}^\dagger\hat{a}|\alpha\rangle = |\alpha|^2. \tag{1.53}$$

Expanded on the set of number states, the coherent states are given by

$$|\alpha\rangle = e^{-|\alpha|^2/2}\sum_{n=0}^{\infty}\frac{\alpha^n}{\sqrt{n!}}|n\rangle, \tag{1.54}$$

and calculating the photon number probability distribution we find, in accordance with (1.53) and (1.53), a Poissonian distribution

$$p(n) = |\langle n|\alpha\rangle|^2 = \frac{|\alpha|^{2n}}{n!}e^{-|\alpha|^2}. \tag{1.55}$$

The quadrature moments for coherent states are

$$\langle \hat{X}_1 \rangle = \alpha + \alpha^* = 2\,\mathrm{Re}(\alpha), \qquad \langle \hat{X}_2 \rangle = -i(\alpha - \alpha^*) = 2\,\mathrm{Im}(\alpha), \tag{1.56}$$

$$\mathrm{Var}(\hat{X}_1) = \mathrm{Var}(\hat{X}_2) = 1 \tag{1.57}$$

revealing that the coherent states are minimum uncertainty states with shot noise variance. Since the coherent states have well defined phase and amplitude for large photon numbers and yield an expectation value for the eletric field operator (1.26) equals the classical expression, they are by the correspondence principle, quantum analogues of the classical electric field emitted by a laser.

A coherent state is generated from the vacuum state by application of the displacement operator $|\alpha\rangle = \hat{D}(\alpha)|0\rangle$, defined as [47]

$$\hat{D}(\alpha) = e^{\alpha\hat{a}^\dagger - \alpha^*\hat{a}}, \tag{1.58}$$

with properties

$$\hat{D}^{-1}(\alpha) = \hat{D}(-\alpha), \qquad \hat{D}^\dagger(\alpha)\hat{a}\hat{D}(\alpha) = \hat{a} + \alpha. \tag{1.59}$$

Combining the results from Section 1.3.1 with the sideband representation (1.38) we see that the action of amplitude and phase modulation is exactly to perform displacement operations in phase space. We can therefore represent amplitude and phase modulation at frequency Ω by sideband displacement operators $\hat{D}^{AM}_{\omega_c\pm\Omega}(\xi\alpha/\sqrt{2})$ and $\hat{D}^{PM}_{\omega_c\pm\Omega}(i\xi\alpha/\sqrt{2})$, respectively.

Thermal states

A thermal state is characteristic of a harmonic oscillator in thermal equilibrium with a heat bath at temperature T. According to statistical mechanics such a state is described by the density operator

$$\hat{\rho}_{Th} = \frac{\exp(-\hat{H}/k_BT)}{\mathrm{Tr}[\exp(-\hat{H}/k_BT)]}, \tag{1.60}$$

where $\hat{H}$ is the single mode harmonic oscillator Hamiltonian, cf. (1.30), and k_B is the Boltzmann constant. In order to relate the thermal state to the occupancy of the harmonic oscillator, we can expand the density operator on the Fock states as:

$$\hat{\rho}_{Th} = \sum_{n'=0}^{\infty}\sum_{n=0}^{\infty} |n'\rangle\langle n'|\hat{\rho}_{Th}|n\rangle\langle n| \tag{1.61}$$

$$= \frac{1}{1+\langle n\rangle}\sum_{n=0}^{\infty}\left(\frac{\langle n\rangle}{1+\langle n\rangle}\right)^n |n\rangle\langle n| \tag{1.62}$$

The mean and variance of the excitation number can be found to be [44]:

$$\langle \hat{n}\rangle = \frac{1}{\exp(\hbar\omega/k_BT)-1}, \qquad \mathrm{Var}(\hat{n}) = \langle\hat{n}\rangle + \langle\hat{n}\rangle^2, \tag{1.63}$$

where ω is the harmonic oscillator frequency.

We will also be interested in knowing the thermal state first and second moments of the quadrature operators. Using the property of the density operator that mean values of system observables can be calculated as $\langle \hat{O} \rangle = \mathrm{Tr}(\hat{\rho}\hat{O})$, it is straightforward to show that the first and second moments of the quadratures for a thermal state are given by,

$$\langle \hat{X}_1 \rangle = \langle \hat{X}_2 \rangle = 0, \tag{1.64}$$

$$\mathrm{Var}(\hat{X}_1) = \mathrm{Var}(\hat{X}_2) = 1 + 2\langle \hat{n} \rangle. \tag{1.65}$$

Squeezed states

As dictated by Heisenberg's uncertainty relation, any optical quantum state must possess a certain amount of noise in the field quadratures. However, the uncertainty relation only bounds the product of the noises, leaving open the possibility of an asymmetric distribution among the two with the noise in one quadrature dropping below the shot noise level. In any case, the associated excess noise in the conjugate quadrature must always be such that the uncertainty relation remains fulfilled. Single-mode squeezed states are generated from the vacuum by the unitary *squeezing operator* [90, 116, 44]

$$\hat{S}(\zeta) = e^{\frac{1}{2}(\zeta^* \hat{a}^2 - \zeta \hat{a}^{\dagger 2})}, \tag{1.66}$$

where $\zeta = re^{i2\theta_s}$. The amplitude r is known as the squeezing parameter and θ_s is the squeezing phase. The appearance of squared field operators in the exponent indicates the nonlinearity of the process.

The action of the squeezing operator on the generalized quadrature operator (1.33) is given by

$$\hat{S}^\dagger(\zeta) \hat{X}_\theta \hat{S}(\zeta) = \hat{X}_\theta \cosh(r) - \hat{X}_{2\theta_s - \theta} \sinh(r), \tag{1.67}$$

and considering the particular phase angle $\theta' = \theta_s$ and $\theta_s + \pi/2$ for the conjugate quadrature we find,

$$\hat{S}^\dagger(\zeta) \hat{X}_{\theta_s} \hat{S}(\zeta) = \hat{X}_{\theta_s}(\cosh(r) - \sinh(r)) = \hat{X}_{\theta_s}\, e^{-r} \tag{1.68}$$

$$\hat{S}^\dagger(\zeta) \hat{X}_{\theta_s + \pi/2} \hat{S}(\zeta) = \hat{X}_{\theta_s + \pi/2}(\cosh(r) + \sinh(r)) = \hat{X}_{\theta_s + \pi/2}\, e^{r}. \tag{1.69}$$

Finally, taking the variances of the transformed quadratures we get,

$$\mathrm{Var}\left(\hat{S}^\dagger(\zeta) \hat{X}_{\theta_s} \hat{S}(\zeta)\right) = e^{-2r}\, \mathrm{Var}(\hat{X}_{\theta_s}), \tag{1.70}$$

$$\mathrm{Var}\left(\hat{S}^\dagger(\zeta) \hat{X}_{\theta_s + \pi/2} \hat{S}(\zeta)\right) = e^{2r}\, \mathrm{Var}(\hat{X}_{\theta_s + \pi/2}). \tag{1.71}$$

Thus, the action of the squeezing operator on the quadratures is to decrease the variance at the angle θ_s while increasing it for the conjugate angle $\theta_s + \pi/2$.

Bright squeezed states for which the field amplitude α is non-zero are generated by concatenating the squeezing operator with the previously defined displacement

operation, and a general bright squeezed state, alternatively squeezed coherent state, may be defined as,

$$|\alpha, \zeta\rangle = \hat{D}(\alpha)\hat{S}(\zeta)|0\rangle. \tag{1.72}$$

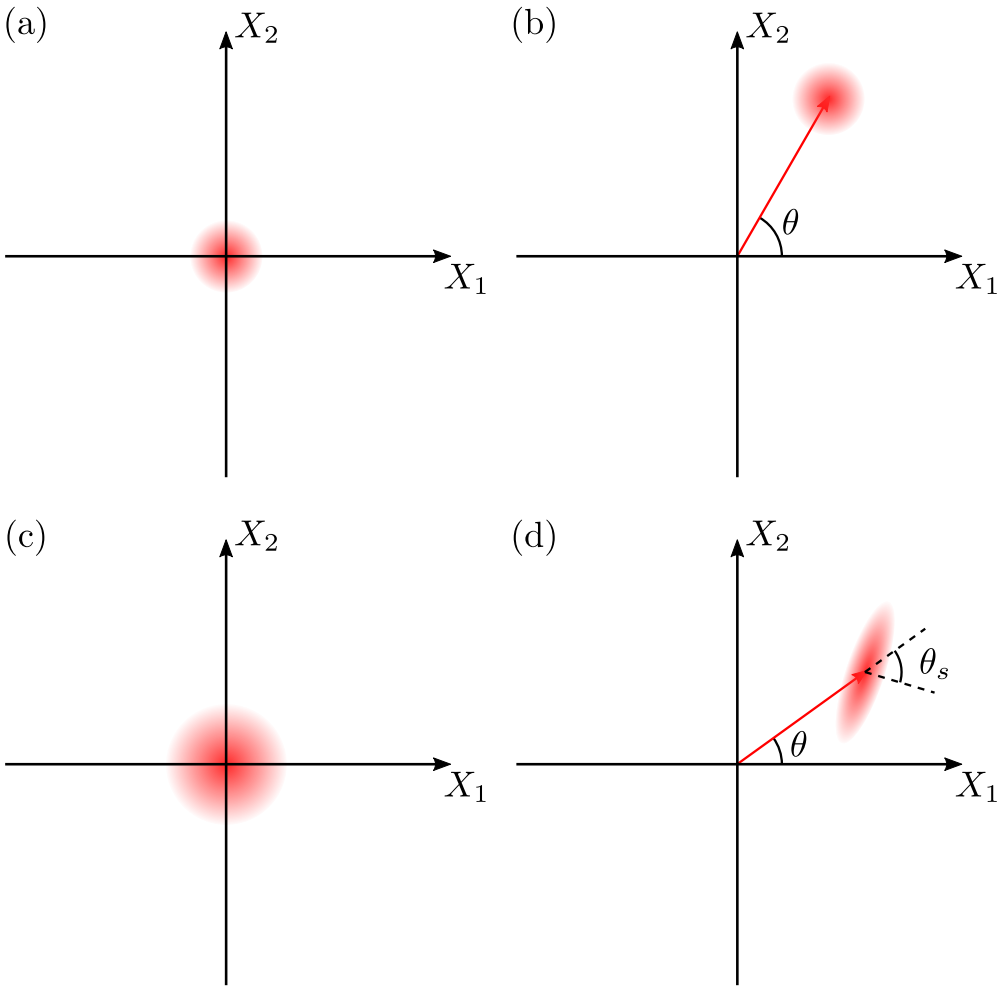

Figure 1.3: Phase space representation of basic quantum states. (a) vacuum state, (b) coherent state, (c) thermal state, and (d) bright squeezed state.

Experimental concepts 2

This chapter serves as an introduction to selected concepts and methods essential for the experiments presented in later parts of the thesis. Particular attention is devoted to the employed field detection schemes as they are techniques of paramount importance for interrogating optical quantum noise. It should be emphasized that the discussed concepts are common to the field of experimental quantum optics and does not represent novel developments particular to this work. The purpose of the chapter is thus solely to familiarize the reader with the framework of concepts in terms of which later discussions of experimental work will be phrased.

2.1 Interference and mode matching

The defining properties of a laser – a quasi-monochromatic spectrum and strong directionality – are consequences of a high degree of temporal and spatial coherence in the field. In an experimental configuration, the laser thus provides a global phase reference, provided that the characteristic length scale of the setup is smaller than the coherence length of the laser, $L_{coh} = c \cdot \tau_{coh} = c/\Delta\omega$, where c is the vacuum speed of light, τ_{coh} the coherence time, and $\Delta\omega$ the laser linewidth. For narrowband cw lasers the coherence length is on the order of kilometers.

As a consequence of the coherence, beams derived from the same laser can interfere. From an experimental point of view, this is an extremely important property as it allows for the implementation of a large number of manipulations and operations on the optical field. Furthermore, interference is crucial in providing the required phase reference for phase sensitive measurements of optical quantum states, as described in the following sections. Conditions for observing interference between two fields are that they have non-orthogonal polarizations and that they are *mode matched*, meaning that they occupy the same spatial mode. Any deviation from a perfect overlap will result in only partial interference and thereby loss.

Experimentally, it is important to quantify the efficiency of an interference process in order to account for the associated loss. Consider the interference of two classical modes α_1 and α_2 on a beamsplitter with intensity transmittivity T and spatial mode matching η. We can arbitrarily define the spatial mode of α_1 as the reference mode and expand the two interfering modes into a part residing in the reference mode

and a part orthogonal to the reference:

$$(\alpha_{1,ref}, \alpha_{1,orth}) = (\alpha_1, 0) \tag{2.1}$$
$$(\alpha_{2,ref}, \alpha_{2,orth}) = \left(\sqrt{\eta}\alpha_2, \sqrt{1-\eta}\alpha_2\right). \tag{2.2}$$

The resulting amplitude of any of the beamsplitter outputs is

$$(\alpha_{3,ref}, \alpha_{3,orth}) = \left(\sqrt{T}\alpha_1 + e^{i\theta}\sqrt{\eta(1-T)}\alpha_2, e^{i\theta}\sqrt{(1-\eta)(1-T)}\alpha_2\right), \tag{2.3}$$

where a relative phase between the interfering beams has been included. From this expression we can calculate the corresponding intensities residing in the reference and orthogonal mode, respectively.

$$I_{ref} = \alpha^*_{3,ref}\alpha_{3,ref} = TI_1 + \eta(1-T)I_2 + 2\sqrt{\eta T(1-T)}\sqrt{I_1 I_2}\cos\theta \tag{2.4}$$
$$I_{orth} = \alpha^*_{3,orth}\alpha_{3,orth} = (1-\eta)(1-T)I_2 \tag{2.5}$$

The total measured intensity is

$$I_{total} = I_{ref} + I_{orth} \tag{2.6}$$
$$= TI_1 + (1-T)I_2 + 2\sqrt{\eta T(1-T)}\sqrt{I_1 I_2}\cos\theta. \tag{2.7}$$

Assuming a balanced beamsplitter with $T = 1/2$ and equal beam intensities, the maximum and minimum output intensity is

$$I_{max} = I(1+\sqrt{\eta}) \tag{2.8}$$
$$I_{min} = I(1-\sqrt{\eta}), \tag{2.9}$$

from which we can construct the measurable interference fringe *visibility*

$$\mathcal{V} = \frac{I_{max} - I_{min}}{I_{max} + I_{min}} = \sqrt{\eta}. \tag{2.10}$$

2.2 Detection of light

Reliable and efficient detection of light is obviously of uttermost importance in any quantum optics experiment, since light is the carrier of information about the system being investigated, whether that be the light itself, an atomic ensemble, a solid state medium, or ... Depending on the nature of the light field and how information is encoded onto it, different detection strategies should be utilized to extract the information most efficiently. In continuous variable experiments we are generally concerned with the quantized electromagnetic *field*, meaning that broadband phase-sensitive detection is required; on the other hand photonics experiments are usually focused on the quantized electromagnetic *energy* requiring efficient detection of single photons and the photon statistics of the light field.

In this thesis work only the field properties of light have been investigated, but a range of different detection schemes has been utilized. In this section we review, from a theoretical point of view, the basics of the involved detection processes and their abilities in terms of detecting quantum properties of light. The actual implementation of the schemes will be discussed in later sections covering the corresponding experimental work. Common to all the schemes are that they are destructive in the sense that optical energy is absorbed and converted into an electrical signal proportional to the light intensity, and in all cases this photon-to-electron conversion is accomplished via the photo-electric effect in reverse-biased semiconductor PIN photodiodes. For such "square-law detectors" the generated photocurrent is proportional to the norm-square of the incident field strength or equivalently the optical power, $i(t) \propto |E(t)|^2 \propto P_{opt}$.

In performing field sensitive measurements, we will most often be interested in the spectral photocurrent revealing quantum properties of optical sidebands at frequencies $\pm\Omega$, relative to the optical carrier frequency ω. At optical wavelengths, say, $\lambda = 850\,\mathrm{nm}$, the corresponding carrier frequency is $\omega/2\pi = c/\lambda = 3.5 \cdot 10^{14}\,\mathrm{Hz}$, which is obvisouly not resolvable by any electronic detector. However, due to the square-law detection process, the bright carrier $Ee^{-i\omega t}$ will simultaneously beat with field sidebands $\delta E e^{-i(\omega\pm\Omega)t}$ on the photodiode and as a result the sideband component is down-mixed to an ac component of the photocurrent at rf frequency Ω. The measured ac component is due to the interference of the two sideband beat signals, while the dc signal is proportional to the carrier power. For this reason it is common – though maybe slightly confusing – to refer to the optical carrier as the dc component of the field and the sidebands as the ac components. In the case of a phase modulated beam, the sideband beat signals always interfere destructively in the amplitude quadrature (cf. Fig 1.2, the projections of the sideband phasors onto the carrier are always equal and opposite) meaning that no Ω-component is observed in the photocurrent. In order to observe a pure phase modulation, a phase sensitive measurement scheme, such as homodyne detection, is required. For an amplitude modulated beam, however, the modulation is directly observable. Monitoring the photocurrent spectrum, e. g. using an electronic spectrum analyzer (ESA), will thus yield direct information about the state of the optical sidebands.

2.2.1 Optical loss and quantum efficiency

In order for a photodetection process to provide a faithful measure of the input quantum state, all incoming photons must be detected and converted into photoelectrons. Many photon loss-channels are present in the process, such as reflection from diode cover, reflection from diode surface, over-filling of the active diode area, recombination of electron-hole pairs, intrinsic diode efficiency etc., all of which can in principle be shifted in front of the diode and modeled as a lumped beamsplitter loss. Classically, the loss can be represented as an amplification process with gain $\eta < 1$. But quantum mechanically we cannot simply say that the corresponding

input-output relation is given by $\hat{a}_{out} = \sqrt{\eta}\hat{a}_{in}$ since

$$[\hat{a}_{out}, \hat{a}_{out}^\dagger] = [\sqrt{\eta}\hat{a}_{in}, \sqrt{\eta}\hat{a}_{in}^\dagger] = \eta[\hat{a}_{in}, \hat{a}_{in}^\dagger] = \eta \neq 1, \tag{2.11}$$

meaning that the transformation is non-unitary. Salvation of the canonical commutation relation requires that we also account for the initial vacuum fluctuations in the loss mode $\hat{b}$, which is achieved by extending the above transformation to that of a beamsplitter with intensity transmittance η, such that

$$\hat{a}_{out} = \sqrt{\eta}\hat{a}_{in} + \sqrt{1-\eta}\hat{b}_{in}, \tag{2.12}$$

$$\hat{b}_{out} = \sqrt{\eta}\hat{b}_{in} - \sqrt{1-\eta}\hat{a}_{in}. \tag{2.13}$$

In this case $[\hat{a}_{out}, \hat{a}_{out}^\dagger] = \eta + (1-\eta) = 1$ and equivalently for $\hat{b}_{out}$. This is the standard beamsplitter model of loss in quantum optics which will also be employed in this thesis. For squeezed states the effect of loss is detrimental and from (2.12) it is clear why: the state is not only attenuated (first term), a portion of the vacuum field equal to the loss is additionally admixed (second term), meaning that any reduction of quantum noise in the input field will quickly be masked by vacuum fluctuations in the presence of loss. For an arbitrary quadrature of the input field the variance is modified by loss according to:

$$\mathrm{Var}(\hat{X}_\theta^{out}) = \eta \mathrm{Var}(\hat{X}_\theta^{in}) + (1-\eta). \tag{2.14}$$

Losses pertaining to the intrinsic efficiency of the photodiode are characterized by the quantum efficiency, quantifying the probability that a photon which is absorbed in the PIN depletion region also leads to a viable electron-hole pair. Commonly, the quantum efficiency of a diode is stated in terms of the *spectral responsivity* R_λ [A/W] which is the proportionality constant between the generated photocurrent and the absorbed optical power, $i = R_\lambda P_{opt}$. In order to evaluate the total detection efficiency, it more convenient to know the percentage quantum efficiency of a diode. A simple conversion relation is derived in the following.

The rate of photon absoptions is

$$n_{ph} = \frac{P_{opt}}{E} = \frac{P_{opt}\lambda}{hc}, \tag{2.15}$$

where E is the photon energy, and the corresponding rate of generated photoelectrons is

$$n_{el} = \frac{i}{q} = \frac{P_{opt}R_\lambda}{q}, \tag{2.16}$$

with q being the electron charge. Forming the ratio of the two quantities yields a relation between responsivity and quantum efficiency.

$$\eta_{QE} = \frac{n_{el}}{n_{ph}} = \frac{hc}{q\lambda}R_\lambda = 1236\,(\mathrm{nm}\cdot\mathrm{W})\mathrm{A}^{-1}\frac{R_\lambda}{\lambda}. \tag{2.17}$$

2.2.2 Direct detection

The most straightforward means of field detection is simply to focus the light onto a single photodiode, in which case the generated photocurrent is proportional to the number of photons in the field $i(t) \propto \hat{n}(t) = \hat{a}^\dagger(t)\hat{a}(t)$. For a coherent state input the linearized temporal and spectral photocurrents are,

$$i(t) = g_D(\alpha^* + \delta\hat{a}^\dagger)(\alpha + \delta\hat{a}) \approx g_D\left(|\alpha|^2 + \alpha\delta\hat{X}_1(t)\right) \tag{2.18}$$

$$i(\Omega) = g_D\left(|\alpha|^2\delta(\Omega) + \alpha\delta\hat{X}_1(\Omega)\right). \tag{2.19}$$

The proportionality constant g_D includes detection effciency and detector gain. The first spectral term is a dc component, proportional to the power in the optical carrier, while the second ac term provides a scaled measure of the field amplitude fluctuations at sideband frequencies.

2.2.3 Balanced homodyne detection

Completely characterizing the quantum fluctuation properties of an optical signal entails a complete shot noise normalized tomography of the sideband quadratures, which requires an optical phase reference. This is conveniently achieved by balanced homodyne detection in which a weak input signal field is mixed with a bright local oscillator (LO) on a balanced (50/50) beamsplitter. The two emerging output fields are directly detected by separate photodiodes and the final measurement output is given by the difference of the photocurrents.

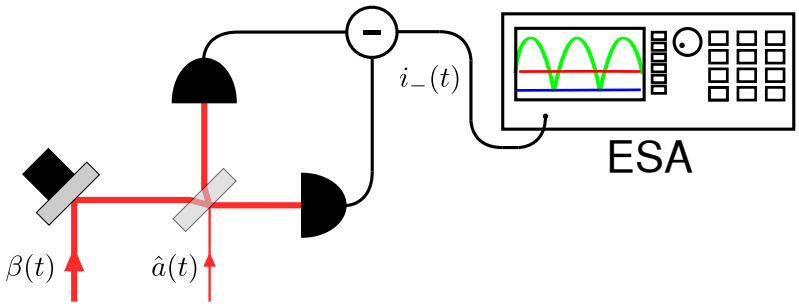

Figure 2.1: Schematic illustration of the experimental setup for homodyne detection.

Consider two optical beams interfering on a 50/50 beamsplitter, presented by field operators $\hat{a}(t) = \alpha(t) + \delta\hat{a}(t)$ and $\hat{b}(t) = (\beta(t) + \delta\hat{b}(t))e^{i\phi}$, respectively, with a relative phase ϕ. The resulting output fields will then be given by

$$\hat{d}_1(t) = \frac{1}{\sqrt{2}}\left((\alpha(t) + \delta\hat{a}(t)) - (\beta(t) + \delta\hat{b}(t))e^{i\phi}\right) \tag{2.20}$$

$$\hat{d}_2(t) = \frac{1}{\sqrt{2}}\left((\alpha(t) + \delta\hat{a}(t)) + (\beta(t) + \delta\hat{b}(t))e^{i\phi}\right) \tag{2.21}$$

Assuming that the gain of the two direct detection processes are identical, the corresponding linearized photocurrents are

$$\begin{aligned} i_1(t) &= g_D \hat{d}_1^\dagger(t)\hat{d}_1(t) \\ &\approx \frac{g_D}{2}\Big[\alpha(t)^2 + \beta(t)^2 - 2\alpha(t)\beta(t)\cos\phi \\ &\quad + \alpha(t)\Big(\delta\hat{X}_1^a(t) - \delta\hat{X}_{-\phi}^b(t)\Big) + \beta(t)\Big(\delta\hat{X}_1^b(t) - \delta\hat{X}_\phi^a(t)\Big)\Big] \end{aligned} \tag{2.22}$$

$$\begin{aligned} i_2(t) &= g_D \hat{d}_2^\dagger(t)\hat{d}_2(t) \\ &\approx \frac{g_D}{2}\Big[\alpha(t)^2 + \beta(t)^2 + 2\alpha(t)\beta(t)\cos\phi \\ &\quad + \alpha(t)\Big(\delta\hat{X}_1^a(t) + \delta\hat{X}_{-\phi}^b(t)\Big) + \beta(t)\Big(\delta\hat{X}_1^b(t) + \delta\hat{X}_\phi^a(t)\Big)\Big]. \end{aligned} \tag{2.23}$$

The differential photocurrent is then found to be

$$\begin{aligned} i_-(t) &= i_2(t) - i_1(t) \\ &\approx g_D\Big(2\alpha(t)\beta(t)\cos\phi + \alpha(t)\delta\hat{X}_{-\phi}^b(t) + \beta(t)\delta\hat{X}_\phi^a(t)\Big). \end{aligned} \tag{2.24}$$

Thus, in general the carrier amplitude of each beam probes the fluctuations of the other, though in orthogonal quadratures. To achieve a phase sensitive measurement of the signal quadrature noise alone we must require that one field – the local oscillator – is much brighter than the signal, $\beta \gg \alpha$, such that terms not containing β can be neglected. This is the usual *homodyne condition*. In this case the spectral variance of the differential signal is

$$\mathrm{Var}(i_-(\Omega)) \approx g_D^2\beta(t)^2\mathrm{Var}(\delta\hat{X}_\phi^a(\Omega)) \tag{2.25}$$

The prefactor can be easily measured by blocking the signal input. Doing so, the homodyne detector simply measures the variance of the vacuum field $\mathrm{Var}(\delta\hat{X}_{\mathrm{vac}}^a(\Omega)) = 1$, providing shot noise normalization for subsequent measurements of the signal field.

2.2.4 Self homodyne detection

Above, we discussed the case where the signal input to the homodyne detector is replaced by vacuum, but we only considered the differential photocurrent. Using (2.22) and (2.22) we can also form the linearized sum signal

$$i_+ = i_2(t) + i_1(t) \approx g_D(\beta(t)^2 + \beta(t)\delta\hat{X}_1^b), \tag{2.26}$$

with spectral variance

$$\mathrm{Var}(i_+(\Omega)) \approx g_D^2\beta(t)^2\mathrm{Var}(\delta\hat{X}_1^b). \tag{2.27}$$

This together with (2.25), for vacuum at the signal input, provides a shot noise calibrated measurement of the amplitude noise in the bright input mode, simply as the ratio of the sum and difference signal variances,

$$\frac{\mathrm{Var}(i_+(\Omega))}{\mathrm{Var}(i_-(\Omega))} = \frac{g_D^2\beta(t)^2\mathrm{Var}(\delta\hat{X}_1^b)}{g_D^2\beta(t)^2\mathrm{Var}(\delta\hat{X}_{\mathrm{vac}}^a(\Omega))} = \mathrm{Var}(\delta\hat{X}_1^b). \tag{2.28}$$

Self homodyning thus provides a convenient means for measuring the quantum noise properties of bright fields, in the sense that the field has a strong coherently excited carrier. Performing standard homodyne detection of such states can be technically challenging, since the detector must be able to withstand high optical powers without inflicting damage to the diodes or causing saturation in the circuit. In it's simplest form, as described above, the feasibility of the self homodyne scheme for squeezed light characterization is clearly limited by the fact that the local oscillator, provided by the carrier, is locked in-phase with the sidebands. This allows only for measurements of the amplitude quadrature. If, however, by some means, the relative phase between carrier and sidebands can be controlled, then the carrier can provide the necessary phase reference for projecting out any quadrature, enabling a full noise tomography of the sidebands. In the following we briefly mention two extended self homodyne schemes for which this can be achieved.

Cavity-assisted self homodyne detection

Introducing a cavity in the signal beam is one way of adding the dispersion required for self homodyne tomography, exploiting that the phase response of a cavity depends on frequency detuning with respect to the cavity resonance. Thus, by detuning the impinging signal field, an arbitrary relative phase between carrier and sidebands can be induced. In this way, complete conversion between amplitude and phase fluctuations can be achieved, as described in [130].

Displacement-assisted self homodyne detection

Alternatively, full state tomography is also achievable by interfering the signal beam with an auxiliary coherent beam $\beta e^{i\theta}$ prior to self homodyne detection. Since interference is conditioned on both spectral and spatial overlap of the partaking fields, the auxiliary will only interfere with the signal carrier at frequency ω while the sidebands are unaffected. Consequently, this entirely classical interference implements a displacement operation $\hat{D}(\beta e^{i\theta})_{\omega+\Omega}$ acting on the signal sidebands, and as the phase of the auxiliary is scanned the displaced state describes a circle in phase space. In this process, the absolute phase of the signal sidebands are unchanged while their relative phase with respect to the carrier *is* changing. Thus, self homodyne detection of the signal field will project out all fluctuation quadratures as the phase θ is scanned through.

Sampling of time-domain fluctuations via demodulation

One complication of the self homodyne scheme is that the signal quadrature variance is not easily measured by just recording the power spectrum of the photocurrent on a spectrum analyzer, as is the case for standard homodyne detection. The individual sum and difference current spectral variances are of course directly measurable, but recording them simultaneously and with the same overall detection gain, in order to faithfully derive the shot noise normalized variance in (2.28), is not straightforward. An alternative approach is to demodulate the individual ac photocurrents at a detection frequency $\Omega = \Omega'$, and sample the time-domain fluctuations of that particular spectral component, rather than measuring the total fluctuation power spectrum. Demodulation is achieved by mixing the photocurrent with an electrical local oscillator at frequency Ω' and low pass filtering the resulting signal, as illustrated in Fig. 2.2. In time-domain, the mixer output is given by multiplying the

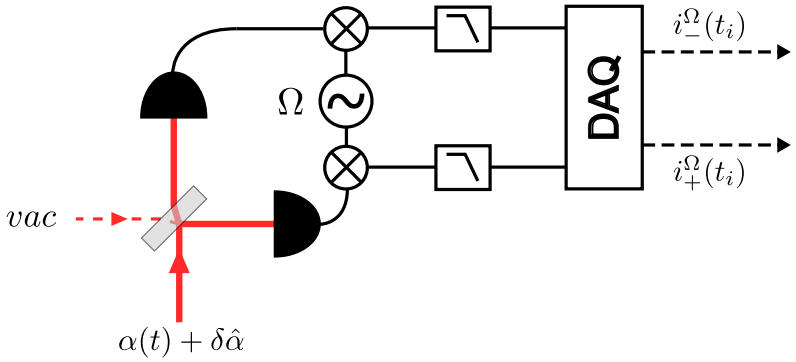

Figure 2.2: Schematic illustration of the experimental setup for self homodyne detection. Time-domain sampling of the individual photocurrents is achieved by down-mixing, low pass filtering, and subsequent recording using a digital data acquisition card (DAQ).

input signal with the local oscillator and the low pass filter is equivalent to temporal averaging over a time T inversely proportional to the filter bandwidth. For $T \to \infty$ the low pass filter transfer function approaches a δ-function and the demodulation output becomes a time-dependent dc-signal proportional to the fluctuating Fourier amplitude at frequency Ω of the photocurrent, denoted $i^{\Omega}(t)$. In reality, the demodulated signal will have a bandwidth determined by the bandwidth of the low pass filter. Sampling simultaneously the demodulated signals from both detectors, $i^{\Omega}_1(t)$ and $i^{\Omega}_2(t)$, provides full information about the statistical properties of the individual current fluctuations as well as for the sum and difference currents.

2.2.5 Heterodyne detection

As a final field detection scheme we discuss heterodyne detection. This scheme distinguishes itself from homodyne and selfhomodyne detection mainly by the fact

that it provides simultaneous measurements of two orthogonal quadratures of the signal field. The experimental implementation (Fig. 2.3) is very similar to that of homodyne detection but with the important distinctions that signal and local oscillator should be equally bright, $\alpha(t) = \beta(t)$, and that their relative phase must be stabilized to a value of $\phi = \pi/2$. As a result, the signal state is displaced by equal amounts along both amplitude and phase quadrature, and direct detection of the two beamsplitter outputs probes fluctuations of this displaced state along the orthogonal $\pm\pi/4$ quadratures. Unlike the case of homodyne detection, the contribution from the signal carrier probing vacuum fluctuations of the local oscillator cannot be neglected, since the fields are equally bright. And due to the indistinguishability of photons from the two fields and the absence of correlations in the vacuum fluctuations there are no means by which the two contributions can be separated, meaning that they will simply add up in quadrature in the final measurement outcome. Though not strictly necessary, it is convenient to consider again the sum

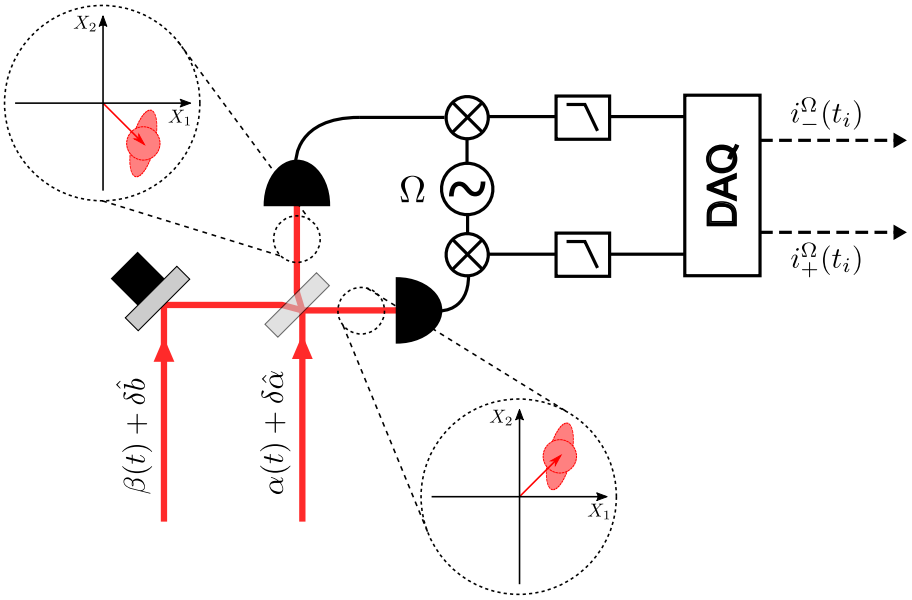

Figure 2.3: Schematic illustration of the experimental setup for heterodyne detection.

and difference of the detector photocurrents since that refers the measurement outcome back to the quadrature basis of the input signal, simplifying the expressions somewhat. From (2.22) and (2.23) we find the spectral variances of the linearized sum and difference photocurrents to be

$$\mathrm{Var}(i_+(\Omega)) \approx g_D^2 \beta(t)^2 \Big(\mathrm{Var}(\delta\hat{X}_1^a(\Omega)) + 1\Big), \tag{2.29}$$

$$\mathrm{Var}(i_-(\Omega)) \approx g_D^2 \beta(t)^2 \Big(\mathrm{Var}(\delta\hat{X}_2^a(\Omega)) + 1\Big), \tag{2.30}$$

where we have assumed a coherent state for the local oscillator. Indeed the heterodyne detection provides simultaneous knowledge about orthogonal quadratures of

the state, but as expected at the expense of an additional shot noise penalty – an inevitable price ensuring that the simultaneous measurement of conjugate variables is in accordance with Heisenberg's uncertainty relation.

Simply measuring the above spectral variances is, however, not enough to obtain full tomographic knowledge about the signal state, since we are only projecting the noise onto one particular set of orthogonal quadratures, neglecting any potential correlations between them. Measuring a squeezed state would thus only give a rightful characterization in the specific cases of amplitude or phase squeezing. In the other extreme, a state squeezed along the $(\hat{X}_1 \pm \hat{X}_2)/\sqrt{2}$ quadrature would only reveal excess noise in both measured quadratures.

The situation is quite different if instead the temporal fluctuations of the photocurrents are sampled and the sums and differences are formed subsequently, as discussed in the previous section. Then the total data set $\{(i_+^\Omega(t_i), i_-^\Omega(t_i))\}$, where

$$i_+^\Omega(t_i) = g_D\beta(t_i)\Big(\delta X_1^a(\Omega) + \delta X_1^b(\Omega)\Big), \tag{2.31}$$

$$i_-^\Omega(t_i) = g_D\beta(t_i)\Big(\delta X_2^a(\Omega) - \delta X_2^b(\Omega)\Big), \tag{2.32}$$

represents the outcomes of an ensemble of independent simultaneous projections of the signal state fluctuations onto quadratures $\hat{X}_1$ and $\hat{X}_2$, each sampled at time t_i. The temporal data gives us not only knowledge about the variances of the sum and difference photocurrents but also their correlations. This is all contained in the covariance matrix, which in shot noise normalized form, is given by

$$\begin{aligned}\boldsymbol{\gamma}(i_+^\Omega, i_-^\Omega) &= \frac{1}{2g_D^2\beta^2}\begin{pmatrix} \mathrm{Var}(i_+^\Omega) & \mathrm{Cov}(i_+^\Omega, i_-^\Omega) \\ \mathrm{Cov}(i_-^\Omega, i_+^\Omega) & \mathrm{Var}(i_-^\Omega)\end{pmatrix} \\ &= \frac{1}{2}\begin{pmatrix} 1+\mathrm{Var}(\delta X_1^a) & \mathrm{Cov}(\delta X_1^a, \delta X_2^a) \\ \mathrm{Cov}(\delta X_2^a, \delta X_1^a) & 1+\mathrm{Var}(\delta X_2^a)\end{pmatrix}_\Omega .\end{aligned} \tag{2.33}$$

Since the covariance matrix is normal per construction ($\boldsymbol{\gamma} = \boldsymbol{\gamma}^{\mathbf{T}}$), it is diagonalizable by an orthogonal matrix $\mathbf{A}$ such that $\mathbf{A}^{-1}\boldsymbol{\gamma}\mathbf{A} = \mathrm{diag}(\mathrm{Var}(\hat{X}_1^P), \mathrm{Var}(\hat{X}_2^P))$, where the eigenvalues represent the principal variances of the state. Coming back to the issue of measuring squeezing in an arbitrary quadrature, mentioned in the previous paragraph, we see that time-domain heterodyne detection conveniently solves the problem. If a state squeezed in the $\hat{X}_\theta$ quadrature is measured in $(\hat{X}_1, \hat{X}_2)$-basis, we can always find a diagonalizing rotation matrix $\mathbf{R}(\theta)$ that recovers the squeezed and anti-squeezed quadrature variances, $\mathbf{R}(\theta)^{-1}\boldsymbol{\gamma}\mathbf{R}(\theta) = \mathrm{diag}(\mathrm{Var}(\delta\hat{X}_\theta), \mathrm{Var}(\delta\hat{X}_{\theta+\pi/2}))$.

In the context of squeezed state characterization, it is important to note that the heterodyne scheme imposes an upper limit to the *measurable* degree of squeezing. Assuming a pure squeezed state with principal quadrature variances $e^{\pm 2r}$ we see that the corresponding measured variances, given by the diagonal elements of the covariance matrix, are $(1 + e^{\pm 2r})/2$. In the limit of infinite squeezing strength we find

$$\lim_{r\to\infty}\frac{1}{2}(1+e^{\pm 2r}) = \begin{cases} +\infty \\ \frac{1}{2}\end{cases}, \tag{2.34}$$

meaning that we can never hope to observe more than 3 dB of squeezing. Forming the quadrature variance product we see that

$$\mathrm{Var}(\delta\hat{X}_\theta)\mathrm{Var}(\delta\hat{X}_{\theta+\pi/2}) = \frac{1}{4}(1+e^{-2r})(1+e^{2r}) = \frac{1}{2}(1+\cosh(2r)) \geq 1, \qquad (2.35)$$

signifying that the additional shot noise unit introduced to each quadrature measurement indeed ensures that Heisenberg's uncertainty relation is fulfilled.

Finally, it is of practical importance to note that the difference of the dc photocurrents, cf. (2.24), is given by

$$i_-^{dc} = 2g_D\alpha(t)\beta(t)\cos\phi. \qquad (2.36)$$

This signal has zero-crossings at phase values $\phi = m\cdot\pi/2$, providing a convenient error signal for stabilizing the relative phase between signal carrier and local oscillator to the required value $\phi = \pi/2$.

Part II

Quantum sensing with cavity optomechanics

Introduction 3

Quantum mechanics is considered a generally valid theory in the sense that it is applicable to physical systems pertaining to the microscopic subatomic universe as well as macroscopic phenomena well-described by classical Newtonian physics. However, from a practical point of view, it is certainly not feasible to describe classical dynamics, say, the collision of billiard balls, using quantum mechanics – and it would be a blatant example of *shooting sparrows with cannons*. But fundamentally it is possible, and consistency of the classical and quantum predictions is enforced by the heuristic *correspondence principle* of Niels Bohr:

> "The aim of regarding the quantum theory as a rational generalization of the classical theories led to the formulation of the so-called correspondence principle." [18]

> "[...] which originated in the search for the closest possible connection between the statistical account of atomic processes and the consequences to be expected from classical theory, which should be valid in the limit where the actions involved in all stages of the analysis of the phenomena are large compared with the universal quantum." [19]

It dictates that the quantum mechanical description should converge to that of classical physics in the limit of large quantum numbers, thus acting as a boundary condition on quantum mechanics towards the classical regime. The transition between the quantum and classical regimes, commonly termed *the quantum-classical boundary*, is a bit of a grey-zone about which very little knowledge exist. And as such it is an area of immense fundamental interest. Since the advent of quantum mechanics, the quantum-classical transition has been a heavily debated topic, and it is at the heart of the so-called *measurement problem*. Numerous proposals exist for the mechanism by which a system transits from one regime to the other, but the number of appropriate systems admitting experimental scrutiny are sparse.

Quantum behaviour of a macroscopic system was observed as early as in 1937, when P. Kapitza [68] discovered the superfluidity of liquid helium, simultaneously with J. F. Allen and A. D. Misener [1]. The related Bose-Einstein condensation phenomenon was only demonstrated much later in 1995 with the first condensates in dilute atomic gases of rubidium[2] and sodium [34]. Also, distinct quantum effects such as matterwave interference and decoherence have been observed for

macroscopic buckyball molecules [24, 50] and macrocyclic compounds [66]. Other prominent demonstrations of macroscopic quantum systems are entanglement of Josephson-junction qubits [16] and atomic ensembles [67].

Within the last decades a class of conceptually much simpler macroscopic systems, collectively known as *micromechanical resonators*, have attracted much attention as potential candidates for displaying quantum behaviour and serving as testbed-systems for probing the quantum-classical transition[13, 45, 95]. Such systems are particularly compelling since they are bulk and truly classical objects that can be fabricated with tailored properties within the existing and mature nanofabrication platform. And they are just about the simplest possible systems one can hope to show quantum behaviour – mechanical harmonic oscillators! The diversity of demonstrated micromechanical resonators is by now vast, with some of the most investigated systems being microwave nanomechanical cavities [125, 126], cantilevers [73], beam oscillators [49, 124], membranes [129, 12], microtoroids [7, 60, 3], photonic crystals [108, 107], and optically levitated microparticles [70].

In probing mechanical displacements optically, the attainable sensitivity is fundamentally limited by noise contributions from two sources [28]: *imprecision noise* in the form of photon shot noise and *quantum back-action noise* due to a stochastic radiation pressure force imparted on the mechanical oscillator by vacuum fluctuations. The optimal sensitivity is given by the so-called Standard Quantum Limit (SQL), in which case the two above contributions are exactly equal. Hitherto, optomechanical experiments have exclusively been carried out using classical coherent probe light for which the imprecision noise contribution scales $\propto 1/N$, with N being the deployed number of photons. This suggests that an arbitrarily high sensitivity can be achieved simply by increasing the optical probe power. However, the quantum back-action noise scales as $\propto N$, and as N is increased this contribution will eventually dominate the imprecision noise, attaining the limiting SQL sensitivity at the particular turning point probe power P_{SQL}. Reaching the SQL for mechanical displacement sensing has been a long standing goal that still remains unachieved. Imprecision noise surpassing that at the SQL has however been demonstrated [125, 4, 5], but so far only at power levels well above that corresponding to the SQL. The ability to access this regime experimentally has also enabled observation of the quantum back-action noise [93, 100] that enforces the SQL and which is a direct consequence of Heisenberg's uncertain principle.

The potentials of cavity optomechanical systems [71] as probes for foundational quantum physics are intriguing and fascinating, and a path we might consider in the future. However, in the work covered in this part of the thesis the approach has been somewhat different. Rather than actually striving to reveal quantum properties of a mechanical oscillator, our focus has been on facilitating such observations through quantum-enhanced probing strategies. It has been long known that squeezed states enable operation of interferometers below the shot noise limit [27] and thereby quantum-enhanced interferometric displacement sensing, as first demonstrated by Xiao et al. [134] and more recently also applied in the context of Sagnac interferometers [39] and gravitational wave detection [127, 128]. However, this technique has

not before been applied in the context of micromechanical resonator displacement sensing. The primary objective of this project has thus been to interface such a microstructured oscillator with squeezed light at room temperature and demonstrate a quantum-enhanced transduction of the classical thermally induced resonator motion, thereby marrying the fields of cavity optomechanics and quantum sensing. It is important to stress that a quantum enhanced transduction sensitivity in itself by no means is equivalent to surpassing, or even approaching, the SQL for displacement sensitivity. But it is one potential way of achieving the required measurement imprecision noise that has not been explored previously.

The work presented in this part constitutes the first endeavours of our group into the field of optomechanics, and was carried out in collaboration with the group of Warwick Bowen at University of Queensland, in particular Glen I. Harris, who visited DTU for about 3 months in late 2011 and brought with him the microtoroidal resonators and tapered optical fibres that were used in the experiments. The optomechanical setup was constructed entirely during the time frame of the project, while the employed squeezed light source was already constructed in the lab some years back. Here the squeezed light source will simply be considered as an available resource and a detailed account for its construction and performance will not be provided. For further details, we refer the reader to the PhD thesis of Jiri Janousek [65].

Cavity optomechanics 4

In this chapter we introduce the generic cavity optomechanical system and associated interaction Hamiltonian describing the coupling of optical and mechanical degrees of freedom. We will then set up a detailed quantum mechanical model for the system dynamics describing the transduction of mechanical vibrations onto the light field, taking inspiration from the linear amplifier model presented by Botter et al. [21]. Furthermore, we discuss a phase space representation of the optomechanical transduction process providing a bridge to the standard quantum optical formalism.

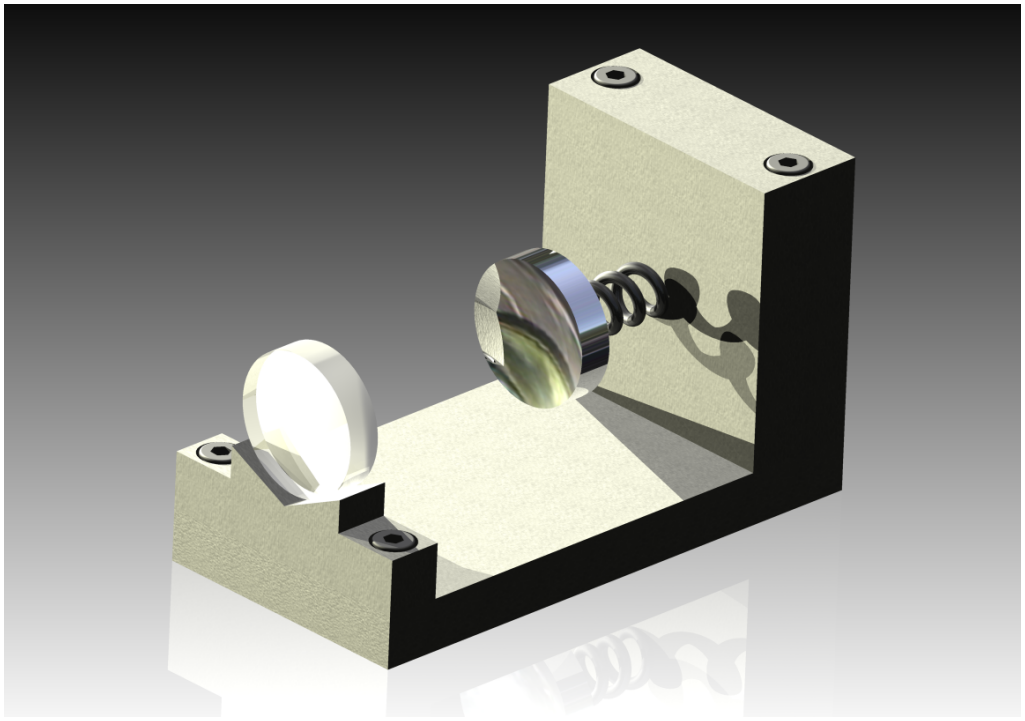

Figure 4.1: Artistic illustration of a generic cavity optomechanical system, comprised of a semi-transparent coupling mirror and a vibrating end mirror.

4.1 Generic system and interaction Hamiltonian

The generic cavity optomechanical system consists of an optical Fabry-Perot cavity with a fixed coupling mirror and a perfectly reflecting end mirror that is free to oscillate along the cavity axies, as simplistically illustrated in Fig. 4.1. A driving laser field is injected into the cavity through the coupling mirror, and the momentum imparted upon reflection exerts a radiation pressure force on the movable mirror, thereby driving its motion. At the same time, the mechanical motion acts back on the light through the oscillating boundary condition which results in a time-varying cavity resonance condition. In the simplest case, the light-mechanics interaction is given by the mutual coupling of single mode optical and mechanical harmonic oscillators. The interaction strength depends on the optical power, proportional to the intra-cavity photon number, and the displacement of the mechanical oscillator from its unperturbed position.

In order to quantify the interaction we investigate the dependence of the optical resonance on a mechanical displacement x. The optical resonance condition is $N \cdot \lambda_N = nL, N \in \mathbb{N}$, where L is the round trip length and n the refractive index in which the cavity mode propagates. The corresponding resonance frequencies are

$$\omega_N = 2\pi \frac{c}{n\lambda_N} = N \cdot 2\pi \frac{c}{nL}. \tag{4.1}$$

A mechanical displacement of the cavity end mirror by an amount x, such that $L \to L + x$, results in a position dependent perturbed resonance frequency

$$\omega_N(x) = N \cdot 2\pi \frac{c}{n(L+x)} = N \cdot 2\pi \frac{c}{nL} \frac{L}{L+x} \simeq \omega_N \left(1 - \frac{x}{L}\right), \tag{4.2}$$

for $x \ll L$. Thus, to first order in the mechanical displacement we have for any optical resonance that

$$\omega(x) = \omega_0 + gx, \tag{4.3}$$

where ω_0 is the unperturbed resonance and $g = -\omega_0/L$ is the optomechanical coupling constant.

We now quantize the optical intracavity field and mechanical harmonic oscillator in terms of annihilation and creation operators $\hat{a}$, $\hat{a}^\dagger$ and $\hat{b}$, $\hat{b}^\dagger$, respectively, each satisfying canonical commutation relations

$$[\hat{a}, \hat{a}^\dagger] = 1, \qquad [\hat{b}, \hat{b}^\dagger] = 1. \tag{4.4}$$

Using the above simple arguments we can express the standard optomechanical Hamiltonian governing the dynamics of the system as

$$\hat{H} = \hbar\omega_0 \hat{a}^\dagger \hat{a} + \hbar\omega_m \hat{b}^\dagger \hat{b} + \hbar g_0 \left(\hat{b} + \hat{b}^\dagger\right) \hat{a}^\dagger \hat{a}, \tag{4.5}$$

where ω_0 and ω_m are the respective optical and mechanical resonance frequencies. The first and third terms result from inserting (4.3) into the usual free cavity field

Hamiltonian and the second term describes the free evolution of the mechanical oscillator. The important third term accounts for the optomechanical interaction, coupling the mechanical oscillator position $\hat{x} = x_{zpf}(\hat{b}+\hat{b}^\dagger)$ to the intracavity photon number $\hat{a}^\dagger\hat{a}$. The interaction strength is characterized by *vacuum optomechanical coupling rate* $g_0 = x_{zpf}\omega_0/L$. The pre-factor $x_{zpf} = \sqrt{\hbar/2M\omega_m}$ is the amplitude of the mechanical zero-point fluctuations, with M the effective mass of the mechanical oscillator.

4.2 Phase space visualization

In the limit of a highly excited mechanical oscillator, e.g. for the system being in thermal equilibrium with a heat bath at room temperature, the mechanical displacement can be considered as a classical harmonic oscillation $x(t) = \delta x \sin(\omega_m t)$ with the particular mode frequency ω_m and an amplitude δx. Correspondingly, the optical resonance frequency will vary in time as $\omega(t) = \omega_0 + g_0\delta x \sin(\omega_m t)$, resulting in a frequency modulated intracavity field,

$$\begin{aligned}
\alpha(t) &= \alpha_0 e^{-i\int_0^t \omega(\tau)d\tau} && (4.6)\\
&= \alpha_0 e^{-i\omega_0 t} e^{-ig_0\delta x\int_0^t \sin(\omega_m\tau)d\tau} && (4.7)\\
&= \alpha_0 e^{-i\omega_0 t} e^{-i\beta(1-\cos(\omega_m t))} && (4.8)\\
&\approx \alpha_0 e^{-i\beta}\left(e^{-i\omega_0 t} + i\frac{\beta}{2}e^{-i(\omega_0-\omega_m)t} + i\frac{\beta}{2}e^{-i(\omega_0+\omega_m)t}\right). && (4.9)
\end{aligned}$$

Here we have assumed the modulation index $\beta = g_0\delta x/\omega_m$ to be small. Thus for a resonant coherent drive field the optomechanical interaction is a mere phase modulation of the carrier, and as a result photons from the carrier are scattered into symmetrically spaced Stokes and anti-Stokes sidebands at frequencies $\pm\omega_m$ relative to the carrier frequency. In the frequency resolved phase space picture (Fig. 4.2) we can thus think of the optomechanical interaction as the simultaneous action of displacement operations $\hat{D}_{\omega_c\pm\omega_m}[i\beta\alpha/\sqrt{2}]$ creating weak coherent states at the sidebands with an amplitude proportional to the mechanical displacement δx. In this way information about the frequency and amplitude of the mechanical resonator is transduced onto the optical field which can subsequently be read out by homodyne detection of the phase quadrature.

4.3 Quantum dynamics

Having introduced the general optomechanical system and provided a classical understanding of the interaction, we now turn to a detailed modeling of the quantum mechanical dynamics governed by the optomechanical interaction Hamiltonian (4.5). We will do so, using the quantum Langevin equation formalism.

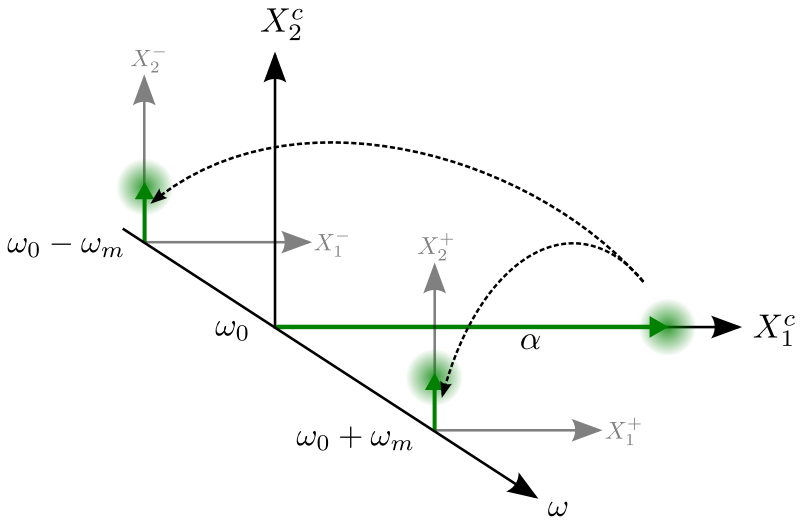

Figure 4.2: Phase space representation of optomechanical transduction. Through the optomechanically mediated phase modulation, photons are scattered from the probe carrier into weak sideband coherent states carrying information about the mechanical oscillation frequency and amplitude. The generated sideband states are associated with vacuum fluctuations which ultimately limit the measurement sensitivity.

4.3.1 Quantum Langevin equations of motion

We represent the coupling efficiency of the cavity input mirror and intracavity loss by amplitude coupling rates κ_c and κ_0, respectively, resulting in a total cavity decay rate (HWHM) of $\kappa = \kappa_c + \kappa_0$. The admixed vacuum mode associated with loss is represented by an annihilation operator $\hat{c}$. Similarly, the mechanical system is characterized by a linear momentum damping rate γ_m and a Langevin noise operator $\hat{\xi}_{th}$ representing the stochastic momentum kicks that drive the mechanical motion due to coupling with the thermal environment. Driven by an input field $\hat{a}_{in}e^{-i\omega_d t}$ the intracavity field and mechanical mode dynamics is described by the quantum Langevin equations of motion

$$\frac{d\hat{a}}{dt} = -\frac{i}{\hbar}\left[\hat{a}, \hat{H}\right] - \kappa\hat{a} + \sqrt{2\kappa_c}\hat{a}_{in}e^{-i\omega_d t} + \sqrt{2\kappa_0}\hat{c}, \tag{4.10}$$

$$\frac{d\hat{b}}{dt} = -\frac{i}{\hbar}\left[\hat{b}, \hat{H}\right] - \gamma_m\hat{b} + \sqrt{2\gamma_m}\hat{\xi}_{th}, \tag{4.11}$$

and a corresponding set for the conjugate operators. For the sake of notational clarity, we have omitted the explicit time dependence of operators, as will also be the case in the remainder of this section. It is convenient to transform the intracavity field into a frame rotating at the driving laser frequency ω_d. Using the results of Appendix A this is achieved by making the substitution $\hat{a} \rightarrow e^{-i\omega_d t}\hat{a}$. After expanding the commutators using (4.5) we get the following rotating frame

equations of motion

$$\frac{d\hat{a}}{dt} = -(\kappa - i\Delta)\hat{a} - ig_0\left(\hat{b} + \hat{b}^\dagger\right)\hat{a} + \sqrt{2\kappa_c}\hat{a}_{in} + \sqrt{2\kappa_0}\hat{c}, \tag{4.12}$$

$$\frac{d\hat{b}}{dt} = -i\omega_m\hat{b} - ig_0\hat{a}^\dagger\hat{a} - \gamma_m\hat{b} + \sqrt{2\gamma_m}\hat{\xi}_{th}, \tag{4.13}$$

where we have introduced the drive field detuning $\Delta = \omega_d - \omega_0$. The boundary conditon for the cavity field is given by the input-output relation

$$\hat{a}_{out} = \hat{a}_{in} - \sqrt{2\kappa_c}\hat{a}, \tag{4.14}$$

which will be used to project the intracavity field onto the measurable output field. From (4.12) and (4.14) we can derive an equation for the mean value of the cavity mode $\alpha = \langle\hat{a}\rangle$, and in steady state, $d\alpha/dt = 0$, the relation between the intracavity and driving field is found to be

$$\alpha = \frac{\sqrt{2\kappa_c}}{\kappa - i\Delta}\alpha_{in}. \tag{4.15}$$

An important parameter characterizing the optical response of the system is the coupling coefficient $\eta_c = \kappa_c/\kappa$, describing the balance between the rate at which photons are coupled into the cavity and the total rate at which they are lost. The coupling coefficient is obviously bounded by $0 \leq \eta_c \leq 1$, and it characterizes the coupling regime in which the cavity is operated: If the input and loss rates are exactly balanced, $\kappa_c = \kappa$ then $\eta_c = 1/2$ and the cavity is said to be *critically coupled*. In case of a net photon loss ($\eta_c < 1/2$) or gain ($\eta_c > 1/2$) the cavity is *under-coupled* and *over-coupled*, respectively.

4.3.2 Linearized dynamics

Since we are interested only in the optical and mechanical fluctuations, we will linearize the equations of motion about the mean amplitude as outlined in Section 1.4.2. Substituting $\hat{a} = \alpha + \delta\hat{a}$, and similarly for all operators, into (4.12-4.13) and retaining only terms of first order in the fluctuations we find the following set of linearized equations of motion for the fluctuations:

$$\frac{d}{dt}\delta\hat{a} = -(\kappa - i\Delta)\delta\hat{a} - ig_0\alpha(\delta\hat{b} + \delta\hat{b}^\dagger) + \sqrt{2\kappa_c}\delta\hat{a}_{in} + \sqrt{2\kappa_0}\delta\hat{c}, \tag{4.16}$$

$$\frac{d}{dt}\delta\hat{b} = -i\omega_m\delta\hat{b} - ig_0\alpha(\delta\hat{a} + \delta\hat{a}^\dagger) - \gamma_m\delta\hat{b} + \sqrt{2\gamma_m}\delta\hat{\xi}_{th}. \tag{4.17}$$

By taking the sum and differences of (4.16) and (4.17) and their conjugates, we can construct a new set of equations of motion for the optical and mechanical

fluctuation quadratures, cf. definitions in Section 1.4.1:

$$\frac{d}{dt}\delta\hat{X}_1^a = -\kappa\delta\hat{X}_1^a - \Delta\delta\hat{X}_2^a + \sqrt{2\kappa_c}\delta\hat{X}_1^{a,in} + \sqrt{2\kappa_0}\delta\hat{X}_1^c, \tag{4.18}$$

$$\frac{d}{dt}\delta\hat{X}_2^a = -\kappa\delta\hat{X}_2^a + \Delta\delta\hat{X}_1^a - 2g_0\alpha\delta\hat{X}_1^b + \sqrt{2\kappa_c}\delta\hat{X}_2^{a,in} + \sqrt{2\kappa_0}\delta\hat{X}_2^c, \tag{4.19}$$

$$\frac{d}{dt}\delta\hat{X}_1^b = \omega_m\delta\hat{X}_2^b - \gamma_m\delta\hat{X}_1^b + \sqrt{2\gamma_m}\delta\hat{X}_1^\xi, \tag{4.20}$$

$$\frac{d}{dt}\delta\hat{X}_2^b = -\omega_m\delta\hat{X}_1^b - 2g_0\alpha\delta\hat{X}_1^a - \gamma_m\delta\hat{X}_2^b + \sqrt{2\gamma_m}\delta\hat{X}_2^\xi. \tag{4.21}$$

Here $(\delta\hat{X}_1^a, \delta\hat{X}_2^a)$ are the intracavity field fluctuation quadratures, $(\delta\hat{X}_1^{a,in}, \delta\hat{X}_2^{a,in})$ the driving field fluctuations, $(\delta\hat{X}_1^c, \delta\hat{X}_2^c)$ the admixed vacuum fluctuations, $(\delta\hat{X}_1^b, \delta\hat{X}_2^b)$ the mechanical fluctuations, and $(\delta\hat{X}_1^\xi, \delta\hat{X}_2^\xi)$ the thermal fluctuations driving the mechanics.

The above differential equation system for the fluctuation quadratures can be reformulated as a single matrix equation

$$\frac{d\boldsymbol{\delta q}}{dt} = \mathbf{M}.\boldsymbol{\delta q} + \sqrt{2\kappa_c}\boldsymbol{\delta q}_{a,in} + \sqrt{2\kappa_0}\boldsymbol{\delta q}_{c,in} + \sqrt{2\gamma_m}\boldsymbol{\delta q}_{b,in}, \tag{4.22}$$

where we have introduced the vectors $\boldsymbol{\delta q} = (\delta\hat{X}_1^a, \delta\hat{X}_2^a, \delta\hat{X}_1^b, \delta\hat{X}_2^b)^T$, $\boldsymbol{\delta q}_{a,in} = (\delta\hat{X}_1^{a,in}, \delta\hat{X}_2^{a,in}, 0, 0)^T$, $\boldsymbol{\delta q}_{c,in} = (\delta\hat{X}_1^c, \delta\hat{X}_2^c, 0, 0)^T$, and $\boldsymbol{\delta q}_{b,in} = (0, 0, \delta\hat{X}_1^\xi, \delta\hat{X}_2^\xi)^T$. The system matrix has the block form

$$\mathbf{M} = \begin{pmatrix} \mathbf{M}_a & \mathbf{T} \\ \mathbf{T} & \mathbf{M}_b \end{pmatrix} = \left(\begin{array}{cc|cc} -\kappa & -\Delta & 0 & 0 \\ \Delta & -\kappa & -2g_0\alpha & 0 \\ \hline 0 & 0 & -\gamma_m & \omega_m \\ -2g_0\alpha & 0 & -\omega_m & -\gamma_m \end{array}\right), \tag{4.23}$$

where submatrices $\mathbf{M}_a$ and $\mathbf{M}_b$ account for the individual evolution of the optical and mechanical systems while the interaction is covered by the transduction matrix $\mathbf{T}$.

4.3.3 Frequency-domain solution

In order to solve the equation system (4.22) we move into frequency space, using the Fourier transform relations

$$\hat{a}(\Omega) = \frac{1}{\sqrt{2\pi}}\int dt\, e^{i\Omega t}\hat{a}(t) \quad \leftrightarrows \quad \hat{a}(t) = \frac{1}{\sqrt{2\pi}}\int d\Omega\, e^{-i\Omega t}\hat{a}(\Omega), \tag{4.24}$$

and the equation system now takes the form

$$\mathbf{M}_\Omega.\boldsymbol{\delta q}(\Omega) = \sqrt{2\kappa_c}\boldsymbol{\delta q}_{a,in}(\Omega) + \sqrt{2\kappa_0}\boldsymbol{\delta q}_{c,in}(\Omega) + \sqrt{2\gamma_m}\boldsymbol{\delta q}_{b,in}(\Omega). \tag{4.25}$$

The frequency space system matrix is

$$\mathbf{M}_\Omega = \begin{pmatrix} \mathbf{M}_{\Omega,a} & -\mathbf{T} \\ -\mathbf{T} & \mathbf{M}_{\Omega,b} \end{pmatrix} = \left(\begin{array}{cc|cc} \kappa - i\Omega & \Delta & 0 & 0 \\ -\Delta & \kappa - i\Omega & 2g_0\alpha & 0 \\ \hline 0 & 0 & \gamma_m - i\Omega & -\omega_m \\ 2g_0\alpha & 0 & \omega_m & \gamma_m - i\Omega \end{array}\right). \tag{4.26}$$

We are interested in deriving an expression for the optical output quadratures as function of the various fluctuation inputs to the system. To this end it is convenient to split (4.25) into separate 2-dimensional systems for the optical (o) and mechanical (m) quadratures

$$\boldsymbol{\delta q}^o(\Omega) = \mathbf{M}_{\Omega,a}^{-1}\left(\mathbf{T}.\boldsymbol{\delta q}^m(\Omega) + \sqrt{2\kappa_c}\boldsymbol{\delta q}^o_{a,in}(\Omega) + \sqrt{2\kappa_0}\boldsymbol{\delta q}^o_{c,in}(\Omega)\right), \tag{4.27}$$

$$\boldsymbol{\delta q}^m(\Omega) = \mathbf{M}_{\Omega,b}^{-1}\left(\mathbf{T}.\boldsymbol{\delta q}^o(\Omega) + \sqrt{2\gamma_m}\boldsymbol{\delta q}^m_{b,in}(\Omega)\right). \tag{4.28}$$

The superscript notation $\boldsymbol{\delta q}^i$ signifies that only the i-part of the full four-dimensional vector is considered, e.g. $\boldsymbol{\delta q}^o = (\delta\hat{X}_1^a, \delta\hat{X}_2^a)$. Now, inserting (4.28) into (4.27) and solving for the optical intra-cavity quadratures we find

$$\begin{aligned}\boldsymbol{\delta q}^o(\Omega) = \mathbf{A}^{-1}.\Big(&\sqrt{2\gamma_m}\mathbf{B}.\boldsymbol{\delta q}^m_{b,in}(\Omega) \\ &+ \mathbf{M}_{\Omega,a}^{-1}.[\sqrt{2\kappa_c}\boldsymbol{\delta q}^o_{a,in}(\Omega) + \sqrt{2\kappa_0}\boldsymbol{\delta q}^o_{c,in}(\Omega)]\Big).\end{aligned} \tag{4.29}$$

In order to simplify the notation somewhat, we have introduced new matrices

$$\mathbf{A} = \mathbf{I}_2 - \mathbf{M}_{\Omega,a}^{-1}.\mathbf{T}.\mathbf{M}_{\Omega,b}^{-1}.\mathbf{T}, \tag{4.30}$$

$$\mathbf{B} = \mathbf{M}_{\Omega,a}^{-1}.\mathbf{T}.\mathbf{M}_{\Omega,b}^{-1}, \tag{4.31}$$

where $\mathbf{I}_2$ is the unit matrix of dimension 2, and the other constituent matrices are given by

$$\mathbf{T} = \begin{pmatrix} 0 & 0 \\ -2g_0\alpha & 0 \end{pmatrix} \tag{4.32}$$

$$\mathbf{M}_{\Omega,a}^{-1} = \frac{1}{(\kappa - i\Omega)^2 + \Delta^2}\begin{pmatrix} \kappa - i\Omega & -\Delta \\ \Delta & \kappa - i\Omega \end{pmatrix} \tag{4.33}$$

$$\mathbf{M}_{\Omega,b}^{-1} = \frac{1}{(\gamma_m - i\Omega)^2 + \omega_m^2}\begin{pmatrix} \gamma_m - i\Omega & \omega_m \\ -\omega_m & \gamma_m - i\Omega \end{pmatrix}. \tag{4.34}$$

Finally, we can invoke the input-output relation for the optical fluctuation quadratures

$$\boldsymbol{\delta q}^o_{out}(\Omega) = \boldsymbol{\delta q}^o_{a,in}(\Omega) - \sqrt{2\kappa_c}\boldsymbol{\delta q}^o(\Omega) \tag{4.35}$$

to map the intracavity field onto the measurable output field. This results in the expression

$$\boldsymbol{\delta q}^{o}_{out}(\Omega) = \mathbf{J}_a.\boldsymbol{\delta q}^{o}_{a,in}(\Omega) + \mathbf{J}_b.\boldsymbol{\delta q}^{m}_{b,in}(\Omega) + \mathbf{J}_c.\boldsymbol{\delta q}^{o}_{c,in}(\Omega), \tag{4.36}$$

describing the mapping of input fluctuations to the system onto the output field through corresponding transfer matrices

$$\mathbf{J}_a = \mathbf{I}_2 - 2\kappa_c(\mathbf{A}^{-1}.\mathbf{M}^{-1}_{\Omega,a})\,, \tag{4.37}$$

$$\mathbf{J}_b = -2\sqrt{\kappa_c\gamma_m}(\mathbf{A}^{-1}.\mathbf{B})\,, \tag{4.38}$$

$$\mathbf{J}_c = -2\sqrt{\kappa_c\kappa_0}(\mathbf{A}^{-1}.\mathbf{M}^{-1}_{\Omega,a}). \tag{4.39}$$

As expected – and not least required of any sensible model of the system – no information about the mechanical oscillator is transferred to the optical output in the absence of coupling to the optomechanical cavity, $\kappa_c = 0$. In this case the fluctuations of the optical input field are directly transferred to the output, $\boldsymbol{\delta q}^{o}_{out}(\Omega) = \boldsymbol{\delta q}^{o}_{a,in}(\Omega)$. Most importantly, we observe that the input fluctuations determine the noise floor for measurements of transduced mechanical motion, $\kappa_c \neq 0$. This means that when probing the mechanical motion with a coherent input state of a given amplitude, the signal-to-noise ratio of the transduction signal will always be limited by the vacuum fluctuations of the input.

4.3.4 Homodyne detection of the output field

In the preceding, we have not made any particular choice of phase reference. But since we will be interested in measuring the output field quadrature fluctuations using homodyne detection with a local oscillator derived from the input field, the obvious choice is to assume the input field to be real. Rewriting (4.15) and using the input-output relation (4.14) we find

$$\alpha = \alpha_{in}|F_1(\Delta)|e^{i\phi_1}, \qquad \phi_1 = \arctan\left(\Delta/\kappa\right), \tag{4.40}$$

$$\alpha_{out} = \alpha_{in}|F_2(\Delta)|e^{i\phi_2}, \qquad \phi_2 = \arctan\left(\frac{-2\eta_c\Delta/\kappa}{1-2\eta_c-(\Delta/\kappa)^2}\right), \tag{4.41}$$

where $|F_1(\Delta)|$ and $|F_2(\Delta)|$ are amplitude transfer functions, and the expressions for ϕ_1 and ϕ_2 provide the necessary relations between the input, intracavity, and output phases. Thus, the output field can always be transformed into the desired basis by introducing appropriate rotation matrices in (4.36). From (4.32) we see that the transduction gain is proportional to the intracavity mean field amplitude, and in order to maximize the signal-to-noise ratio we will therefore only consider resonant driving ($\Delta = 0$) of the optomechanical system. In this case the relative phases (4.40)-(4.41) both vanish, eliminating the need for basis transformations.

As described in Section 2.2.3, homodyne detection projects out a particular quadrature $\hat{Q}_\theta$ of the signal field determined by the local oscillator phase θ:

$$\hat{Q}_\theta(\Omega) = \left(\cos(\theta)\,,\sin(\theta)\right).\boldsymbol{\delta q}^{o}_{out}(\Omega) = \cos(\theta)\delta\hat{X}_1^{a,out} + \sin(\theta)\delta\hat{X}_2^{a,out}. \tag{4.42}$$

Assuming that all input fluctuations are uncorrelated, we can use (4.36) and (4.42) to express the measured quadrature variance as

$$\mathrm{Var}(\hat{Q}_\theta) = \eta_{mm}\eta_{QE} \sum_{k=\{a,b,c\}} \mathrm{Var}\Big((\cos(\theta)\,, \sin(\theta)).\mathbf{J}_k.\boldsymbol{\delta q}_{k,in}(\Omega)\Big) + (1 - \eta_{mm}\eta_{QE}). \quad (4.43)$$

Here we have also accounted for measurement imperfection through mode matching efficiency η_{mm} and detector quantum efficiency η_{QE} and the resulting admixed vacuum noise contribution. The quadrature variances of the three fluctuation inputs are given by:

$$\boldsymbol{\delta q}_{a,in} : \begin{cases} \mathrm{Var}(\delta X_1^a) = \mathrm{Var}(\delta X_2^a) = 1 \\ \mathrm{Var}(\delta X_1^a) = e^{2r}; \quad \mathrm{Var}(\delta X_2^a) = e^{-2r} \end{cases}, \quad (4.44)$$

$$\boldsymbol{\delta q}_{b,in} : \mathrm{Var}(\delta X_1^b) = \mathrm{Var}(\delta X_2^b) = 1 + \langle n \rangle, \qquad \langle n \rangle = \frac{1}{e^{\hbar\omega_m/k_bT} - 1}, \quad (4.45)$$

$$\boldsymbol{\delta q}_{c,in} : \mathrm{Var}(\delta X_1^c) = \mathrm{Var}(\delta X_2^c) = 1, \quad (4.46)$$

The two cases for the optical driving field correspond to a coherent state and a phase squeezed state, respectively. We have assumed that the system is in thermal equilibrium with the environment at temperature T resulting in thermal state fluctuations of the mechanical oscillator (cf. Section 1.4.4).

Squeezing-enhanced transduction 5

> "It [quantum efficiency] determines our signal to shot noise ratio, which sets an upper bound on the SNR of the measurement. There are very special situations ("squeezed states") in which this has to be qualified, but they aren't of much practical use."
>
> – P. C. D. Hobbs
> in *"Building electro-optical systems: making it all work."* [57]

In this chapter we discuss how the optomechanical transduction sensitivity can be enhanced by employing squeezed probe states. Using the model developed in Section 4.3 we investigate numerically the enhancement efficiency in different cavity coupling regimes and as function of the mechanical frequency to optical linewidth ratio. The aim is to identify the operation regime for which this particular quantum sensing scheme yields the largest possible improvement compared to coherent state probing.

An elaboration of the work presented in this chapter has been published in the journal article:

- H. Kerdoncuff, U. B. Hoff, G. I. Harris, W. P. Bowen, and U. L. Andersen. Squeezing-enhanced measurement sensitivity in a cavity optomechanical system, *Annalen der Physik*, 527:107-114, 2015. Special issue: Quantum and Hybrid Mechanical Systems.

5.1 How does squeezing improve the transduction sensitivity?

As mentioned in Section 4.3 the optomechanical transduction signal rides on a noise floor set by optical input fluctuations, which in the case of a quantum noise limited probe amounts to one unit of shot noise. This noise imposes a limit on the transduction sensitivity achievable using classical probe fields of a fixed amplitude. We have already seen that the manifestation of quantum noise can be understood in terms of randomly fluctuating sidebands that beat with the carrier in the detection process, and from (1.46) we find that the noise contributions from upper and lower

sidebands to the total spectral variance of a phase quadrature measurement ($\theta = \pi/2$) are given by:

$$\mathrm{Var}(\delta\hat{X}_2(\Omega)) = \frac{1}{4}\Big[\mathrm{Var}(\delta\hat{X}_2^+) + \mathrm{Var}(\delta\hat{X}_2^-) + 2\mathrm{Cov}(\delta\hat{X}_2^+, \delta\hat{X}_2^-) + \mathrm{Var}(\delta\hat{X}_1^+) + \mathrm{Var}(\delta\hat{X}_1^-) - 2\mathrm{Cov}(\delta\hat{X}_1^+, \delta\hat{X}_1^-)\Big]. \quad (5.1)$$

The key to understanding how squeezing can help improving the transduction signal lies in the two covariance terms. If the upper and lower sidebands are completely uncorrelated, which is the case for a coherent probe, then both these terms evaluate to zero and the total variance is one. However, if correlations are introduced in such a way that both terms subtract from the total sum then the net variance will be less than one and thereby reduced below the shot noise level. A bright phase squeezed probe state – that is a bright carrier surrounded by phase squeezed vaccuum fluctuations at sideband frequencies – has exactly the desired properties: as illustrated in Fig. 5.1 the optomechanical phase modulation of the carrier generates weak coherent sideband states constituting the actual transduction signal. But in contrast to the coherent state probing scheme (Fig. 4.2) the upper and lower sideband amplitude and phase quadrature fluctuations are now correlated $\mathrm{Cov}(\delta\hat{X}_1^+, \delta\hat{X}_1^-) > 0$ and anti-correlated $\mathrm{Cov}(\delta\hat{X}_2^+, \delta\hat{X}_2^-) < 0$, respectively, as a result of phase squeezing. In a subsequent homodyne phase quadrature measurement, a signal component at ω_m is generated in the photocurrent spectrum due to beating of the optical transduction signal sidebands ($\omega_0 \pm \omega_m$) with the local oscillator at frequency ω_0. The noise floor is (apart from electronic noise in the detection circuit) determined by the simultaneous beating of the local oscillator with fluctuating sidebands surrounding the upper and lower signal components. But thanks to the induced correlations these beat signals will interfere destructively, resulting in a measurement noise floor reduced below the shot noise level. We now see that the total measured transduction signal spectrum consists of contributions from two separate parts: a classical measurement of the optomechanically induced phase modulation amplitude which dominates the spectrum in the vicinity of the mechanical resonance frequency and determines the signal level, and a quantum part which determines the noise floor at frequencies away from the mechanical resonance. Thus, comparing coherent state and squeezing-enhanced measurements conducted using identical probe powers we expect an improved sensitivity in the latter case, solely due to a lowering of the noise floor.

5.2 Numerical results

In order to make predictions from the theoretical model it has to be linked to an actual cavity optomechanical system via a set of physical parameters. In this work we have focused on implementing the squeezing-enhanced transduction scheme in the particular type of system known as a microtoroid, as will be discussed in detail

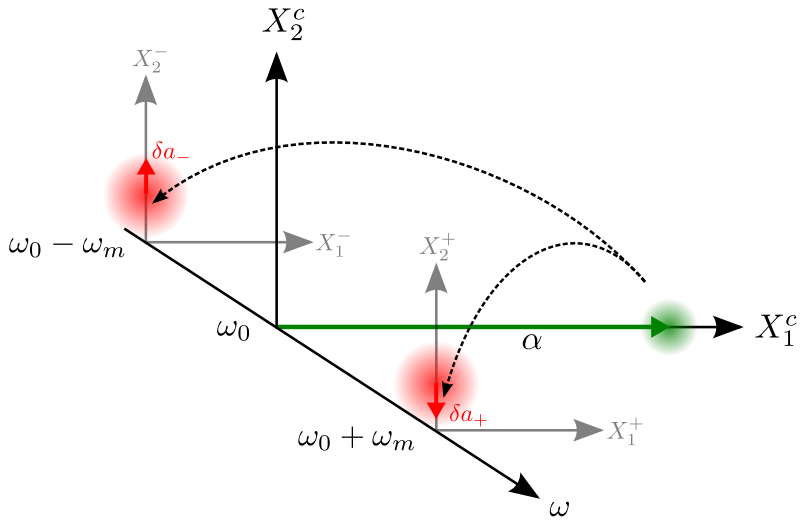

Figure 5.1: Phase space representation of squeezing-enhanced optomechanical transduction. For a phase squeezed state the individual sidebands show thermal state fluctuations exceeding the vacuum fluctuations. The squeezing-effect lies in the inter-sideband correlations and it only manifests itself upon detection.

in Chapter 6. The obvious choice is therefore to pick parameters reminiscent of this type of system. In this case the relevant form of the vacuum optomechanical coupling rate is $g_0 = x_{zpf}\omega_0/R$, with R being the major radius of the microtoroid. The assumed system parameter values are listed in Table 5.1. Furthermore, we will assume a total optical probe power of $P = 10\,\mu$W at $\lambda = 1064\,$nm, and 6 dB of phase squeezing ($r = 0.69$) in the quantum-enhanced case. Detection losses are neglected.

Physical parameter	**Symbol**	**Value**
Micro toroid major radius	R	$30\,\mu$m
Effective mass	M_{eff}	$0.3\,\mu$g [52]
Mechanical resonance frequency	$\omega_m/2\pi$	10 MHz / 50 MHz
Mechanical linewidth (FWHM)	$2\gamma_m/2\pi$	15 kHz
Optical cavity linewidth (FWHM)	$2\kappa_0/2\pi$	200 MHz / 5 MHz
Environment temperature	T	300 K

Table 5.1: Physical parameters used in simulation of the optomechanical transduction sensitivity using a micro toroidal resonator.

An important characterization parameter for cavity optomechanical systems is the ratio of mechanical resonance frequency over optical linewidth, $\omega_m/2\kappa$, distinguishing the resolved-sideband systems $\omega_m/2\kappa > 1$ from the unresolved ones $\omega_m/2\kappa < 1$. The ability to enter the resolved sideband regime of cavity optomechanical systems has been of absolute importance for demonstrating ground-state cooling of mechani-

cal oscillators [126, 30], as it enables implementation of sideband laser cooling [113] techniques in analogy to that employed in ion-trap experiments [35]. In the following we will investigate the effect of squeezing-enhanced transduction in both regimes using the two corresponding parameter sets in Table 5.1, and we will do so as function of the optical cavity coupling coefficient η_c. It is important to note that for a given physical system with a fixed intrinsic optical loss rate κ_0, varying η_c will also affect the sideband resolvedness parameter since the coupling perturbs the intrinsic quality factor of the cavity resulting in the effective total linewidth $\kappa = \kappa_0 + \kappa_c$:

$$\frac{\omega_m}{2\kappa} = \frac{\omega_m}{2(\kappa_0 + \kappa_c)} = \frac{\omega_m}{2\kappa_0}(1 - \eta_c). \tag{5.2}$$

As already mentioned, we are in this work not concerned about the *absolute* achievable transduction sensitivity, commonly quoted in units of $\mathrm{m}/\sqrt{\mathrm{Hz}}$. The quantity of interest is rather the *relative* improvement in the signal-to-noise ratio (SNR), measured as the level difference in the homodyne power spectrum of the transduction signal between the peak value at the mechanical resonance frequency and the noise floor, which in the classical probing scheme is given by the shot noise level.

5.2.1 Case I: Unresolved sideband regime

In this regime the transduced signal sidebands are deeply buried inside the optical cavity resonance and so is the relevant part of the squeezing spectrum. Because of that the effective degree of squeezing is progressively degraded due to loss as coupling to the cavity (η_c) is increased. Classically, the best sensitivity is achieved at critical coupling since that maximizes the intracavity field and thereby the transduction signal amplitude. However, at critical coupling destructive interference occurs between the field that is reflected directly off the cavity input boundary and that part leaking out the cavity, which in the ideal case results in a dark output from the cavity exactly at resonance. Since the transduction signal is comparatively close to the cavity resonance the corresponding part of the squeezing will be heavily suppressed resulting in a vanishingly small quantum-enhancement effect.

The simulated transduction spectrum for a system operated in the under coupled regime with $\eta_c = 0.025$ is shown in Fig. 5.2. As expected the coherent and quantum-enhanced signals overlap at the mechanical resonance and an improvement in SNR results by a lowering of the noise floor as discussed in Section 5.1. A simulation of the SNR values as function of η_c is shown in Fig. 5.3. Calculating the difference in achievable SNR for coherent and bright squeezed probing, we find that a significant quantum enhancement over the classically achievable level only occurs in the limiting regimes where $\eta_c \simeq 0$ and $\eta_c \simeq 1$. However, it is important to note that an absolute enhancement is not achievable in the sense that the squeezed probe SNR value is always smaller than that of the coherent probe at critical coupling.

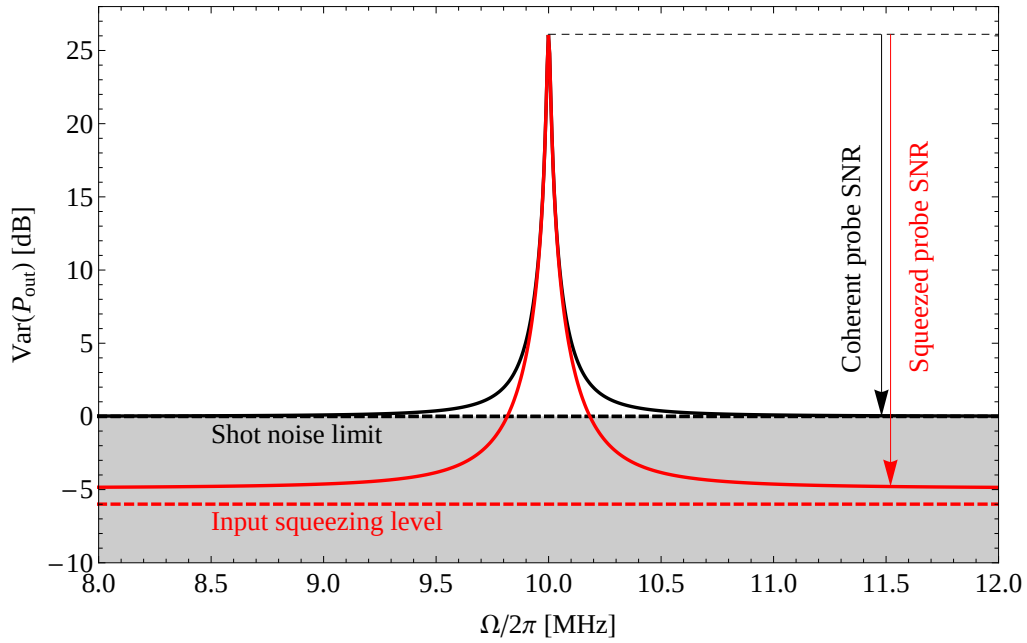

Figure 5.2: Simulated transduction spectrum for a non-resolved sideband optomechanical system, using coherent (black) and bright squeezed (red) probe light, operated in the under-coupled regime with $\eta_c = 0.025$.

5.2.2 Case II: Resolved sideband regime

We now turn to the resolved sideband case where the transduced signal sideband lies outside the optical cavity linewidth. Following the reasoning in the previous paragraph we expect a better performance of the quantum-enhanced probing scheme in this regime since the squeezing is no longer subject to large intracavity losses. A crucial requirement is, however, that the bandwidth of the employed squeezed light source is sufficiently large that strong squeezing is generated at frequencies exceeding the transduced signal sideband (in this case 50 MHz). For typical microtoroidal resonators where the dominant mechanical radial breathing modes have frequencies below 100 MHz this requirement can be met since squeezed-light sources with bandwidths exceeding 150 MHz has been demonstrated in several cases [92, 135]. The situation is quite different for photonic-crystal optomechanical systems where the mechanical oscillation frequencies are in the GHz range [30]. So far only weakly squeezed continuous-wave states with such a large bandwidth has been demonstrated [8], though progress is being made in that direction, cf. Part III of this thesis.

Figure 5.4 shows the simulated transduction spectrum for operation close to the critical coupling point. The cavity induced degradation of the input squeezing is observed at low frequencies but the full initial quantum noise reduction is recovered in the high end of the spectrum resulting in a corresponding enhancement of the transduction SNR. Achievable SNR values for coherent and squeezed light probing

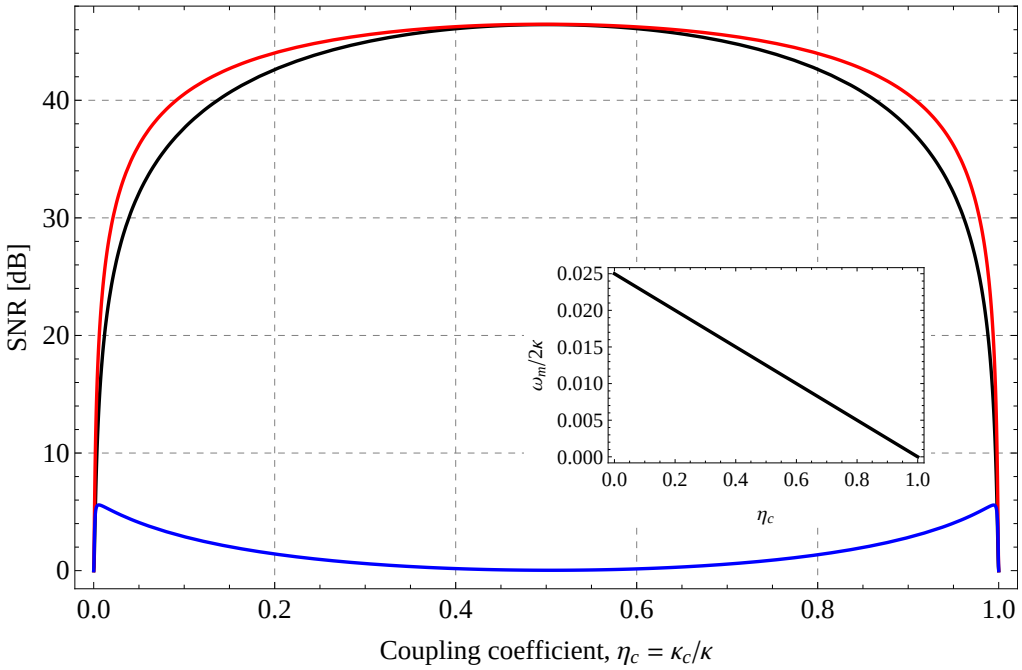

Figure 5.3: Simulated signal-to-noise ratio for optomechanical interaction in the non-sideband resolved regime as function of coupling coefficient η_c, using coherent (black) and bright squeezed (red) probe light. The achievable increase in signal-to-noise ratio by quantum-enhanced probing is plotted in blue. The inset shows the corresponding change in sideband-resolvedness as the cavity coupling is increased.

as function of η_c are plotted in Fig. 5.5. An enhancement corresponding to the input degree of squeezing is observed for basically all coupling values. Most importantly, and in contrast to the unresolved sideband system, an absolute enhancement is actually achieved in this case illustrating the full potential of implementing quantum-sensing strategies in cavity optomechanical applications. For coupling coefficients larger than $\eta_c \approx 0.8$ a small drop in SNR enhancement is observed. The inset graph shows that this happens because the system inevitably drops out of the resolved sideband regime when the coupled-cavity linewidth gets sufficiently large to encompass the transduction signal sideband. By increasing the coupling further the enhancement is recovered in accordance with the unresolved sideband simulations.

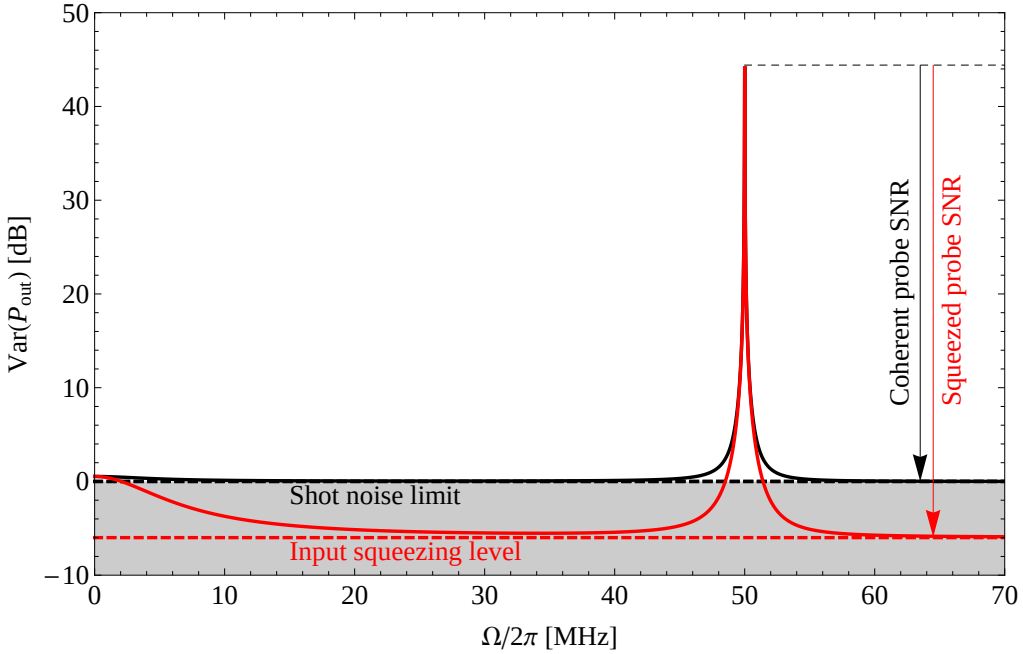

Figure 5.4: Simulated transduction spectrum for a resolved sideband optomechanical system, using coherent (black) and bright squeezed (red) probe light, operated close to critical coupling $\eta_c \approx 0.5$.

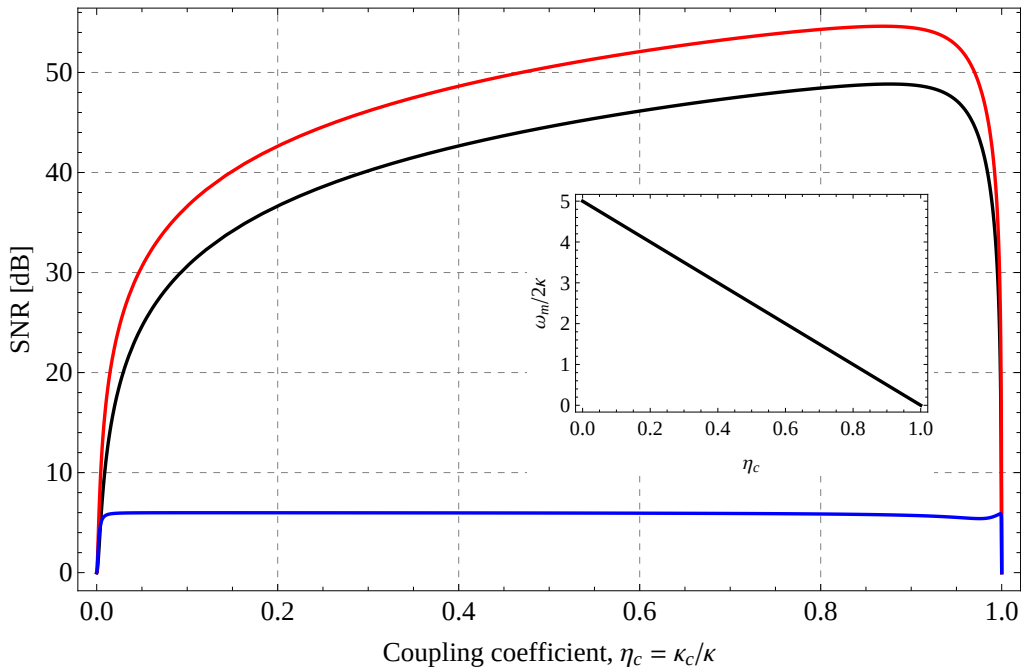

Figure 5.5: Simulated signal-to-noise ratio for optomechanical interaction in the sideband resolved regime as function of coupling coefficient η_c, using coherent (black) and bright squeezed (red) probe light. The achievable increase in signal-to-noise ratio by quantum-enhanced probing is plotted in blue. The inset shows the corresponding change in sideband-resolvedness as the cavity coupling is increased.

Experimental demonstration of squeezing-enhanced transduction

6

In this chapter we present – to the best of our knowledge – the first experimental work on interfacing a micromechanical system with squeezed states of light. The reported results constitute a proof-of-principle demonstration of squeezing-enhanced micromechanical displacement sensing, which could be a valuable resource for future scrutiny of quantum-behavior in macro-physical systems. Furthermore, the offered improvement of the transduction signal-to-noise ratio can be directly exploited for boosting the cooling efficiency of electro-static feedback cooling techniques [82].

Part of the work presented in this chapter has been published in the journal article:

- U. B. Hoff, G. I Harris, L. S. Madsen, H. Kerdoncuff, M. Lassen, B. M. Nielsen, W. P. Bowen, and U. L. Andesen. Quantum-enhanced micromechanical displacement sensitivity, *Optics Letters*, 38(9):1413-1415, 2013.

6.1 Micro-toroidal resonators

Out of the existing multitude of optomechanical microcavities the particular variant chosen for implementation of squeezing-enhanced transduction sensitivity in this work, has been the silica microtoroidal resonator (Fig. 6.1), first demonstrated in 2003 by the group of Kerry Vahala at the California Institute of Technology [7, 6]. Due to their integration of high-Q optical whispering gallery modes[1] with mechanical vibrational modes, microtoroidal resonators have been proven to be well-suited on-chip systems for high-sensitivity displacement sensing [112]. On the mechanical side, engineering of dissipation properties has enabled demonstration of mechanical Q-values of up to 80000 [3], measured in a cryogenic environment. For the present application, state-of-the-art optical and mechanical properties has not been a requirement. The optical quality should just be sufficiently good that a significant degree of squeezing is preserved after the optomechanical interaction. And mechanically, the main requirement is the existence of a strong resonance within

[1] A detailed description of whispering gallery modes in microcavities can be found in the thesis of T. J. Kippenberg [72].

the bandwidth of the available squeezed-light source. Characteristic properties of our microtoroidal resonators, provided by the group of Warwick Bowen, University of Queensland, are listed in Table 6.1.

As briefly touched upon in Section 1.2.2, the optical guiding principle of whispering gallery mode resonators is gracing-incidence total internal reflection, resulting in a highly localized mode at the silica-air interface of the resonator and with an evanescent tail extending into the surrounding air. This is an essential property of the system as it allows efficient optical coupling via overlapping the evanescent field with that of a tapered optical fiber. For further details on the underlying theory for this coupling mechanism we refer the reader to the existing literature on the topic, e.g. [120]. In this work, bare SMF-28 fibers tapered down to a diameter of approximately 1 μm over a length of 20 mm, subject to the constraint of single-mode operation, were used for coupling to the microtoroids. Details on the particular flame-brushing procedure used for fabrication of the tapered fibers are provided in the thesis of M. McGovern [91].

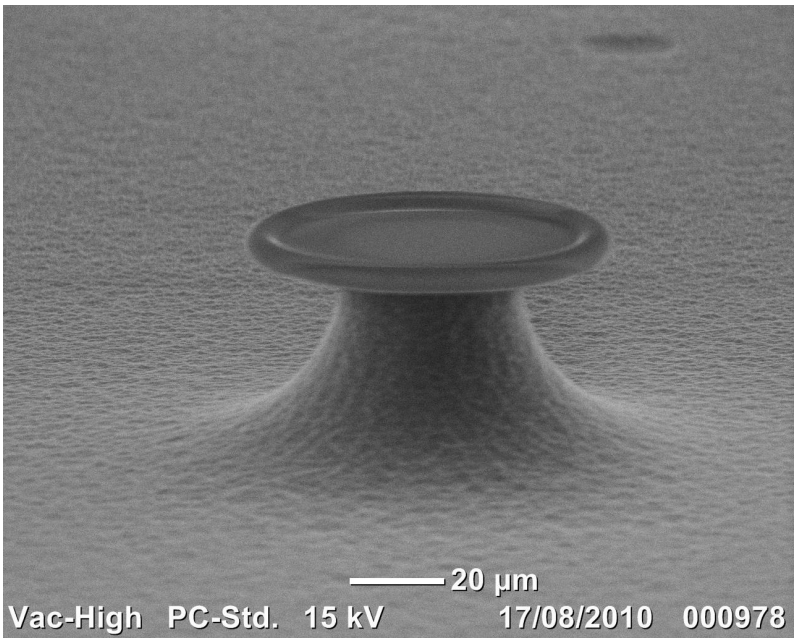

Figure 6.1: SEM micrograph of a microtoroid fabricated at University of Queensland, similar to the ones employed in the reported experiments. Image courtesy of Glen I. Harris.

Property	**Value**
Chip layer stack	SiO_2/Si
Major radius	$\simeq 30\,\mu$m
Minor radius	$\simeq 3\,\mu$m
Pedestal height	$30\,\mu$m
Optical FSR at 1064 nm	$\simeq 1$ THz
Optical linewidth (FWHM)	180 MHz [69]
Optical Q	$\simeq 1.5 \cdot 10^6$
Primary mechanical resonance frequency	$\simeq 5.2$ MHz
Mechanical linewidth (FWHM)	$\simeq 15$ kHz
Mechanical Q	$\simeq 350$
Effective mass	$<100\,\mu$g

Table 6.1: Characteristic physical properties of the employed microtoroidal resonator. The estimated upper bound on the effective mass of the relevant mechanical mode was derived on the basis of FEM simulations conducted by G. I. Harris.

6.2 Experimental setup

The experimental setup conceived for implementation of squeezed-light interfacing of microtoroidal resonators is simplistically illustrated in Fig. 6.2. It was constructed as a sub-setup in a pre-existing experimental quantum optics framework, hosting a number of other experimental activities in our group [89, 88, 76, 81]. Common to all is that they run off an Innolight Diabolo Nd:YAG laser with a nominal fundamental (signal) output of 450 mW at 1064 nm and a second harmonic (SHG) output of 800 mW at 532 nm. For further details on the laser system, the reader is referred to the thesis of M. Lassen [80]. After spectral and spatial filtering using a mode cleaning cavity, actively stabilized using a Pound-Drever-Hall locking technique [17] employing phase modulation sidebands at 22.03 MHz, the signal beam was quantum noise limited from a sideband frequency of around 3 MHz and up. Using an optical parametric oscillator, based on the $\chi^{(2)}$ nonlinearity of PPKTP, squeezed states of the signal field were generated and subsequently distributed to the client setups via free-space channels. Optimal squeezing was generated at a sideband frequency of 4.9 MHz, and at the time when this work was conducted, the routinely generated degree of single mode vacuum squeezing, as measured in the proximity of the OPA, was about 4.5 dB. In what follows, the squeezed light source will simply be considered as an available resource and we refrain from dwelling upon further details but refer the interested reader to the theses of J. Janousek [65] and L. S. Madsen [87].

As elaborated on in the preceding chapters, a resonant optomechanical interaction results in frequency dependent phase modulation of the probe field, rendering balanced homodyne detection an appropriate interrogation strategy. And even more so, when probing of the optomechanical system with a bright phase-squeezed state is targeted, and quantum noise limited detection of the field quadratures is required. To this end, the signal was split into a strong local oscillator beam (LO) and a weaker probe beam. For the latter, two distinct optical paths were established, cf. Fig. 6.2: (1.) bypassing the OPA for coherent probing of the optomechanical system, and (2.) seeding the OPA for probing with a bright phase squeezed state[2]. Squeezing in the phase quadrature was achieved by appropriate locking of the relative phase between the signal field and the SHG pump for the OPA. In either case, the probe was coupled into the bare tapered fiber by means of a mode matching telescope and an antireflection V-coated aspheric singlet lens[3]. Polarization control, important for optimizing coupling to the microtoroid, was implemented by a combination of zero-order $\lambda/2$ and $\lambda/4$ wave plates immediately before the aspheric singlet. The chip containing the microtoroidal resonators was held on piezo-controlled tree-axis translation stage[4] next to the tapered fiber. In this way we were able to precisely control the taper-toroid distance, and thereby the optical coupling strength, by moving the

[2]To preserve squeezing in the probe field, all mirrors following the OPA were high-reflectors: Layertec GmbH, #100362, HRr(45°, 1064 nm)>99.9%.
[3]Thorlabs C240TME-1064, $f = 8.07$ mm
[4]Thorlabs, model NanoMax MAX311D/M, closed loop.

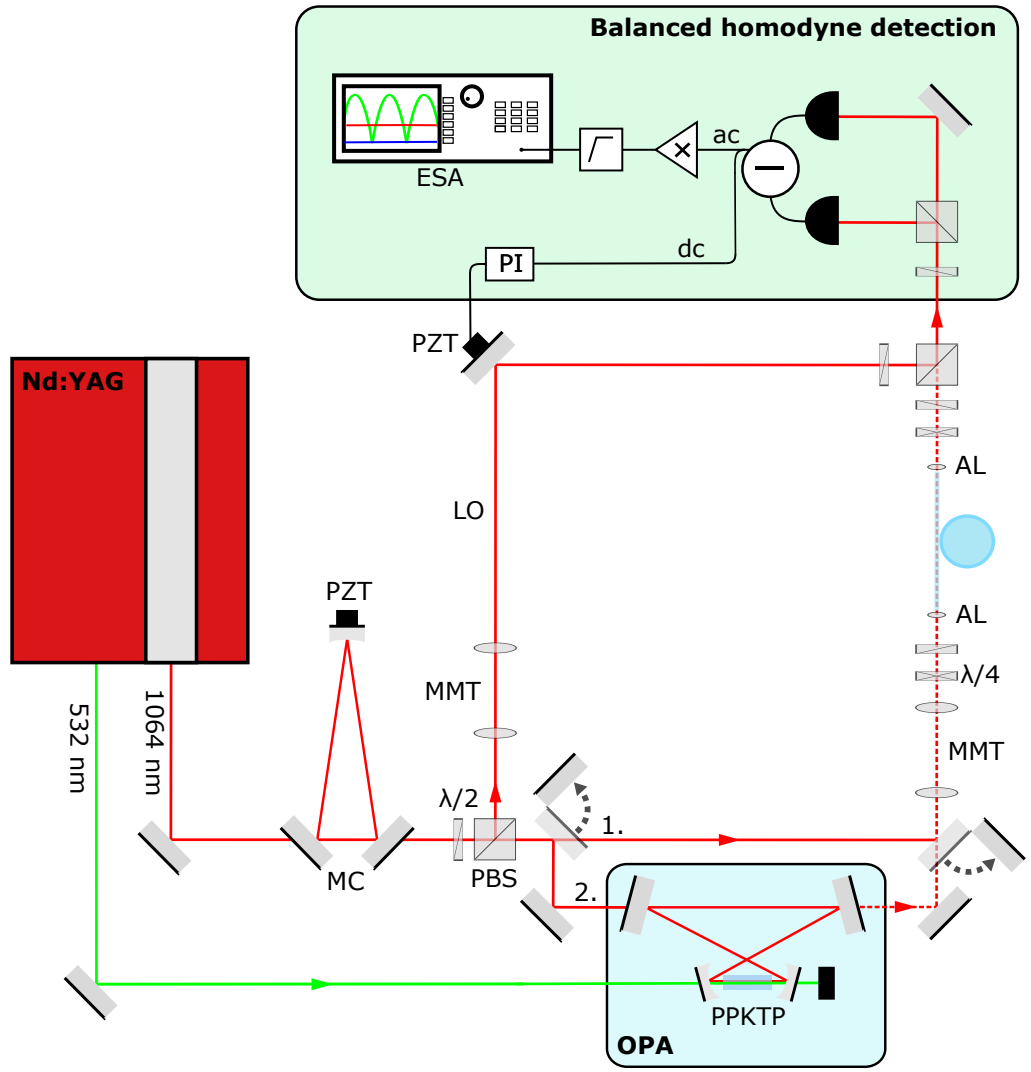

Figure 6.2: Simplified schematic representation of experimental setup devised for squeezed-light interfacing of microtoroidal resonators. MC, mode cleaning cavity; PZT, piezoelectric transducer; PI, proportional-integral servo controller; PBS, polarizing beamsplitter; MMT, mode matching telescope; LO, local oscillator beam for balanced homodyne detection; AL, aspherical lens. The figure is adapted from [59].

microtoroids with respect to the spatially fixed tapered fiber. On the output side of the fiber, the probe was coupled back to free-space using the exact same aspheric singlet, and then spatially overlapped with the orthogonally polarized local oscillator on a polarizing beamsplitter (PBS). The combined field was directed to the balanced homodyne detection setup, and the polarization components were made to interfere using a $\lambda/2$-plate, set for 45 degree polarization rotation, and a polarizing beamsplitter. The two equally intense outputs were directed on to separate photodetectors[5] and the ac photocurrents were subtracted[6], amplified[7], high-pass filtered[8], and finally measured on an electronic spectrum analyzer[9]. The dc photocurrents were used as feedback signal for stabilizing the local oscillator phase by means of a servo and a piezo-actuated turning mirror. In this way the homodyne detector was locked for phase quadrature measurement.

6.2.1 Balancing the homodyne detector

The ability of the balanced homodyne detector to perform shot noise limited quadrature measurements stems from the strong suppression of correlated classical noise in the input signal (common-mode rejection) resulting from measuring a *differential* signal. And the suppression strength in turn relies on careful *balancing* of the two individual signals. Using an optical power meter the two impinging beams can only be balanced in power to within approximately $\pm 5\%$. And comparing the dc-outputs from the detectors on an oscilloscope does not in general provide information on balancing of the spectral components as the detectors are likely to have different ac-gains. However, a neat way of balancing the homodyne detector is to consider only the local oscillator input, i.e. blocking the probe, and apply to it a broadband white noise amplitude modulation[10]. Monitoring the spectrum of the homodyne output, the individual modulated spectra can then be measured by blocking one and the other input (Fig. 6.3 green and red traces) as well as the differential signal (blue), providing a direct measure of the suppression strength to optimize on. The relative phase of the two signals being subtracted is particularly important and can be optimized by iteratively changing the length of the cables from the detectors to the subtraction box. Through this procedure, we achieved a noise suppression in excess of 25 dB.

[5] The employed photodetectors were made by M. Lassen and fitted with Epitaxx ETX-500 InGaAs photodiodes, $\eta_{QE} = 87 \pm 2\%$.
[6] Mini-Circuits, model ZSCJ-2-1. Power splitter/combiner, 1-200 MHz.
[7] Mini-Circuits, model ZFL-500LN-BNC. Low noise amplifier, 0.1-500 MHz.
[8] Dunestar, model 400-HPF. 7-pole high-pass filter with a cut-off frequency at 1.8 MHz.
[9] Agilent, model N9000A-503, 9 kHz - 3 GHz
[10] Here implemented by an electro-optical modulator (New Focus, model 4004. Broadband phase modulator, DC-100 MHz) driven by a white-noise input signal (Stanford DS345).

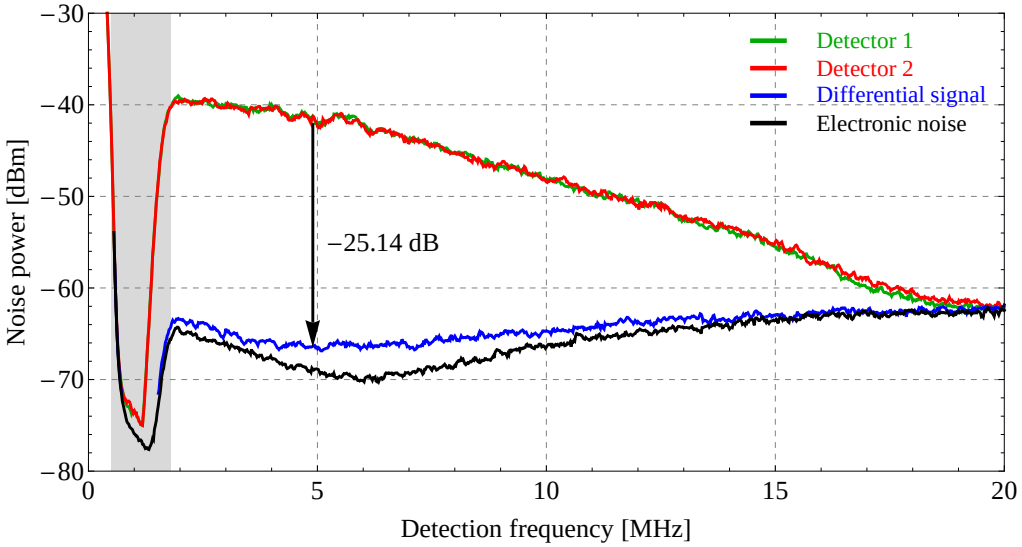

Figure 6.3: Common-mode noise suppression of the balanced homodyne detector. The shaded area indicates the suppression band of the high-pass filter. Data was recorded with RBW = 300 kHz and VBW = 300 Hz.

6.3 Quantum sensing of micro-mechanical displacements

The experimental configuration outlined in the previous section was built with the primary purpose of interfacing the microtoroidal resonators with squeezed light. However, an important prerequisite for doing so is to demonstrate the ability to address the system using coherent light and with firm control of the taper-toroid coupling efficiency. In this section we first document that we indeed have this level of control over the system, and we then characterize the effect of optical loss suffered by the squeezed state as it is propagated through the setup. Finally, we turn to a discussion of the primary results obtained from this project, constituting a proof-of-principle demonstrating of squeezed-light enhanced transduction of micromechanical motion.

6.3.1 Coupling to the micro-toroidal resonator

As mentioned, the setup was accommodated in an existing framework, and it was quickly realized that the Innolight Diabolo is not the optimal laser for experimenting with microcavities. With a course thermal tuning range of 60 GHz and a fine piezo tuning range of ±200 MHz [62] it is actually very unlikely to find a resonance of a cavity with a free spectral range in excess of 1 THz! To overcome this overlooked detail in planning the setup, a Peltier element[11] was installed underneath

[11] Marlow Industries, model DT3-2.5

the microtoroid chip providing temperature tuning of the microcavity resonances. Active stabilization of the temperature was implemented by connecting the Peltier element to a temperature controller[12]. In this way we were able to steer and maintain a cavity resonance in the range of the laser, always keeping it at a temperature above the ambient level to avoid condensation issues.

With optical coupling to the microcavities established, the ability to control the actual coupling efficiency was explored. Figure 6.4 shows exemplary data of the relative transmission through the tapered fiber as the taper-toroid separation was decreased (right to left). The measurements clearly confirm our ability to address both the under- and over-coupled regime. The particular system could not achieve critical coupling as the transmission does not go to zero in the intermediate region. On this point, slightly different behavior was observed depending on the particular combination of microtoroidal resonator and tapered fiber.

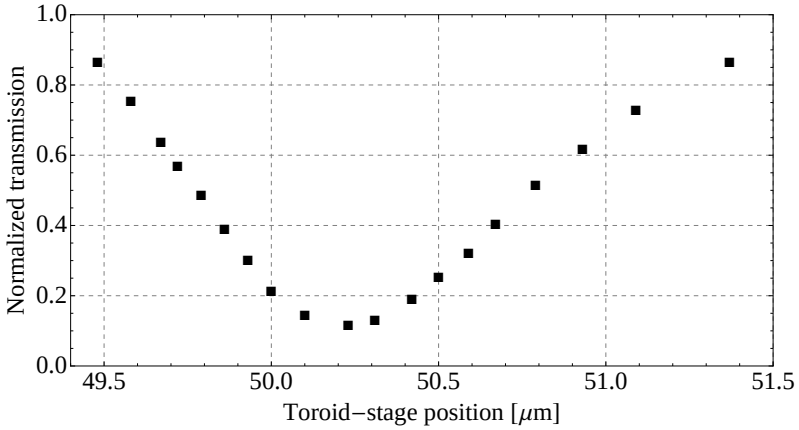

Figure 6.4: Transmission through tapered fiber as function of taper-toroid separation. The absolute separation was not calibrated, and the indicated distance values are stage positions relative to an arbitrary reference point. Data was obtained by direct detection of the transmitted light using a photodiode. The measured transmission levels are normalized to that in the absence of coupling.

Employing instead phase stabilized homodyne detection of the transmitted field we can measure the actual spectral transduction signal in the phase quadrature as function of coupling to the microcavity, as shown in Fig. 6.5, for operation in the under coupled regime. In qualitative agreement with Fig. 5.2 we observe that the signal noise power increases with coupling to the toroid. Here, as in Fig. 6.4, the coupling efficiency is stated in terms of the experimental quantity

$$T = \frac{P_{out}(\kappa_c \neq 0)}{P^0_{out}(\kappa_c = 0)}. \tag{6.1}$$

For a fixed power launched into the tapered fiber, the transmitted power is measured in the absence of coupling to the microtoroid, P^0_{out} $(\kappa_c = 0)$. The chip is then shifted

[12]Wavelength, model LFI-3751.

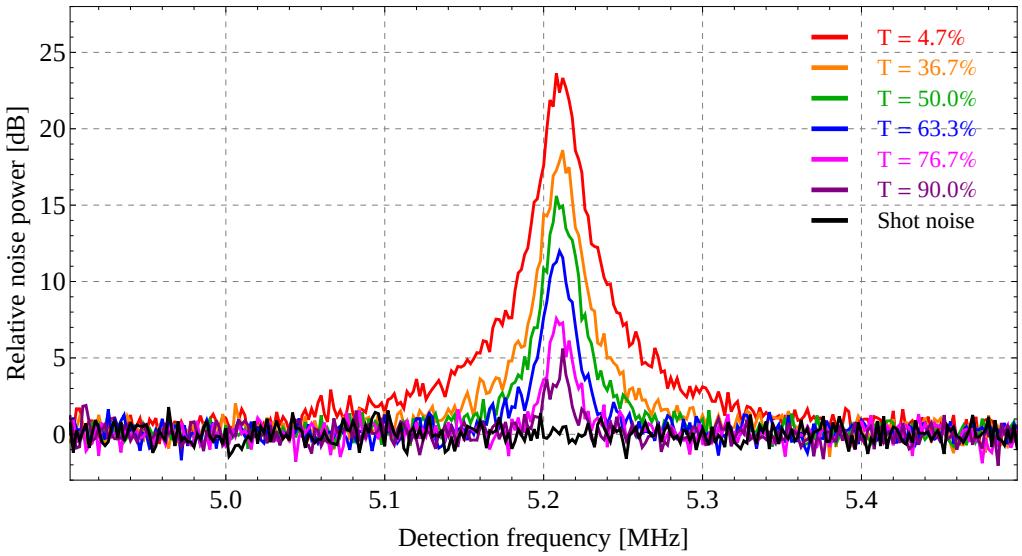

Figure 6.5: Homodyne measurement of the classical transduction signal as function of optical coupling efficiency to the microcavity, for a probe power of 18.3 μW. The homodyne photocurrent was measured on a spectrum analyzer with RBW=10 kHz and VBW=1 kHz.

into the evanescent field from the taper until the desired coupling is reached, and the transmitted power is measured again, P_{out} ($\kappa_c \neq 0$). In order to relate T to the relevant theoretical quantity η_c, we first note that the following relation between steady state input and output power of the mirocavity,

$$P_{out} = \left(1 - \frac{4\eta_c(1-\eta_c)}{1+\Delta^2/\kappa^2}\right) P_{in}, \tag{6.2}$$

can be easily derived from (4.15) and (4.14). Assuming resonant probing and that the combined transmission loss through the fiber, not related to cavity coupling, can be represented by a lumped parameter α, (6.2) takes the form $P_{out} = \alpha(1 - 4\eta_c(1-\eta_c))P_{in}$. In the absence of coupling the expression reduces to $P^0_{out} = \alpha P_{in}$. Now, taking the ratio of the two expressions we find,

$$\frac{P_{out}}{P^0_{out}} = 1 - 4\eta_c(1-\eta_c) = T, \tag{6.3}$$

with solutions

$$\eta_c = \begin{cases} \frac{1}{2}(1-\sqrt{T}) & \text{, under-coupling} \\ \frac{1}{2}(1+\sqrt{T}) & \text{, over-coupling.} \end{cases} \tag{6.4}$$

The correspondence between T and η_c is plotted in Fig. 6.6, and the values used in Fig. 6.5 are indicated in corresponding colors.

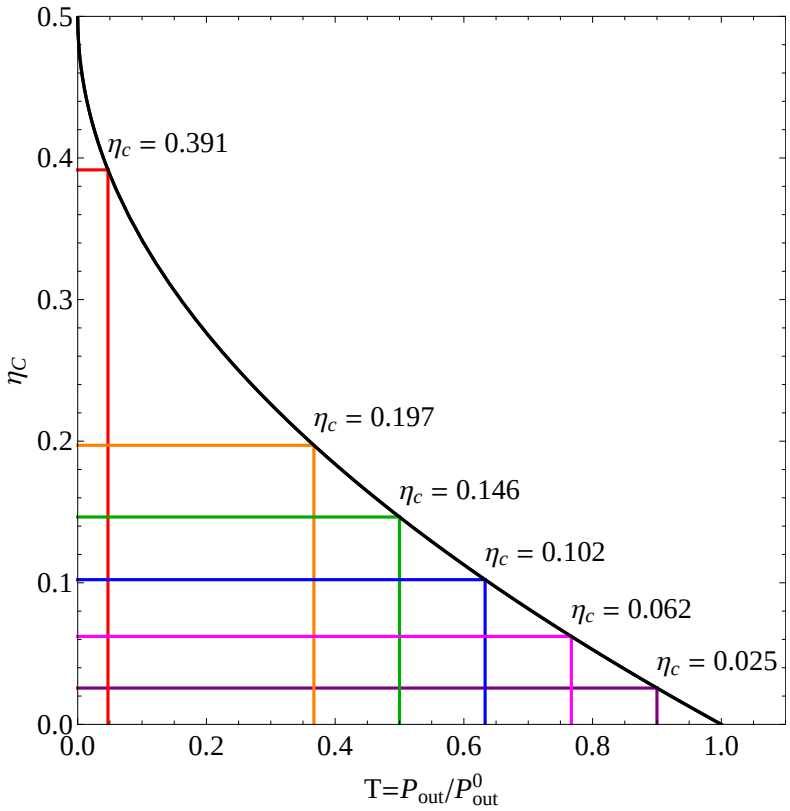

Figure 6.6: Correspondence between the experimentally measured coupling efficiency T and the theoretical coupling parameter η_c.

6.3.2 Loss-induced degradation of squeezed light

The vulnerability of squeezed states to optical loss is a major challenge in any practical application. Obtaining an observable degree of quantum-enhancement in a sensing application is not *per se* guaranteed by the mere injection of squeezed light into the system, but strongly relies on optical losses being kept at a minimal level. A number of significant loss channels are immediately identifiable in the setup considered here, and the corresponding loss budget is given in Table 6.2. Here, we have included only fixed losses, not accounting the loss associated with coupling to the microcavity. The tapered fiber is clearly a bottleneck for the experiment. Compared to commonly achieved coupling efficiencies through single mode fiber, the observed transmission of only 75% is rather low. This can partly be explained by the taper itself, which might not always be adiabatic, and the bare fiber end facets also contribute: firstly, they are not AR coated resulting in about 4% Fresnel loss at either end, and secondly the cleaving does not always result in a perfectly flat facet (Fig. 6.7(a)). Last but not least, we have during the everyday work with the experiment observed that after installing a new tapered fiber, the transmission degrades steadily over time. The quoted maximal value of 75% was measured straight after installing a new fiber. Similar observations were reported by Fujiwara et al. in [42] where they, based on a systematical investigation of the surrounding dust-particle density, conclude that the degradation can be attributed to accumulation of dust on the fiber. Imaging the tapered region from above, we indeed observe a significant amount of scattering centers (Fig. 6.7(b)), consistent with dust particles stuck on the fiber surface. This indicates that the plexiglas enclosure containing the taper-toroid coupling region only provides an insufficient shielding of the setup. The accumulated dust can to some extent be cleaned off[13], partially recovering the initial transmittance of the fiber.

Loss channel	**Efficiency**
Fiber transmission	< 0.75
Optical components (e.g. 0.25% loss per waveplate)	0.987
Homodyne visibility, $\mathcal{V} = 0.98$	0.96
Photodiode quantum efficiency	0.87
Total loss	< 0.62

Table 6.2: Loss budget for the squeezed beam, not accounting for loss induced by coupling to the microcavity.

In order to verify that squeezing is preserved in the probe field, despite the large losses, homodyne tomography was performed of the field transmitted through the

[13]This was done by a delicate process where a droplet of solvent on the chip carrier platform was gently lifted through the fiber and swept across the tapered region. The force required to overcome the surface tension of the droplet, to actually get the fiber inside it, sometimes caused the fiber to break.

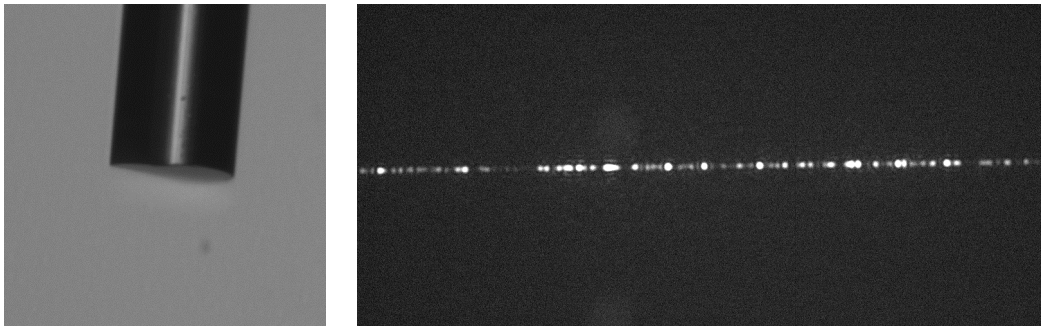

(a) (b)

Figure 6.7: (a) End facet of a stripped cleaved fiber. The diameter is 250 μm. (b) Optical scattering observed from tapered region of the fiber.

taper in absence of coupling to the microcavity. As shown in Fig. 6.8, slightly more than 1 dB of quantum noise reduction is indeed observed.

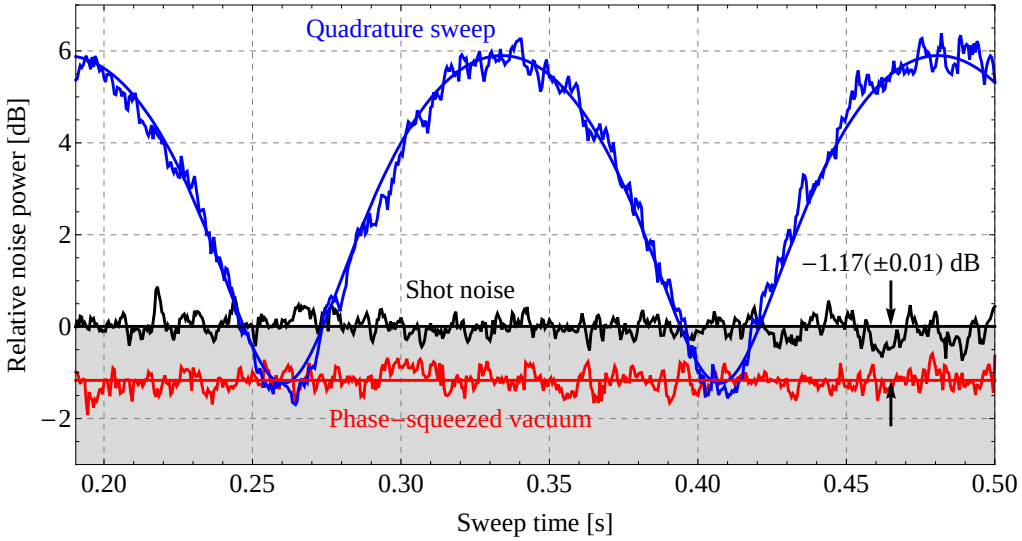

Figure 6.8: Homodyne tomography of squeezed light transmitted through the tapered fiber. The homodyne photocurrent noise power was measured at 4.9 MHz with RBW= 100 kHz and VBW = 100 Hz. Probe power, 20μW, LO power, 1.2 mW. Electronic noise is not subtracted.

6.3.3 So, why not send the squeezed light down the free-space path?

Facing the challenge of minimizing losses in the optical setup, it is tempting to consider whether simply swapping the probe and local oscillator paths would be an efficient way of mitigating loss-degradation of the squeezed state. In this way

the fiber-related loss would be inflicted on the coherent loss-tolerant beam while the squeezed light propagates in free-space, suffering only negligible loss. Unfortunately, the idea is deceiving – for a number of reasons. One practical issue is that the power required in the local oscillator in order to perform a proper homodyne measurement is far too much to be coupled to the high-Q microcavity. But more importantly, and independent of the system being probed, it is not even theoretically possible to achieve a quantum enhanced signal-to-noise ratio if the signal is not encoded on the squeezed beam. Three variations of the "squeezing in free-space" configuration exist (Fig. 6.9): (I) a squeezed vacuum state propagates in the free-space channel and the system is probed by the bright coherent local oscillator transmitted through the fiber, and (II) a bright squeezed local oscillator propagates in the free space channel and the system is probed by a weak coherent field, both employing homodyne detection. Case (III) uses two equally bright beams where the free-space one is squeezed and read out via heterodyne detection. Keeping in mind the homodyne assumption – that only terms multiplied by the local oscillator carrier contribute to the measured signal – it is clear that (I) is just a homodyne measurement of the squeezed vacuum, while (II) is a homodyne measurement of the classical signal field, at best resulting in a shot noise limited spectrum of the transduction signal. In case (III), the fact that the noise in the two interferometer arms is uncorrelated entails that the phase quadrature measurement (sum-signal) yields just a shot noise limited transduction spectrum riding on top of the squeezed noise in mode a. Thus, none of the three alternatives offer any quantum enhanced signal-to-noise ratio on the measured transduction signal.

6.3.4 Proof-of-principle results with squeezed light

Having justified the chosen experimental configuration and verified, unambiguously, that squeezing is preserved in transmission of the setup, we now turn to a discussion of the main results achieved so far.

Using power levels and a coupling strength to the microcavity identical to the coherent-state measurements in Fig. 6.5, that is $T = 90\%$ or $\eta_c = 0.025$, we have performed quantum-enhanced sensing of the thermally excited mechanical vibrations of a microtoroidal resonator, using a bright phase squeezed probe beam. As shown in Fig. 6.10 a reduction of the noise floor by 0.72 dB was observed, resulting in a quantum-enhanced signal-to-noise ratio. The system was brought on to resonance by a combination of temperature tuning of both laser and toroid, ending up at values $T_{tor} = 22.65\,^{\circ}\mathrm{C}$ and $T_l = 24.04\,^{\circ}\mathrm{C}$. The coupling strength was set by monitoring the transmitted light power on a photodiode, decoupling completely from the toroid, and then bringing the toroid closer and closer to the tapered fiber until the transmitted power had dropped to 90% of the uncoupled level.

According to the theoretical simulations in Chapter 5, the noise power at the mechanical resonance peak should be the same for coherent and bright squeezed probing as it is entirely determined by the carrier amplitude. But in Fig. 6.10 the quantum enhanced signal is actually somewhat larger than the classical one.

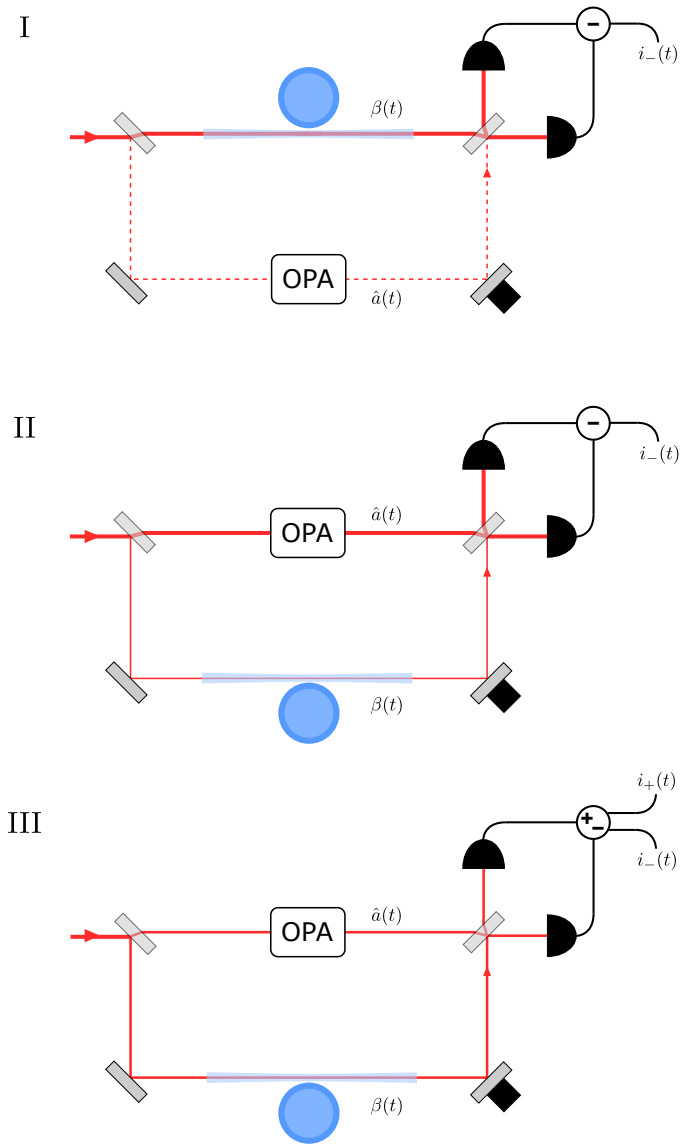

Figure 6.9: Three alternative experimental configurations for squeezing enhanced transduction, where squeezing is not coupled through the lossy tapered fiber. But are they useful?

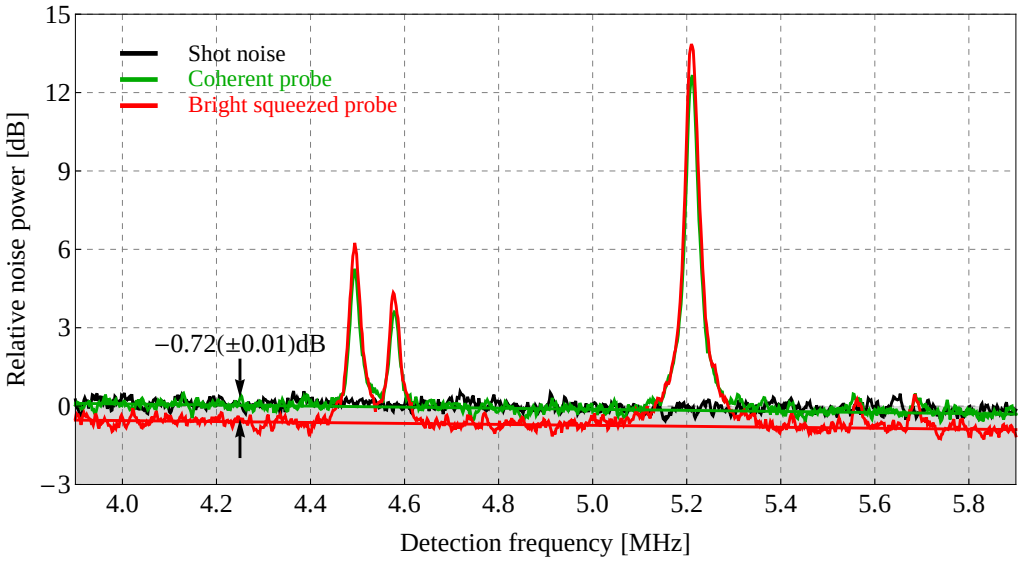

Figure 6.10: Squeezing-enhanced mechanical transduction spectrum. RBW= 100 kHz, VBW = 100 Hz. Probe 20 μW, LO 1.2 mW. The reduction of the noise floor is evaluated by fitting (solid lines) the noise level in between the transduced mechanical resonances, for both coherent and bright squeezed probe light. Figure adapted from [59].

We attribute this difference to a small change in the non-stabilized taper-toroid separation which might have taken place in between the two measurements. In the experiment the classical measurement was recorded first and the input power before the tapered fiber and the coupled transmission power were noted. After switching on the phase squeezing, the input power on the fiber was regulated to the appropriate value, and the homodyne measurement of the phase quadrature spectrum was recorded. The taper toroid distance was not adjusted. It is thus very likely that the separation could have changed a little, resulting in a slightly stronger coupling to the microcavity in the second measurement.

In a future experiment we can imagine exploiting the quantum enhancement of the transduction SNR for e.g. efficient cooling of the mechanical vibrations via application of electro-static feedback gradient forces. In that case it is important that the coupling is stabilized, which could be achieved in a straightforward manner by implementation of a PDH-like locking scheme. However, in the present case, where a proof-of-principle demonstration of the quantum sensing technique has been the objective, we are primarily interested in the spectral behavior at frequencies away from the mechanical resonances since this is where the sideband-correlations of squeezed states play a role.

Conclusion and outlook 7

In the previous chapters we have investigated theoretically and experimentally the feasibility of exploiting squeezed states for increasing the transduction sensitivity of micromechanical motion in a cavity optomechanical system. It has been known for long that the application of squeezed states can improve the sensitivity of interferometric measurements by effectively reducing the shot noise level, but the principle has hitherto not been implemented in the context of micromechanical oscillators.

Through the conducted theoretical work we have shown that for systems pertaining to the non-sideband resolved regime the use of squeezed light only provides an increase in the achievable transduction signal-to-noise ratio for operation in the highly under-coupled or highly over-coupled regimes. Moreover, the technique does not provide an absolute improvement as the quantum-enhanced transduction signal is always below that achievable by a coherent state at critical coupling. The situation is different for systems operating in the sideband resolved regime where we find that squeezing-enhanced transduction always provides an absolute improvement.

We have successfully implemented the technique for the particular system of a tapered fiber coupled microtoroidal resonator at room temperature. Specifically, we observe that by probing the optomechanical system with a bright squeezed state the thermally excited micromechanical motion is transduced with a signal-to-noise ratio improved by 0.72 dB compared to a coherent probe of the same power. In the experiments, the achievable enhancement was predominantly limited by the optical loss associated with fiber coupling of the squeezed state and the evanescent coupling to the microtoroidal resonator.

The experimental work reported here constitutes the first demonstration of interfacing micromechanical systems with squeezed light. However, we anticipate that the application of quantum correlated states of light will become more and more frequent in the optomechanics community as the strive for higher and higher sensitivities continues. In particular, the improved sensitivity offered by employing squeezed probe states might become instrumental for finally attaining the standard quantum limit in an optomechanical systems. With the ability to cool micromechanical systems to their motional ground state, the application of more excotic quantum states might also open up for the possibility of preparing macroscopic superposition states of micromechanical oscillators. This would be a major scientific achievement, and potentially a way to study the elusive quantum-classical boundary. Another application of the technique which is currently being pursued

in our group is to exploit the quantum-enhanced signal-to-noise ratio for improved efficiency of electro-static feedback cooling of the mechanical vibrations. For this particular cooling technique the efficiency and thereby the lowest attainable mode temperature is directly related to the transduction signal-to-noise ratio.

Part III

Integrated source of single-mode quadrature squeezed light

Introduction 8

The first pioneering demonstrations of squeezed states of light were reported in 1985 by R. Slusher et al. [119] in the context of four-wave mixing in atomic vapors, and somewhat later by Shelby et al. [117] also by four-wave mixing, but in cooled single-mode optical fiber. The immense progress in control and manipulation of quantum states of light and matter and their mutual interaction, witnessed during the last decades, has by now facilitated generation of squeezed states of light in a broad selection of physical systems, with the most recent member of the family being ponderomotive squeezing through optomechanical interactions [25, 101, 109]. However, the most common sources are optical parametric amplifiers, based on spontaneous parametric down-conversion in $\chi^{(2)}$-materials, and the to date strongest suppression of quantum noise by 12.7 dB, demonstrated by T. Eberle et al. [39], was also achieved in such a system.

In the emergent field of optical quantum technologies, squeezed quantum states of light have become an essential resource for many continuous variable quantum information and communication protocols [89]. And the feasibility of exploiting such quantum-correlated states for ultra-sensitive measurements has been demonstrated in numerous implementations of quantum-enhanced sensing, pioneered in the context of Mech-Zehnder interferometry [28, 134], and by now applied both at macroscopic scale [127] and in microscopic systems as demonstrated in Part II of this thesis [59]. However, the size and operational complexity of quantum light sources remains a limitation for practical and industrial applications of optical quantum technologies and integration with electronics. Efficient pulsed Kerr-squeezing in standard polarization maintaining fibers [15, 53] requires fiber lengths on the order of tens of meters and in so-called monolithic squeezed light sources [77, 23, 39] the employed bulk nonlinear crystals are in themselves orders of magnitude larger than lithographically defined electronic integrated circuits. An important step towards source miniaturization is the recent demonstration of twin beam squeezing in resonant on-chip structures [38], bringing the development of fully integrated optoelectronic quantum sensing devices one step closer. But so far, an integrated source of quantum correlated continuous variable states remains to be demonstrated.

The development of integrated quantum light sources is faced by one major obstacle: optical loss. Whereas free-space sources mainly suffer from Fresnel losses at optical interfaces, which can be mitigated by tailored anti-reflection coatings, integrated waveguide circuits are also subject to material losses and scattering losses.

The former contribution is governed by intrinsic band structure properties of the material and cannot be compensated for. Bulk crystalline silicon has an indirect band gap of 1.1 eV leading to significant two-photon absorption (TPA) at wavelengths below roughly 2000 nm, and this is the reason why so much attention is currently drawn towards identification of CMOS-compatible alternatives to the otherwise appealing silicon-on-insulator (SOI) platform for nonlinear optics. Scattering losses, primarily originating from the roughness of the lithographically defined sidewalls and increasing quadratically with the refractive index contrast $\Delta n = n_{core} - n_{cladding}$ [32], can be compensated for by optimization of fabrication procedures and engineering of waveguide dimensions.

Yet another severe loss-related challenge for high-index contrast waveguides is the inevitable mode conversion and effective index step associated with chip interfacing. The former leads to loss through coupling to radiation modes and the latter to Fresnel loss and low collection efficiency because of the large numerical aperture of high-index contrast waveguides. The most common approach to overcome these complications is to employ inverse tapers (spot size converters) at the waveguide ends allowing near-adiabatic conversion between the tightly confined waveguide mode and that of a single mode tapered fiber or fiber pigtail. Using such coupling strategies approximately 1.5 dB/facet coupling loss has been reported for pigtailed high-index contrast Hydex waveguides [40].

In this part, we address the problem of scalability of available squeezed-light sources, by targeting the development of a novel integrated source of quadrature squeezed states based on SPM (cf. Section 1.2.3) mediated by the $\chi^{(3)}$-nonlinearity in resonant silicon nitride waveguide structures. Such systems have previously been proven viable sources of photon pairs with controllable degree of correlation [54], and they have formed the basis for demonstration of on-chip classical optical parametric oscillations [83] and frequency combs [96] at telecom wavelengths. But so far, the cv quantum noise properties of the parametrically generated sideband fields have remained unexplored experimentally. The aforementioned applications in general require careful engineering of the device dispersion properties in order to achieve a broad phase matching bandwidth spanning several free spectral ranges. But in the particular case discussed here, this condition is greatly relaxed since the quantum correlated fields of interest are constituted by symmetrically distributed rf-sidebands of the pump, co-resonant on the same cavity mode, rather than distinctly colored signal and idler modes. On the other hand, this causes considerable technical complications at the state interrogation stage because the bright pump carrier prevents direct characterization of the sideband state by balanced homodyne tomography. Either the sidebands must somehow be separated from the carrier or the state tomography should be implemented by other means.

The contents of this Part is structured as follows: In Chapter 9 we present the basic considerations underlying this development project and motivate the particular choice of host material. Next, in Chapter 10 we develop a full quantum-dynamics model for analyzing squeezed-light generation in the considered system, and in the following Chapter 11 we summarize extensive work performed on identification of a

feasible device design through numerical simulations of optical and nonlinear properties. Combining the simulation results with the theoretical model we derive a set of promising estimates for the device performance. Turning to the experimental aspects of the project, we present in Chapter 12 details on the actual integrated devices that have been fabricated, and we finally discuss the experimental work conducted on the devices so far, covering optical characterization and attempted squeezed-light generation. Particular attention is paid to the exploration of different detection strategies for overcoming the difficulties in characterizing quantum noise properties of bright states.

The material presented in Chapters 9, 10, and 11 is based on the conducted theoretical feasibility study discussed in the submitted manuscript:

- U. B. Hoff, B. M. Nielsen, and U. L. Andersen. An integrated source of broadband quadrature squeezed light. *arXiv:quant-ph/1504.01054. Submitted to Optics Express, March 2015*

Basic considerations 9

Before turning to in-depth discussions of the various aspects of the project we will first set the stage by motivating some of the directions followed during the work, such as the choice of silicon nitride as host material for squeezed-light generation and the target device design. We also provide a preliminary discussion of squeezing via third-order optical nonlinearity, with the intention of giving the unfamiliar reader an intuitive understanding of the process.

9.1 Why silicon nitride?

Integration of quantum optical processes requires the host material to possess both a strong nonlinearity, essential for implementing high-efficiency parametric interactions, and low material and structural loss in order to preserve the generally fragile quantum states. These requirements are met by low-pressure chemical vapor deposition (LPCVD) amorphous stoichiometric silicon nitride (Si_3N_4). With a linear refractive index of $n \approx 2$ and a reasonably high third order Kerr nonlinearity of $n_2 = 2.5 \times 10^{-15}\text{cm}^2/\text{W}$ [61], it is a suitable core material for high-index contrast waveguides in applications where tight field confinement and small waveguide bending radii are required. For comparison, the nonlinearity of silicon nitride is roughly 10 times the nonlinearity of silica, 2 times that of Hydex, and 0.1 times that of silicon. On the loss side, 200 nm thick channel waveguides with ≤ 0.2 dB/cm propagation loss at 780 nm have been demonstrated [32]. Using temperature-cycling to overcome the tensile-stress limited film thickness of around 250 nm [33, 86], propagation losses of 0.12 dB/cm at 1540 nm have been measured in channel waveguides of more than 700 nm thickness [48]. And by employing a large-aspect ratio waveguide geometry the dominating scattering loss contribution can be shifted from the sidewalls to the waveguide top and bottom surfaces, which for LPCVD Si_3N_4 have roughnesses in the sub-nanometer regime, resulting in ultra-low waveguide propagation losses below 0.1 dB/m at 1580 nm [14]. Unfortunately, this comes at the price of low field confinement, which is essential for efficient nonlinear processes. Furthermore, the band gap of silicon nitride is approximately 5 eV [46], placing the absorption edge just below 300 nm. This provides low material loss in the visible and infrared, and negligible TPA above 600 nm even at high power levels, as opposed to silicon. Thus motivated, the device will be designed for an operation

wavelength around 850 nm, conveniently centered in the Ti:sapphire tuning range and with readily available low-loss optics and high quantum efficiency photodiodes.

9.2 Integrated resonator

The specific integrated system that we wish to explore in this project is a buried channel waveguide circuit consisting of a racetrack resonator (RTR) with radius of curvature R, laterally coupled to a straight bus waveguide, as illustrated in Fig. 9.1 (a). Similar to the microtoroidal resonators discussed in Part II, coupling to

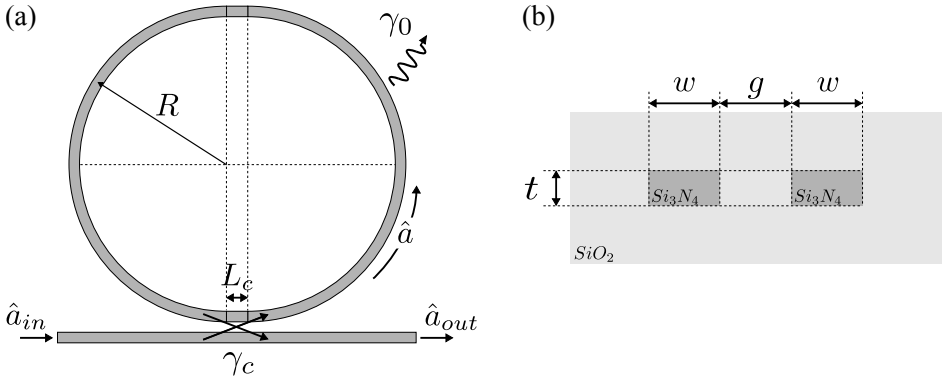

Figure 9.1: (a) Top view of the racetrack resonator geometry. (b) Cross sectional view at the bus-resonator coupling region. The thickness is $t = 250\,\text{nm}$ and the width w is chosen such that the waveguide only supports a single transversal mode. The gap size g is fixed, and limited from below by the resolution of the lithographic method chosen, and the coupling rate γ_c is determined by the length of the coupling region L_c. Figure adapted from [58].

the RTR is achieved by a finite overlap of the evanescent fields of the two waveguide modes in the coupling region, and the efficiency is modelled by the field amplitude coupling rate[1] $\gamma_c \approx \kappa_c^2/2\tau$, where $\tau = 2n_{eff}(L_c + \pi R)/c$ is the resonator round-trip time. The coupling rate is controlled through the gap size and coupling length parameters g and L_c, respectively. Intracavity losses, primarily due to scattering from the waveguide sidewalls, are represented by an intrinsic loss rate $\gamma_0 \approx \kappa_0^2/2\tau = \alpha c/2n_{eff}$, where α is the waveguide per meter loss parameter, c is the vacuum speed of light, and n_{eff} the effective mode index. The total loss rate is given by $\gamma = \gamma_0 + \gamma_c$ (HWHM) determining the loaded quality factor of the resonator. An important parameter for controlling the squeezed light generation efficiency of the system is the *escape efficiency* $\eta_{esc} = \gamma_c/\gamma$, characterizing the collection efficiency

[1] The integrated resonator can be modelled by an equivalent one-sided bulk-optics cavity with internal loss, for which κ_c^2 is the intensity transmittivity of the coupling mirror. The approximate expression is valid for $\kappa_c^2 \ll 1$.

of the intracavity field[2]. For the application of squeezed light generation, operation in the over-coupled regime ($\eta_{esc} > 1/2$) is required. But since coupling inevitably reduces the quality factor, obviously a suitable trade-off between efficient collection from the cavity (large η_{esc}) and resonant enhancement of the nonlinear process (small γ) has to be identified.

As depicted in Fig. 9.1(b), we opt for a rectangular low-aspect ratio cross sectional geometry of the waveguides. For the sake of minimizing fabricational complexity, we restrict the thickness t to a value of 250 nm, yielding the largest possible mode confinement while at the same time eliminating the need for stress-releasing temperature cycling in the deposition process. This in turn puts an upper bound on the width w, due to the requirement of single mode operation.

9.3 Squeezing via the $\chi^{(3)}$ Kerr nonlinearity

A simple and intuitive understanding of the generation of bright quadrature squeezed states by SPM is provided in [10]: Consider an input pump field $\alpha = \alpha_0 + \delta X_1^{in} + \delta X_2^{in}$ consisting of a coherent carrier amplitude and vacuum fluctuations in the sideband quadratures. Both the coherent amplitude α_0 and the noise δX_1^{in} drives the intensity dependent SPM process, resulting in a phase shift of the carrier proportional to α_0 and induced phase fluctuations at sideband frequencies given by $\delta\phi_{nl} = 4\pi n_2 L \alpha_0 \delta X_1^{in}/\lambda$. For small angles the corresponding change in the phase quadrature fluctuations is $\Delta(\delta X_2) \approx \alpha_0 \delta\phi_{nl} \equiv 2r\delta X_1^{in}$, yielding the following input-output relations for the quadrature fluctuations under influence of SPM:

$$\delta X_1^{out} = \delta X_1^{in}, \tag{9.1}$$

$$\delta X_2^{out} = \delta X_2^{in} + 2r\delta X_1^{in}. \tag{9.2}$$

While the amplitude quadrature is unaffected by the interaction, the phase quadrature is admixed an amount proportional to the amplitude fluctuations and the carrier intensity, correlating the two quadratures. The correlations are strongest at a quadrature phase of $\theta_{\min}(r) = \frac{1}{2}\arctan(-1/r)$ for which the variance is $\mathrm{Var}(\delta X_{\theta_{\min}}^{\mathrm{out}}) = 1 - 2r\sqrt{1+r^2} + 2r^2$. Thus, for any $r > 0$ the noise is, in principle, squeezed below the vacuum level at the optimal phase angle which in the limit of weak interaction strength is $\lim_{r\to 0}\theta_{\min}(r) = -\pi/4$. The SPM squeezing process is illustrated in Fig. 9.2. Due to the intensity-dependence of the process, the state is progressively rotated in phase space for increasing squeezing strengths, and at the same time the squeezing angle θ_{min} approaches the amplitude quadrature of the driving field. In the limit of strong squeezing, theory predicts a crescent shape deformation of the noise ellipse. This limit is, however, far beyond the experimentally realizable – as pointed out by Sizmann and Leuchs [118], entering this regime requires a sufficiently strong nonlinearity that even a few-photon driving field would be enough to generate significant squeezing.

[2]The escape efficiency is identical to the coupling parameter η_c introduced in Section 4.3, and the different names just reflect common terminology used in the different contexts.

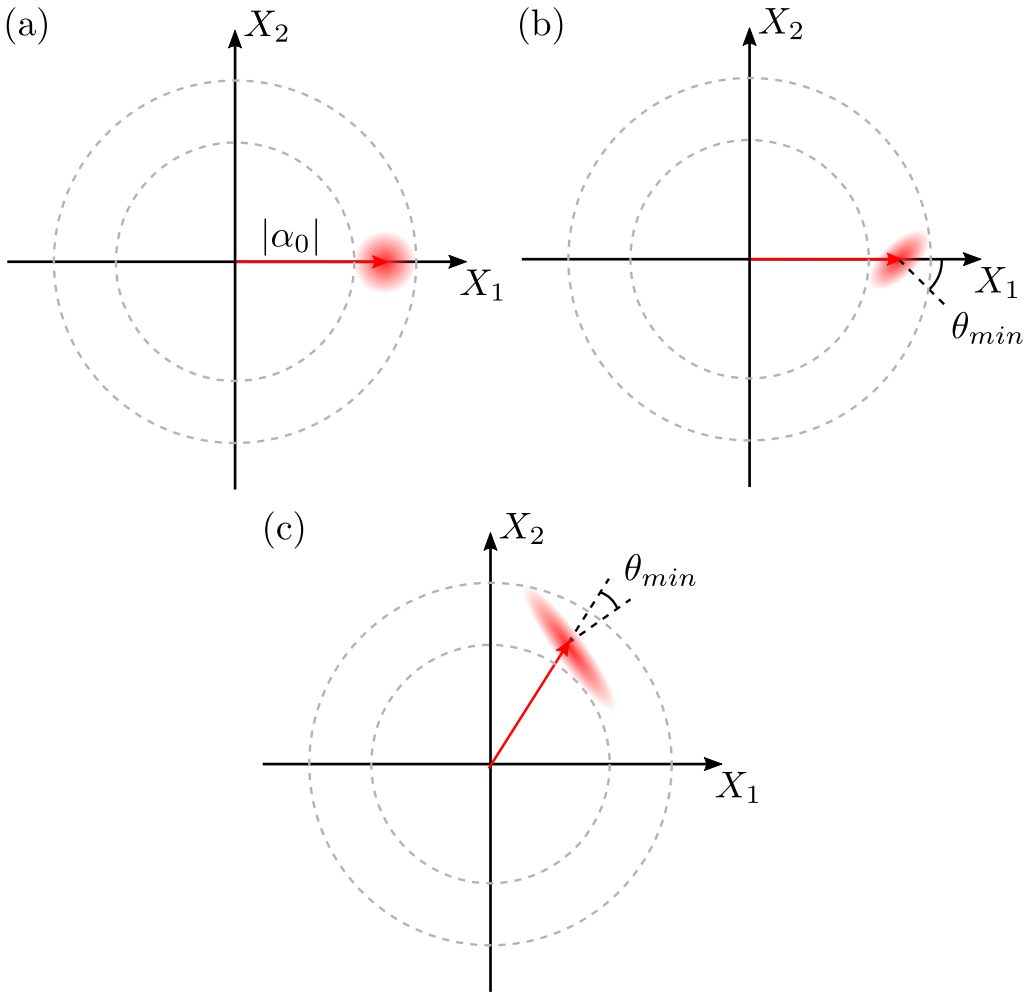

Figure 9.2: Phase space illustration of SPM squeezing. The amplitude quadrature fluctuations are unaffected by the interaction, cf. (9.1), and the resulting output state is given by a transformation of the input comprised of a carrier-phase rotation of the amplitude about the origin and a shearing of the fluctuations, orthogonal to the amplitude. As a result, the output state is bounded by the dashed circles representing the input state amplitude fluctuations. (a) input coherent state. (b) Weak squeezing resulting in minimum uncertainty at $\theta_{min} = -\pi/4$ relative to the drive field. (c) The stronger the interaction, the more the squeezing angle approaches the amplitude quadrature of the driving field.

Quantum-model of SPM squeezing 10

Though providing an intuitive understanding of how squeezing can be generated via SPM through coupling of amplitude and phase quadrature fluctuations by the intensity dependent refractive index, the simplistic description presented in the previous chapter only captures part of the dynamics of the system we are concerned with. In this chapter, we present a full quantum analysis of the effects of SPM on the dynamics and noise properties of a cavity field interacting with a Kerr nonlinearity. We will do so by taking the particular SPM Hamiltonian as onset for derivation of the quantum Langevin equations governing the intracavity field dynamics. As we will see, the presence of a Kerr medium in the cavity can significantly alter the cavity response. Not only does it enable manipulation of the optical quantum noise properties and generation of squeezed states, on a classical level it can also lead to optical bistability of the intracavity field in certain pumping and detuning regimes. The primary purpose of the analysis is to derive an analytical expression for the quadrature noise spectrum of the output field which will form the basis for a subsequent estimation of the device performance.

10.1 Interaction Hamiltonian

As already mentioned in Section 1.2.3, the third order Kerr nonlinearity supports a number of processes, and for a derivation of the full corresponding interaction Hamiltonian we refer the reader to the appendix of [58]. However, for the present analysis we will only be concerned with the part describing the fully degenerate SPM sub-process. Quantum mechanically, this process is governed by a quartic Hamiltonian of the form

$$\hat{H}_{SPM} = \frac{\hbar\xi}{2}\hat{a}_p^{\dagger\,2}\hat{a}_p^2, \tag{10.1}$$

where the interaction strength is given by

$$\xi = \frac{\hbar\omega_p c^2\gamma_{nl}}{2n_{eff}^2 L}. \tag{10.2}$$

Here, L is the round-trip length of the resonator and n_{eff} is the effective mode index of the pumped guided mode with resonance frequency ω_p.

10.2 Quantum dynamics

In close analogy to the analysis in Section 4.3, we follow the standard quantum Langevin equation approach [31, 43] for analyzing the noise properties of the cavity output field. Using the Fourier space solution to the dynamical equations, we derive the single mode squeezing spectrum for the output field.

10.2.1 Langevin equation of motion

Considering a single pumped resonator mode $\hat{a}_p$ interacting with a Kerr nonlinearity the general Langevin equation of motion is given by

$$\frac{d\hat{a}_p}{dt} = -\frac{i}{\hbar}\left[\hat{a}_p, \hat{H}\right] - \gamma\hat{a}_p + \sqrt{2\gamma_c}\hat{a}_{p,in}e^{-i\omega_L t} + \sqrt{2\gamma_0}\hat{b}_p, \tag{10.3}$$

where

$$\hat{H} = \hbar\omega_p\hat{a}_p^\dagger\hat{a}_p + \hat{H}_{SPM}. \tag{10.4}$$

Operators $\hat{a}_{p,in}$ and $\hat{b}_p$ represent driving and input vacuum fields, respectively. Transforming all mode operators to a frame rotating at the driving laser frequency ω_L, by means of the substitution $\hat{a}_p \rightarrow e^{-i\omega_L t}\hat{a}_p$ (cf. Appendix A), leads to the rotating frame equation of motion:

$$\frac{d\hat{a}_p}{dt} = -(\gamma - i\Delta_p)\hat{a}_p - i\xi\hat{a}_p^\dagger\hat{a}_p^2 + \sqrt{2\gamma_c}\hat{a}_{p,in} + \sqrt{2\gamma_0}\hat{b}_p, \tag{10.5}$$

with detuning $\Delta_p = \omega_L - \omega_p$ relative to the empty cavity mode frequency. Adopting the standard coupled-mode theory normalization convention, the steady-state value $|\alpha_p|^2$ represents the total photon number stored in the resonator mode and $|\alpha_{p,in}|^2$ the incoming traveling mode photon flux in the bus waveguide.

10.2.2 Linearized dynamics

In order to solve the system dynamics we linearize the rotating frame quantum Langevin equation (10.5) about the solution α_p to the steady-state equation

$$|\alpha_p|^2(\gamma^2 + (\Delta_p - \xi|\alpha_p|^2)^2) = 2\gamma_c|\alpha_{p,in}|^2. \tag{10.6}$$

We do so by making the substitution $\hat{a}_p \rightarrow \alpha_p + \delta\hat{a}_p$ and retaining only terms of first order in the quantum fluctuation operator $\delta\hat{a}_p$. Defining vectors of fluctuation operators, e.g. $\boldsymbol{\delta a}_i = (\delta\hat{a}_i,\, \delta\hat{a}_i^\dagger)^T$, the linearized system of differential equations can be stated as a matrix equation

$$\frac{d\boldsymbol{\delta a}_p}{dt} = \left[\mathbf{M} - \gamma\mathbf{I}_2\right]\boldsymbol{\delta a}_p + \sqrt{2\gamma_c}\boldsymbol{\delta a}_{in} + \sqrt{2\gamma_0}\boldsymbol{\delta b}, \tag{10.7}$$

where $\mathbf{I}_2$ is the two-dimensional identity matrix. The dynamics of the pumped mode is fully characterized by the system matrix

$$\mathbf{M} - \gamma\mathbf{I}_2 = \begin{pmatrix} -\gamma - i(2|\epsilon| - \Delta_p) & -i\epsilon \\ i\epsilon^* & -\gamma + i(2|\epsilon| - \Delta_p) \end{pmatrix} \tag{10.8}$$

and its eigenvalues

$$\lambda_\pm = -\gamma \pm \sqrt{|\epsilon|^2 - (\Delta_p - 2|\epsilon|)^2}. \tag{10.9}$$

For brevity we have introduced the pump parameter $\epsilon = \xi|\alpha_p|^2 e^{i2\phi}$, where ϕ is the phase of the pump field. From (10.8) we observe that SPM induces phase-dependent correlations in the fluctuations of the intracavity field (anti-diagonal elements), increasing with pump power, and a power-dependent nonlinear shift of the cold-cavity resonances (diagonal elements), responsible for optical bistability [37, 105] of the system.

Stability of the pumped mode requires that $\mathrm{Re}(\lambda) < 0$ for all eigenvalues [63]. This is trivially fulfilled for λ_-, and for λ_+ the condition can be equivalently formulated as: $3|\epsilon|^2 - 4\Delta_p|\epsilon| + \Delta_p^2 + \gamma^2 > 0$. The real part of λ_+ is plotted in Fig. 10.1. Solving the equation for $|\epsilon|$ we find solutions $|\epsilon|_\pm = \frac{1}{3}(2\Delta_p \pm \sqrt{\Delta_p^2 - 3\gamma^2})$; for $|\epsilon|_- \leq |\epsilon| \leq |\epsilon|_+$ the system is unstable and outside it is always stable. Furthermore, for $\Delta_p < \sqrt{3}\gamma$ no real positive solution for $|\epsilon|$ exists and the stability criterion is always fulfilled; for $\Delta_p > \sqrt{3}\gamma$ two solutions exist, marking the onset of optical bistability. We observe from (10.9) that for the particular choice of detuning $\Delta_p = \xi|\alpha_p|^2 = |\epsilon|$ the eigenvalues collapse to a degenerate pair $\lambda_\pm = -\gamma$. Thus, the system is always stable, independent of the pump power. In this case the SPM induced nonlinear shift of the cavity resonances is exactly compensated for by the pump laser detuning, restoring the usual proportionality between input pump power and stored intracavity energy, $|\alpha_p|^2 = 2\gamma_c/\gamma^2 \cdot |\alpha_{p,in}|^2$ for a resonantly driven cavity.

10.3 Squeezing spectrum

In order to derive the fluctuation spectrum which is the important quantity for characterizing the noise properties of the field, we transform (10.7) into frequency space. Fourier transformation conveniently turns the differential equation system into a set of algebraic equations for the intracavity fluctuations, and the solution is readily found to be

$$\boldsymbol{\delta a}_p(\Omega) = -\left[\mathbf{M} - (\gamma - i\Omega)\mathbf{I}_2\right]^{-1} \left(\sqrt{2\gamma_c}\boldsymbol{\delta a}_{in}(\Omega) + \sqrt{2\gamma_0}\boldsymbol{\delta b}(\Omega)\right). \tag{10.10}$$

The intracavity field fluctuations can in turn be projected onto the output mode through the boundary condition,

$$\boldsymbol{\delta a}_{out}(\Omega) = \boldsymbol{\delta a}_{in}(\Omega) - \sqrt{2\gamma_c}\boldsymbol{\delta a}_p(\Omega). \tag{10.11}$$

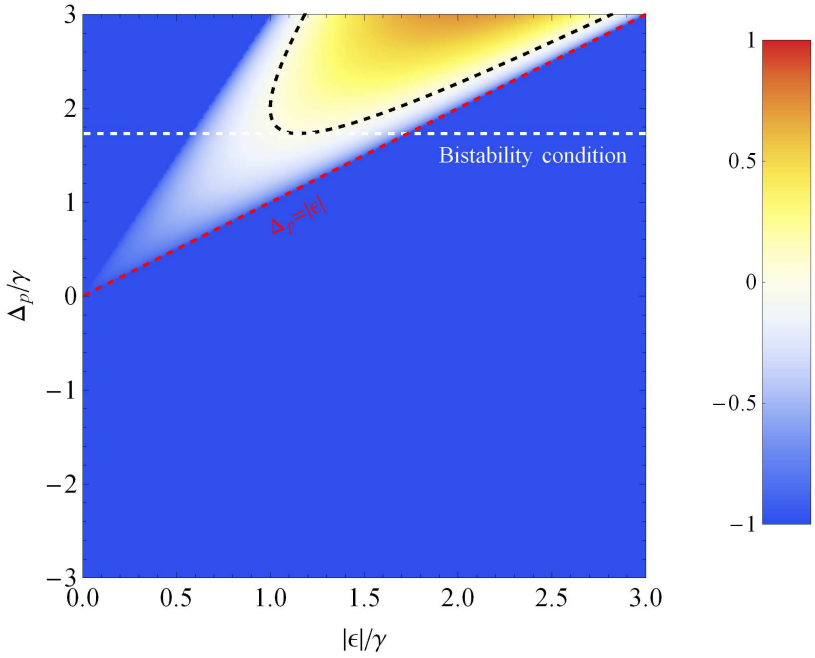

Figure 10.1: Real part of the pumped mode eigenvalue λ_+ as a function of pump parameter and detuning. The $\lambda_+ = 0$ contour (black dashed line) divides the parameter space into a stable ($\lambda_+ < 0$) and an unstable ($\lambda_+ > 0$) region. For detunings above the bistability condition (white dashed line) two stable regions exist and the system can be tuned between the two by changing the intracavity power. The intermediate unstable region is not accessible. By progressively detuning the drive field from the empty cavity resonance as the pump power is increased it is possible to maintain stability of the system and maximize the intracavity power (red dashed line). Furthermore, we observe that in terms of power the instability region is bounded from below by the condition that $|\varepsilon| > \gamma$ indicating that the nonlinear scattering rate from the pumped mode should exceed the cavity dissipation rate in order for instability to occur. Figure adapted from [58].

Inserting (10.10) into (10.11) we find for the output field fluctuations,

$$\begin{aligned}\boldsymbol{\delta a}_{out}(\Omega) &= [\mathbf{M}-(\gamma-i\Omega)\mathbf{I}_2]^{-1} \\ &\quad\times\Big(\left[\mathbf{M}+(\gamma_c-\gamma_0+i\Omega)\mathbf{I}_2\right]\boldsymbol{\delta a}_{in}(\Omega)+2\sqrt{\gamma_0\gamma_c}\boldsymbol{\delta b}(\Omega)\Big). \quad (10.12)\end{aligned}$$

Experimentally, the cavity output will be characterized by balanced homodyne detection of the field fluctuation quadratures

$$\delta\hat{X}_\theta(\Omega)=\delta\hat{a}_{out}(\Omega)e^{-i\theta}+\delta\hat{a}^\dagger_{out}(-\Omega)e^{i\theta}, \quad (10.13)$$

for which the quantum noise properties are fully characterized by the normal ordered second order moment

$$\begin{aligned}\langle:\delta\hat{X}_\theta(\Omega)\delta\hat{X}_\theta(\Omega'):\rangle &= \Big[e^{-2i\theta}\langle\delta\hat{a}_{out}(\Omega)\delta\hat{a}_{out}(\Omega')\rangle+e^{2i\theta}\langle\delta\hat{a}^\dagger_{out}(-\Omega)\delta\hat{a}^\dagger_{out}(-\Omega')\rangle \\ &\quad+\langle\delta\hat{a}^\dagger_{out}(-\Omega)\delta\hat{a}_{out}(\Omega')\rangle\Big]\delta(\Omega+\Omega'). \quad (10.14)\end{aligned}$$

The normal ordered spectrum of $\delta\hat{X}_\theta(\Omega)$ is given by the integral of (10.14) over Ω' [131]

$$:S_\theta(\Omega):=\int d\Omega'\langle:\delta\hat{X}_\theta(\Omega)\delta\hat{X}_\theta(\Omega'):\rangle, \quad (10.15)$$

and finally the squeezing spectrum of the output field quadrature is given by

$$S_\theta(\Omega)=1+:S_\theta(\Omega): \quad (10.16)$$

which can be directly measured as the power spectral density of the homodyne photocurrent. The additional constant term accounts for the vacuum variance contribution from anti-normal ordered terms of the second order moment, which for the particular field quadrature definition in (10.13) is equal to one.

Using the system matrix (10.8) the contributing second order moments in (10.14) can be evaluated, and through a bit of algebraic manipulation we can derive the following expression for the output squeezing spectrum of the pump (see Appendix B for a fully detailed derivation):

$$\begin{aligned}S^{SPM}_\theta(\Omega) &= 1+:S^{SPM}_\theta(\Omega): \\ &= 1+G\cdot\Big[2\gamma|\epsilon|-2\gamma\Big[2|\epsilon|-\Delta_p\Big]\cos 2(\theta-\phi) \\ &\quad-\Big[\gamma^2+\Omega^2-\Delta_p^2+4\Delta_p|\epsilon|-3|\epsilon|^2\Big]\sin 2(\theta-\phi)\Big] \quad (10.17)\end{aligned}$$

where

$$G=\frac{4\gamma_c|\epsilon|}{\Big[\Delta_p^2+\gamma^2-\Omega^2-4\Delta_p|\epsilon|+3|\epsilon|^2\Big]^2+4\gamma^2\Omega^2}. \quad (10.18)$$

Using the beamsplitter loss model described in Section 2.2.1, we can account for finite detection efficiency, primarily resulting from fiber-chip coupling (η_c), imperfect

mode overlap on the homodyne detector (η_{mm}), and photodiode quantum efficiency (η_{qe}). The resulting reduced measurable squeezing spectrum is given by

$$S_\theta^{meas}(\Omega) = (1-\eta) + \eta\, S_\theta(\Omega) = 1 + \eta\, :S_\theta(\Omega):, \tag{10.19}$$

where $\eta = \eta_c \cdot \eta_{mm} \cdot \eta_{qe}$ is the total detection efficiency.

Numerical investigation 11

Developing a novel squeezed-light source inevitably entails careful consideration of all parts of the design, in order for the system to meet the strict performance requirements, prerequisite for manipulating light at the quantum level. High source efficiency is generally desired, both in terms of required pump power and attainable quantum noise suppression, placing strong demands on the design in terms of nonlinear interaction strength and optical loss, respectively. And if in addition particular source characteristics are targeted, which is usually the case, e.g. small footprint, operation wavelength(s), resonant enhancement or not, broad/narrow bandwidth, etc., then further requirements obviously apply.

Whereas bulk optics systems to a certain degree allow tweaking and post optimization in case of sub-optimal performance or parasitic effects, integrated devices are less forgiving as the structures are hard coded into the host material, requiring a new fabrication run to accommodate modifications. On the other hand, the compactness and ability of batch production of integrated devices allows multiple parameter ranges to be explored in a single fabrication run with no or only limited additional cost. However, in either case it is important to identify the relevant tuning range or tolerance of central design parameters within which optimal system operation is expected.

As presented in Section 11.1 below, we have addressed this point by undertaking a thorough numerical investigation of crucial optical propagation and nonlinear properties of the envisioned waveguide racetrack resonator. Table 11.1 summarizes the parameters that were held fixed throughout the simulations, and we furthermore constrained the minimum lateral feature size to 400 nm to make the design compatible with standard UV stepper lithography. On the basis of our findings we have identified a target device design, and the feasibility of it has subsequently been evaluated by using the simulation results as input to the theoretical model developed in Chapter 10. These results are discussed in Section 11.2.

11.1 Device design via numerical simulation of optical properties

As described in Section 1.2.2, determination of the supported modes of a waveguide structure can be reduced to solving a two-dimensional eigenvalue problem on the

Parameter	Symbol	Value
Operation wavelength	λ	850 nm
Waveguide thickness	t	250 nm
Refractive index of silicon dioxide @ 850 nm	n_{SiO_2}, n_{clad}	1.45
Refractive index of silicon nitride @ 850 nm	$n_{Si_3N_4}$, n_{core}	2.00

Table 11.1: Parameter values held fixed in simulations.

transverse cross section. Though providing a considerable simplification compared to solving the full 3D vectorial Helmholtz equation it is still, in general, a difficult problem for which one has to resort to numerics. A number of different methods exist for numerically solving the eigenmode problem for arbitrary waveguide designs, e.g. the finite element method (FEM) and the finite difference method (FD), where in the latter case the frequency domain formulation (FDFD) is particularly well-suited for mode solving. Both methods rely on breaking up the continuous analytical problem on a fine-meshed discretization grid and in both cases the accuracy of the solution depends on the grid finesse, resulting in exceedingly long computation times when finer and finer details need to be resolved. In the early stage of this project both methods were explored; FEM via the commercial software COMSOL, and FDFD using a self-implemented solver. However, for the work presented in the following, we have exclusively used the full vectorial mode solver software *FieldDesigner*, commercially available from PhoeniX Software, which employs the Film Mode Matching (FMM) method [123] for mode solving. Unlike FEM and FD, FMM is a semi-analytic method not requiring discretization. Rather it slices the structure up into thin films and finds the TE and TM of each film. The total mode is then constructed by matching up the field distributions of each individual film mode. Due to its working principle, FMM is particularly well-suited for analysis of rectangular dielectric waveguides.

11.1.1 Supported modes

A very basic requirement that has to be imposed is that the waveguides be single mode. That is, the transversal waveguide geometry should be designed in such a way that only a single guided mode is supported. This is important in order to optimize power confinement in the core and to facilitate mode matching of the output field to a free space local oscillator field as required for homodyne interrogation.

In the weak-guidance approximation, where the relative index difference $\Delta = (n_{core}^2 - n_{clad}^2)/(2n_{core}^2)$ is small, $\Delta \ll 1$, an analog of the V-number or *normalized frequency* for optical fibers [111], can be defined for waveguides [78]:

$$V = \frac{2\pi}{\lambda}\rho n_{core}\sqrt{2\Delta}, \tag{11.1}$$

and the condition $V = 2.131$ then provides an approximate single-mode criteria [78]. The characteristic dimension is defined as $\rho = \sqrt{\rho_x \rho_y}$ where $\rho_x = w/2$ and $\rho_y = t/2$

are the half widths of the waveguide. Using (11.1) and the fixed value for t we find that the cut-off for the first higher-order TE[1] mode appears at $w_{\mathrm{co}} = 700\,\mathrm{nm}$. However, since the waveguides considered here have a rather large index difference ($\Delta = 0.237$) the weak-guidance approximation is not entirely justified, and we should not have too much faith in the predicted cut-off value. In Fig. 11.1 we plot the numerically calculated effective mode indices for the first three guided modes as function of waveguide width w. Starting from the square cross section and increasing the $w:t$ aspect ratio the effective indices of the fundamental TE and TM modes separate with $n_{eff}^{TE} > n_{eff}^{TM}$, indicating that the horizontally polarized TE mode is more confined to the silicon nitride core. This geometry-induced birefringence improves the polarization maintaining property of the waveguide and it is thus beneficial to maximize the aspect ratio. As the width is further increased the first higher-order TE mode starts to break through with the single-mode cutoff width being $w_{\mathrm{co}} \simeq 600\,\mathrm{nm}$. The large discrepancy between this and the first predicted value highlights the need for numerical analysis in order to make reliable predictions.

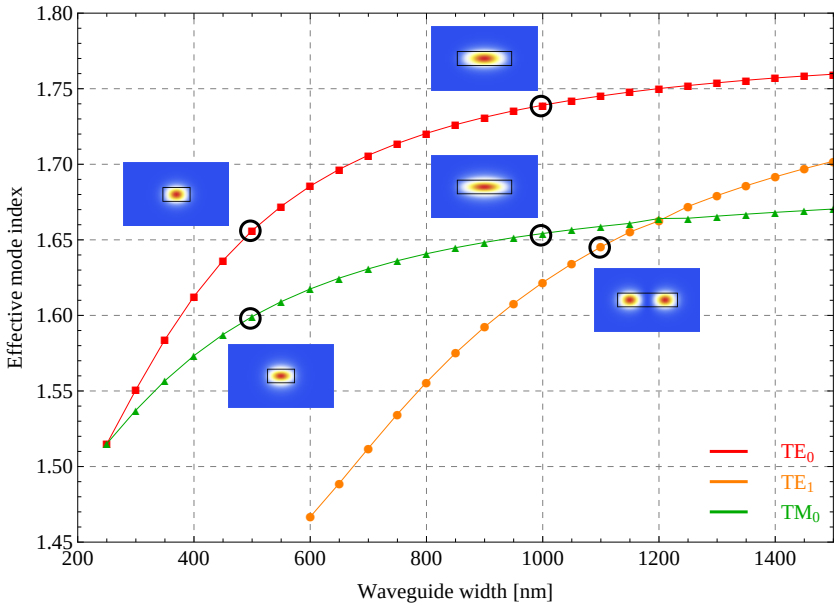

Figure 11.1: Simulated ($\lambda = 850\,\mathrm{nm}$, t $= 250\,\mathrm{nm}$) effective mode indices for the first three guided modes as function of waveguide width. Insets: Simulated mode profiles corresponding to each of the five encircled points. Solid black lines outline the waveguide core cross section. Figure adapted from [58].

[1]Strictly speaking the field inside a rectangular buried channel waveguide is neither purely TE or TM, since the two-dimensional confinement generally yields a skew in the mode. But so-called quasi-TE and quasi-TM modes exist, for which the dominant part of the electric field is along the x- or y-axis, respectively. That said, we will however simply refer to these modes as TE or TM throughout the rest of this thesis.

11.1.2 Optimizing the nonlinear interaction strength

An equally important property related to the waveguide cross section is the effective mode area A_{eff} introduced in Section 1.2.3. Since the Hamiltonian coupling constant (10.2) is inversely proportional to A_{eff}, minimization of this parameter will have a direct impact on the device efficiency. Different definitions of A_{eff} exist in the litterature, but here we adopt the form introduced by Rukhlenko et al. [106] given by

$$A_{eff} = a_{NL} \iint_{-\infty}^{\infty} S_z dxdy \Big/ \iint_{NL} S_z dxdy \,, \tag{11.2}$$

where a_{NL} is the cross sectional area of the nonlinear waveguide core and S_z is the time-averaged z component of the Poynting vector[2]. The effective mode area is thus simply defined as the core area scaled by the ratio of total mode power to power transmitted through the core. Simulated effective TE_0 mode areas as function of waveguide width are shown in Fig. 11.2 for a range of different thicknesses.

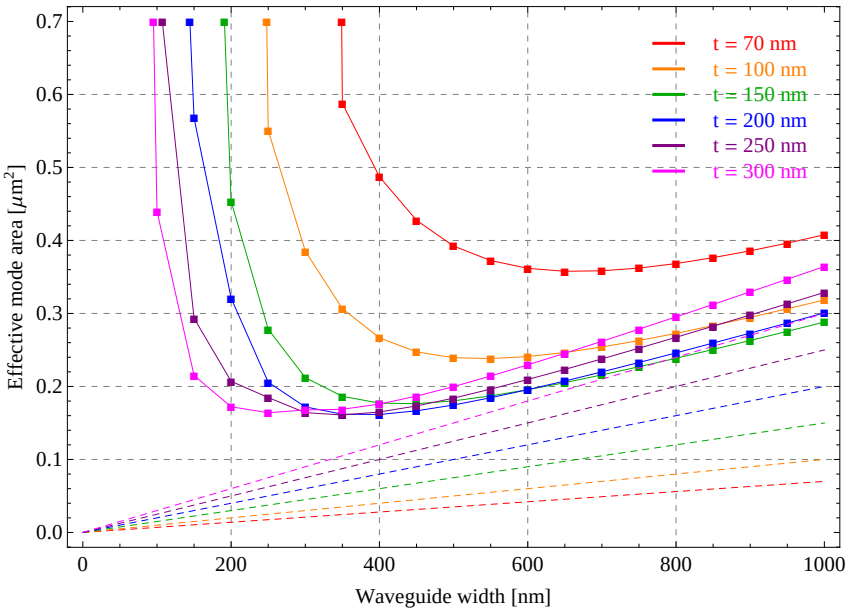

Figure 11.2: Simulated ($\lambda = 850\,\text{nm}$) effective mode area as function of waveguide width for different waveguide thicknesses. Dashed lines show the nonlinear core area a_{NL} which, according to the definition in (11.2), is the minimal effective mode area for a given cross section. Figure adapted from [58].

According to the simulated effective indices in Fig. 11.1 the waveguide width should be kept below 600 nm to maintain single mode operation. But to benefit from the geometry-induced polarization maintaining property the ratio of width to thickness should be maximized. On the other hand the simulated effective mode

[2]The z-axis is defined to be along the propagation direction of the bus waveguide.

areas in Fig. 11.2 point in the direction of a reduced $w : t$ aspect ratio for increasing the nonlinear interaction strength. From this we anticipate that a cross sectional waveguide geometry with $t = 250\,\text{nm}$ and $w = 500\,\text{nm}$ would be a suitable compromise, and the following simulations will assume these values.

11.1.3 RTR coupling

Having identified a suitable cross sectional design we now turn to a discussion of how the RTR coupling efficiency can be tailored to meet the requirements for squeezed light generation. Most importantly, the escape efficiency $\eta_{esc} = \gamma_c/\gamma$ of the resonator is required to be large, as otherwise the squeezed intracavity field will predominantly decay via internal loss sources rather than being collected through the bus. Meeting this requirement means that the coupling efficiency should overcompensate the resonator round-trip loss due to linear propagation loss and bending loss. But on the other hand we also want to preserve a certain field enhancement factor of the resonator in order to boost the nonlinear interaction.

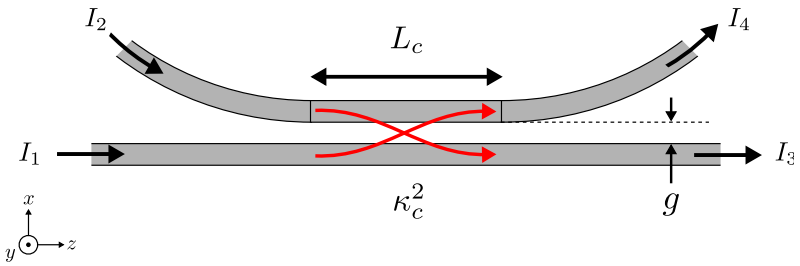

Figure 11.3: Directional coupler formed at the RTR-bus waveguide "junction". The couping efficiency κ_c^2 is controllable through the bus-to-RTR separation g and length of the coupling region L_c.

Physically, coupling to the RTR is achieved by means of a four-port directional coupler-like waveguide architecture (Fig. 11.3) formed by placing the bus waveguide in the vicinity of the RTR. If the separation is sufficiently small then the overlap of the two waveguide mode functions $\int_{core\,2} u_1(x,y)u_2(x,y)dA$, integrated over the second core, will take a nonvanishing value, enabling transfer of power from mode 1 to mode 2.[3] The directional coupler is the integrated analogue of a free-space beamsplitter and its classical action is, in terms of the coupled mode intensities,

[3]From a quantum mechanical perspective, the individual modes of the bus and RTR waveguides can be seen as eigenstates of the trapping potential formed by the respective dielectric structures. The corresponding wavefunctions have exponentially decaying tails outside the potential wells and if the structures are sufficiently close that the tails overlap significantly then tunneling between the wells becomes possible.

described in a way similar to the beamsplitter transformation in Section 2.2.1:

$$\begin{pmatrix} I_3 \\ I_4 \end{pmatrix} = (1-\Gamma_l) \begin{pmatrix} 1-\kappa_c^2 & \kappa_c^2 \\ \kappa_c^2 & 1-\kappa_c^2 \end{pmatrix} \begin{pmatrix} I_1 \\ I_2 \end{pmatrix}, \tag{11.3}$$

where κ_c^2 is the power coupling efficiency and Γ_l is a power loss coefficient, relevant since the directional coupler does not necessarily provide adiabatic transfer between the coupled modes. The total coupling efficiency κ_c^2 is given by the integral over the entire resonant interaction between the bus and RTR waveguide modes along the z-direction, with a predominant contribution from the coupling region of length L_c. Accounting for the spatial variation of the coupling strength, dependent on the instantaneous waveguide separation $g(z)$, the total field coupling efficiency is given by [84]

$$\kappa_c = \int_{-\infty}^{\infty} \kappa_c(g(z)) e^{i(\beta_1-\beta_2)z} dz, \tag{11.4}$$

where $\beta_{1,2}$ are the propagation constants of the individual modes. If the bus is initially excited (port 1), then after an interaction length L_0, which depends on the actual coupler architecture and the optical wavelength, the optical intensity will be transferred to the RTR waveguide (port 4). In general, the intensity splitting between output ports 3 and 4 is a sinusoidally varying function of z [102]:

$$I_3(z) = I_1 \cos^2\left(\frac{\pi}{2L_0} z\right), \qquad I_4(z) = I_1 \sin^2\left(\frac{\pi}{2L_0} z\right), \tag{11.5}$$

where we have assumed a lossless coupler.

Figure 11.4 shows simulations of the coupling between bus waveguide and RTR as function of the coupling region length L_c and separation gap g.[4] For the linear propagation loss we have assumed a conservative value of $\alpha = 2$ dB/cm, and via separate simulations we have ascertained that for RTR radii of curvature $R \geq 50\,\mu$m, the bending loss is reduced to $\lesssim 0.003\,$dB/360° [58]. The resulting total round-trip loss $\mathcal{L}$ is on the order of a few percent. From the simulation results we observe that for large gaps the mode overlap is too small to achieve efficient coupling to the resonator whereas for very small gaps the energy oscillates back and forth between bus waveguide and RTR as function of the coupling length, cf. (11.5). Furthermore, we observe that for $L_c = 0\,\mu m$ (ring resonator) the coupling efficiency drops off exponentially with gap size. Relevant simulation runs complying with the constraint on lateral feature sizes are plotted in the right-hand panel. It appears that for $g = 500\,$nm the coupling efficiency can be conveniently tuned across and above the full range of expected intracavity loss values (gray dashed line), rendering this gap size a favourable choice for fabrication of over-coupled resonators. Reducing the gap by another 100 nm leads to a strong perturbation of the intrinsic RTR properties

[4] For these simulations we used the FieldDesigner RingResonator module which combines a 2D vectorial mode solver with coupled mode theory to effectively handle 3D problems like curved waveguides and coupling between waveguides.

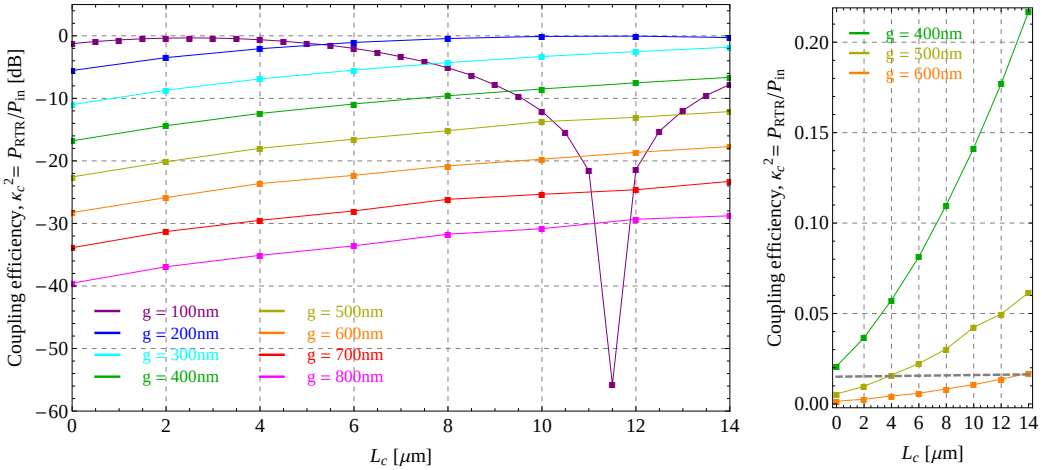

Figure 11.4: Simulated ($\lambda = 850\,\text{nm}$, $t = 250\,\text{nm}$, $w = 500\,\text{nm}$) efficiency of TE_0 coupling between RTR and bus waveguide as function of coupling length L_c. (left) Simulation runs with gap sizes in the range $100-800\,\text{nm}$. (right) Selected simulation runs plotted on linear scale. The gray dashed line indicates the total intracavity loss for an RTR with $R = 50\,\mu\text{m}$ in case of 2 dB/cm propagation loss. Figure adapted from [58].

and the associated increase in η_{esc} comes at a price of a much reduced finesse. The RTR finesse and escape efficiency are given by the approximate expressions

$$\mathcal{F} \approx \frac{2\pi}{\kappa_c^2 + \mathcal{L}}, \qquad \eta_{esc} \approx \frac{\kappa_c^2}{\kappa_c^2 + \mathcal{L}}, \tag{11.6}$$

valid for $\kappa_c^2,\ \mathcal{L} \ll 1$. Table 11.2 summarizes the evaluation of (11.6) using simulation data from Fig. 11.4. For comparison we have also carried through the simulations in case of $\alpha = 1\,\text{dB/cm}$. We observe that for $g = 500\,\text{nm}$ it is indeed possible to achieve escape efficiencies above 80% and maintain $\mathcal{F} > 100$, provided that the waveguide propagation loss can be reduced to about 1 dB/cm.

$\alpha = 1\,\text{dB/cm}$				
L_c	$g = 400$ nm		$g = 500$ nm	
[μm]	η_{esc}	$\mathcal{F}$	η_{esc}	$\mathcal{F}$
4	0.88	96	0.73	207
6	0.91	70	0.79	163
10	*0.94*	*42*	0.84	124
14	*0.96*	*28*	0.88	90

$\alpha = 2\,\text{dB/cm}$				
L_c	$g = 400$ nm		$g = 500$ nm	
[μm]	η_{esc}	$\mathcal{F}$	η_{esc}	$\mathcal{F}$
4	0.79	86	0.59	167
6	0.84	65	0.66	137
10	*0.90*	*40*	0.73	108
14	*0.93*	*27*	0.79	81

Table 11.2: Evaluation of RTR ($R = 50\,\mu\text{m}$) escape efficiency and finesse in case of 1 dB/cm (left) and 2 dB/cm (right) propagation loss. Italicized values indicate that the approximations used in (11.6) are only partially justified.

11.1.4 Chip interfacing

One of the most severe limitations for generation and application of squeezed light in integrated structures is the notoriously large coupling loss associated with interfacing integrated waveguides. Using an external squeezed-light source for on-chip sensing purposes the effective degree of squeezing will be greatly reduced by in- and out-coupling losses[5] and for an integrated source – as targeted here – inefficient collection of the squeezed light on the output side will prevent generation of high-purity states with significantly reduced quantum noise, thereby limiting the source feasibility.

One way of mitigating this problem is to adiabatically match the highly confined waveguide mode to that of, say a single mode fiber, by means of optimized waveguide structures – known as *spot size converters* – at the chip facet. In [58] we proposed one such waveguide design, based on the TriPleX^{TM} waveguide technology developed by LioniX, and we investigated numerically its feasibility. Here, we will just discuss the underlying idea of the proposed design and summarize the previously obtained results. Implementation of non-standard designs will inevitably increase fabrication costs and difficulties considerably but it is paramount that the coupling loss issue is addressed thoroughly in order for integrated quantum optical devices to be of any practical relevance.

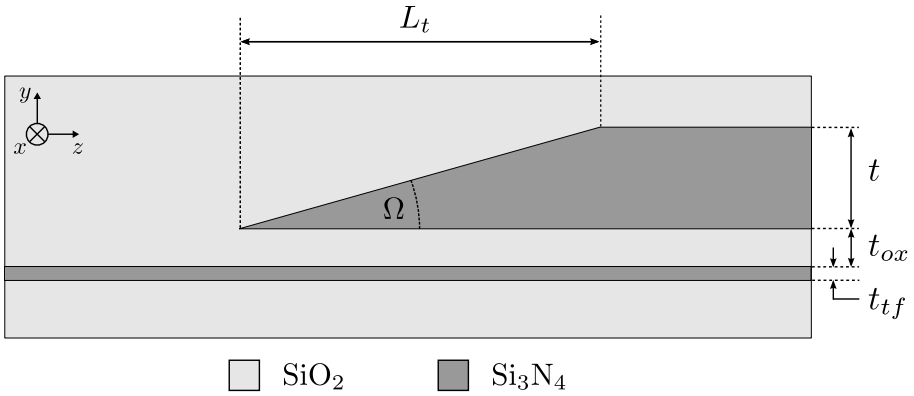

Figure 11.5: Longitudinal cross section of the proposed silicon nitride double layer stack and inverse taper for robust chip coupling. On the left-hand side the lower thin film extends all the way to the chip-air interface and acts as a weakly guiding structure for the incident light. The light is then transferred into the high-confinement upper waveguide by means of the adiabatic inverse taper. The performance of the design depends on optimization of thin film thickness t_{tf}, intermediate oxide layer thickness t_{ox}, and tapering length L_t. Figure adapted from [58].

The design in question is sketched in Fig. 11.5 and consists of an asymmetric silicon nitride double layer stack with inverse vertical tapering of the upper layer. The lower film extends to the chip facet and acts as a weakly guiding structure

[5]Similar to what was observed in the cavity optomechanics experiments in Part II of this thesis.

for the incident light field and serves two purposes: (i) it reduces interface Fresnel losses to ∼4% ($\eta_{Fresnel} = 96\%$), which can in principle be further reduced by anti-reflection coating, and (ii) the mode field diameter of the guided thin film mode can be easily tailored to match that of an incoming mode, e.g. delivered by a lensed fiber, by controlling the film thickness. Light is then transferred to the main high-confinement waveguide by means of the inverse vertical taper. The efficiency of this process relies on optimization of the intermediate oxide layer thickness and the tapering angle Ω being sufficiently shallow for the mode conversion to take place adiabatically. The mode conversion along the structure is illustrated in Fig. 11.7.

An optimal thin film thickness was identified by numerically evaluating the mode overlap between an incident Gaussian mode with a waist of 1 μm (consistent with the use of a lensed fiber) and the fundamental TE mode guided by the film as function of the thickness t_{tf} (Fig. 11.6). As the thickness is thinned down the mode field diameter expands exponentially, reaching an optimal overlap of $\eta_{overlap} \sim$ 98% at a thickness of 60 nm. The exponential mode expansion requires a firm handle on the film thickness during the fabrication process in order to optimize coupling to a specific lensed fiber. To this end the double layer stack design offers a great simplification fabrication-wise. The thin film can be directly deposited with nanometer-control of the thickness using LPCVD and with the protective oxide layer on top, acting as an etch-stop, the nitride etch used to define the inverse taper can be performed without risk of damaging the thin film.

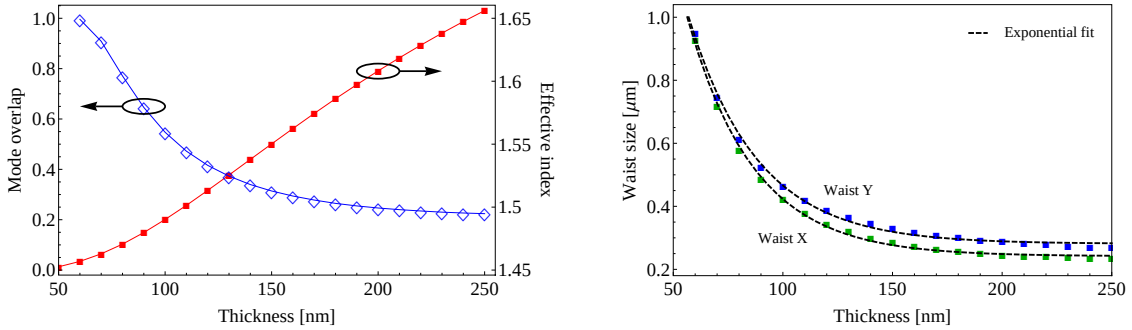

Figure 11.6: Numerical simulations of the fundamental mode guided by the lower thin film as function of thickness. (left) Effective index of the fundamental mode and overlap with a target mode of waist 1 μm. As the film thickness is reduced the effective index approaches that of the cladding, and the mode expands to reach an overlap of about 98% with the target mode at a thickness of 60 nm. (right) Fitted x- and y-waists of the fundamental mode showing an exponential expansion for a decreasing film thickness. Figure adapted from [58].

We have studied the requirements for adiabatic performance of the taper in the context of the theory for delineation of adiabaticity criteria for tapered optical fibers, developed by Love et al. [85, 78]. In combination with numerical calculations of the optical mode properties as function of the instantaneous taper height, we have

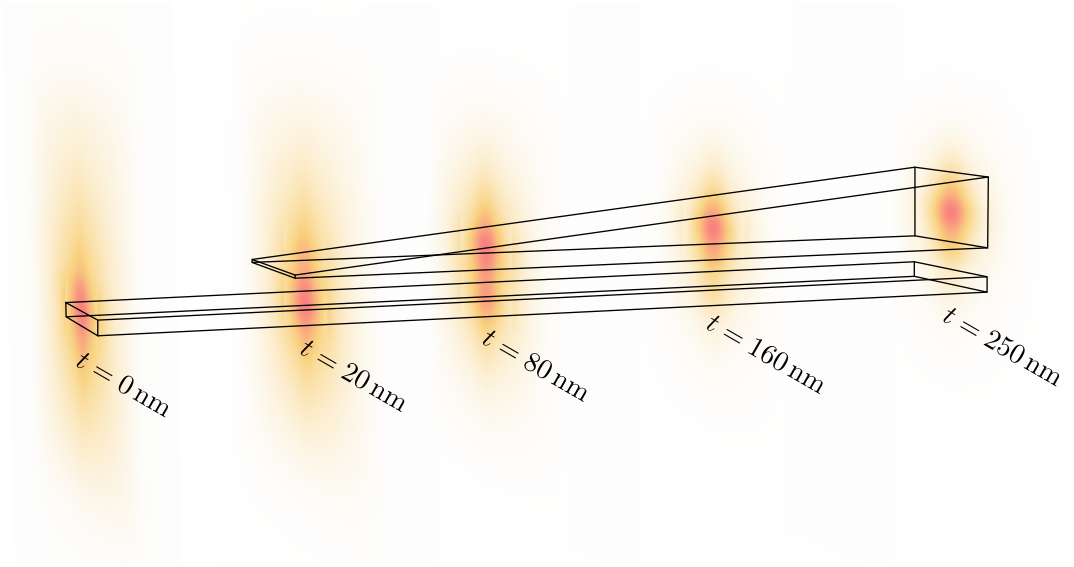

Figure 11.7: Illustration of mode conversion along the inverse taper. At the beginning of the taper (right) the mode is highly confined to the 250 nm thick silicon nitride core. As it propagates towards the chip facet (left) the light is gradually coupled over to the lower thin film while the mode expands more and more into the cladding. The shown modes were calculated numerically for a 500 nm wide double layer stack with a constant lower film thickness of 60 nm, an intermediate oxide thickness of 100 nm, and an upper layer thickness t varied between 0 nm and 250 nm. The cross sectional dimensions of the indicated waveguide structure is to-scale with the the plotted mode profiles but the axial dimension has been compressed in order to accommodate the whole large-aspect ratio structure in the figure.

found that for tapering lengths $L_t \gtrsim 500\,\mu$m the loss is less than 10%. To consolidate this estimate we have performed 2D Beam Propagation Method simulations of the coupling across the taper as function of the intermediate oxide layer thickness. At a thickness of $t_{ox} = 100\,$nm the simulations yield a coupling efficiency similar to the above estimate. We will therefore take $\eta_{taper} = 90\%$ as our best estimate for the taper efficiency.

In summary, the numerical analysis of the double layer stack has resulted in a set of efficiencies which can be combined in an estimate for the over-all fiber-to-waveguide coupling efficiency:

$$\eta_c = \eta_{Fresnel} \cdot \eta_{overlap} \cdot \eta_{taper} \geq 0.96 \cdot 0.98 \cdot 0.90 \approx 84\%, \tag{11.7}$$

corresponding to a coupling loss of only 0.75 dB/facet. Experimental confirmation of this value would be an important step towards feasible integrated high-index contrast structures for quadrature squeezed light generation.

11.1.5 Summary

The numerical investigations suggest that it is indeed possible to design an integrated resonator with characteristics in accordance with the requirements for squeezed-light generation. That said, it is clear from Section 11.1.4 that despite our efforts to devise an efficient and robust chip interfacing mechanism, out-coupling loss from the chip remains a bottleneck for the device performance. Also, the initially assumed propagation loss of 2 dB/cm has turned out to be somewhat on the high side of what is acceptable. The results of Section 11.1.3 indicate that a more tractable trade-off between escape efficiency and intracavity field enhancement is possible if the propagation loss can be reduced to about 1 dB/cm.

To provide a clear and concise overview of the outcomes of the numerical simulations, we list in Table 11.3 all the identified target design values and the derived values which will characterize the performance of the device as a source of squeezed-light. These target values are the exact ones used for the integrated devices which have been fabricated and experimentally investigated during the course of this thesis (see Chapter 12).

11.2 Estimation of device performance

In the preceding chapter we developed a theoretical model of the output squeezing spectrum from an integrated RTR device, showing a third order optical nonlinearity, and in the above section we have discussed numerical simulations leading to an optimized design for such a device. We will now use those results to piece together estimates of the projected device feasibility as a source of squeezed light. This will be done on the basis of a device design as specified by Table 11.3 with the only

Parameter	Sym.	Target	Derived values
Wavelength	λ	850 nm	TE$_0$: $n_{eff} = 1.66$, $A_{eff} = 0.18\,\mu\text{m}^2$
Waveguide thick.	t	250 nm	
Waveguide width	w	500 nm	
RTR radius	R	50 μm	@ 1 dB/cm: $\eta_{esc} = 84\%$, $\mathcal{F} = 124$; @ 2 dB/cm: $\eta_{esc} = 73\%$, $\mathcal{F} = 108$
Bus-to-RTR gap	g	500 nm	
Coupling length	L_c	10 μm	
Thin film thick.	t_{tf}	60 nm	$\eta_c = 84\%$
Oxide layer thick.	t_{ox}	100 nm	
Taper length	L_t	> 500 μm	

Table 11.3: Summary of numerically optimized target parameter values for RTR design.

variable parameter being the RTR power coupling efficiency κ_c^2, bound to the range 2-8%.[6]

Stimulated by the conclusions of Section 11.1 we will assume an uprated linear propagation loss of 1 dB/cm. This is a reasonable assumption as 300 nm thick silicon nitride waveguides have been demonstrated with a loss of only 0.1 dB/cm in the visible [121] and at a wavelength of 900 nm PECVD-fabricated waveguides of 180 nm thickness and 500 nm width with propagation loss < 0.8 dB/cm were recently demonstrated by Subramanian et al. [122]. In order to make realistic estimates for the measurable degree of squeezing the state detection efficiency must also be accounted for. To this end, an out-coupling efficiency of 84% will be used (cf. Table 11.3) and we will take the homodyne mode overlap and detector quantum efficiency to be $\eta_{mm} = \eta_{qe} = 98\%$, resulting in a total detection efficiency of $\eta = 80.6\%$.

Ultimately, the figure of merit is the maximum achievable quantum noise reduction, but other characteristics such as output state bandwidth and purity are also important for the practical applicability of the source. All aspects are treated in [58] but here we will only discuss the results obtained for the former two.

11.2.1 Achievable degree of squeezing

Using the derived expression for the squeezing spectrum in (10.17)-(10.19) and the design values in Table 11.3 we calculate the quantum noise characteristics of the output field from the integrated device as function of escape efficiency, input pump power, and quadrature phase. The corresponding relative noise power tomographies, normalized to the shot noise level, are plotted in Fig. 11.8. We have furthermore

[6] In practice this is realized by variation of the coupling length L_c. Since the associated modification to the nonlinear interaction strength ξ and intra-cavity loss $\mathcal{L}$, through the L_c dependence of the RTR round-trip length, is only on the few-percent level, we will neglect this and assume constant values for these quantities corresponding to $L_c = 12\,\mu m$ ($\kappa_c^2 = 5\%$).

assumed the measurements to be performed at a particular sideband frequency of 30 MHz. Most significantly a quantum noise reduction of about 4.5 dB is observable, confirming the feasibility of the designed device as a source of bright squeezing.

Throughout this part of the thesis we have regularly returned to the issue of determining an optimal trade-off between escape efficiency and cavity enhancement. The importance of it for the system in question stems from the self-driven squeezing interaction and power dependence of the Kerr nonlinearity: it is generally of interest to increase η_{esc} in order to preserve squeezing in the output field, but that inevitably reduces the cavity finesse and thereby the intracavity power driving the squeezing process. And indeed we observe from Fig. 11.8 that for a given pump parameter $|\epsilon|$ (bottom axes) larger squeezing is achievable as the escape efficiency is increased. But the required pump power in the bus waveguide (top axes) also increases, rapidly approaching experimentally intractable levels. For $\eta_{esc} \geq 90\%$ we find that reaching 3 dB of squeezing already requires about 200 mW input pump power.

Taking cross sectional views for a particular pump power of the individual panels in Fig. 11.8 provides the more familiar representation of the output field quantum noise shown in Fig. 11.9. This is how homodyne measurements of the noise would look like as the local oscillator scans through the quadrature phases. From the tendency of the noise minima as function of escape efficiency we infer that an optimum of the sought-for compromise between escape efficiency and cavity enhancement is achieved for $\eta_{esc} = 85\%$. Furthermore, the figure clearly illustrates the admixing of vacuum fluctuations for low escape efficiencies by a rapidly increasing noise in the anti-squeezed quadrature, resulting in output states of low purity [97].

11.2.2 Squeezing bandwidth

As mentioned, another important characteristic of a squeezed-light source is its bandwidth. Most often, cw OPOs based on parametric down-conversion employ cavities with bandwidths of a few tens of MHz, limiting the output bandwidth to a similar value. One exception is monolithic cavity systems [92, 135] where the internal loss is sufficiently low to reach bandwidths up to 170 MHz. In such a system, designed for strong resonant enhancement of the pump field only, weak squeezing at 1550 nm with a bandwidth of more than 2 GHz has been demonstrated [8], and in a later work about 2 dB of squeezing was observed with a bandwidth exceeding 1 GHz [9].

Squeezed light is a widely used resource in quantum communication applications, e.g. for establishing the essential two-partite entanglement for quantum key distribution [29, 89]. In this particular case the key rate is directly linked to the squeezing bandwidth and demonstration of efficient GHz-bandwidth sources is thus an important prerequisite for high-speed protocols. Large-bandwidth squeezed states are also essential for extending the applicability of cv quantum sensing techniques. As an example, state of the art optomechanical photonic crystal devices have mechanical resonance frequencies in the GHz range [108], rendering conventional squeezed light sources insufficient for enhancing the transduction sensitivity.

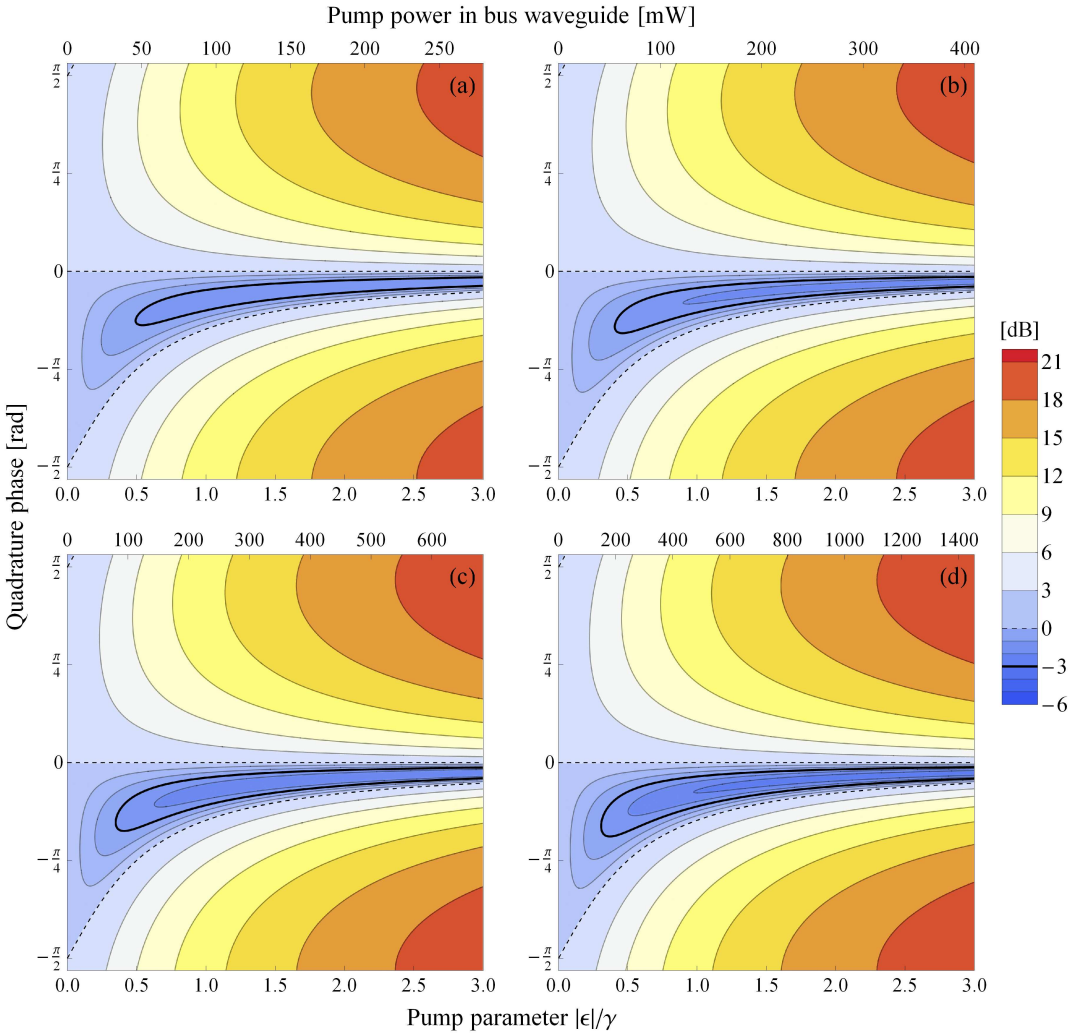

Figure 11.8: ($\lambda = 850\,\mathrm{nm}$, $\alpha = 1\,\mathrm{dB/cm}$, $\eta = 80.6\%$, $\Omega/2\pi = 30\,\mathrm{MHz}$) Relative noise power in the output field of a resonantly pumped RTR ($\Delta_\mathrm{p} = |\epsilon|$) as function of pump parameter $|\epsilon|$. Panels (a)-(d) correspond to RTR escape efficiencies of 75%, 80%, 85%, and 90% respectively. The shot noise level is indicated by the dashed contour and the solid black contour corresponds to 3 dB quantum noise reduction. Figure adapted from [58].

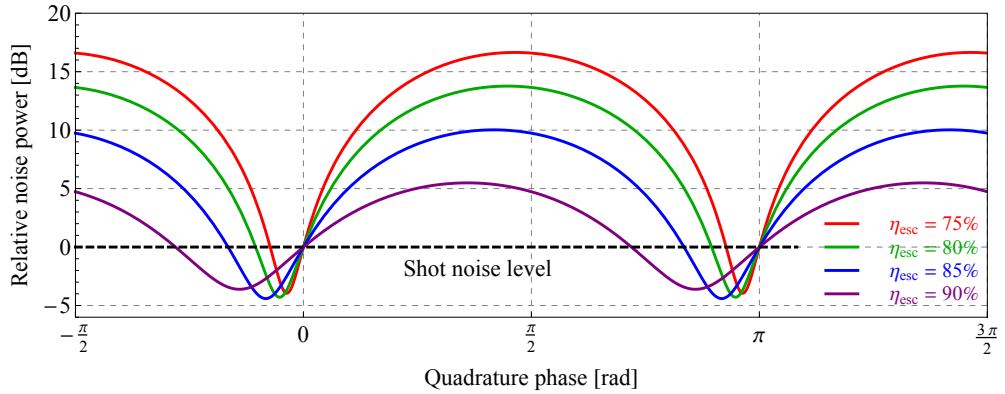

Figure 11.9: ($\lambda = 850\,\text{nm}$, $\alpha = 1\,\text{dB/cm}$, $\eta = 80.6\%$, $\Omega/2\pi = 30\,\text{MHz}$) Cross sectional views of panels (a)-(d) in Fig. 11.8 for an input pump power of 200 mW. Figure adapted from [58].

The squeezing spectrum of the discussed integrated device is plotted in Fig. 11.10 and evidently it has potential to fulfill the above requirements for a broadband source. The shown squeezing and anti-squeezing spectra correspond to $|\epsilon|/\gamma = 0.5$

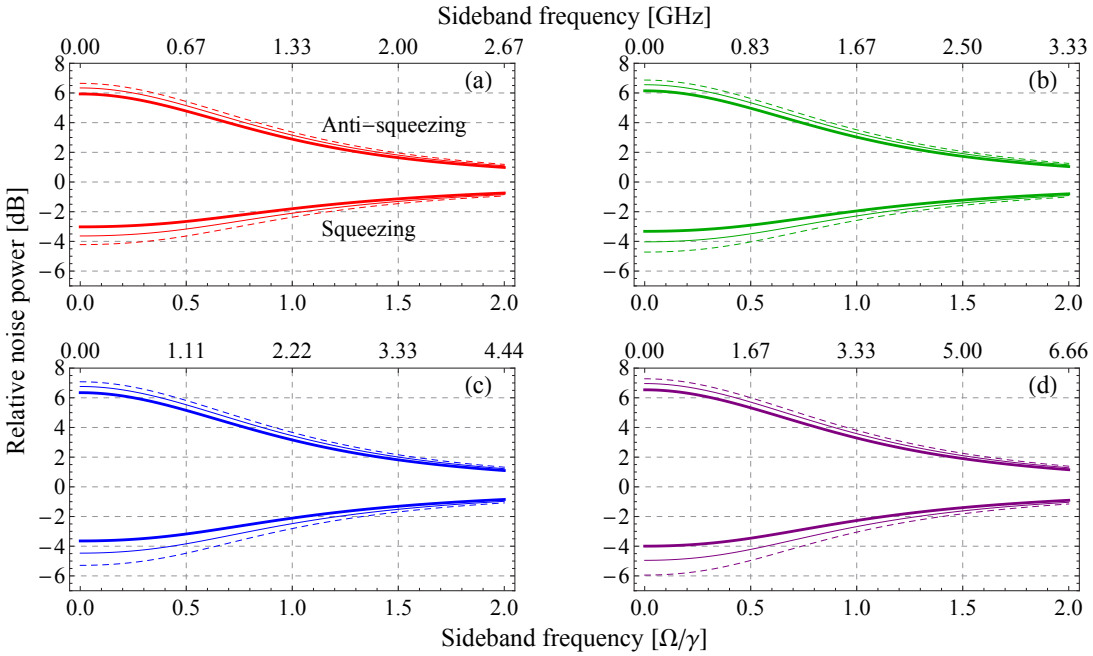

Figure 11.10: ($\lambda = 850\,\text{nm}$, $\alpha = 1\,\text{dB/cm}$, $|\epsilon|/\gamma = 0.5$) Spectrum of the squeezed and anti-squeezed quadratures assuming 80.6% (thick), 91.2% (thin), and unity (dashed) detection efficiency. Panels (a)-(d) correspond to RTR escape efficiencies of 75%, 80%, 85%, and 90% respectively. Figure adapted from [58].

for the same escape efficiencies as in Fig. 11.8. With a total detection efficiency of

80.6% ($\eta_c = 84\%$) the output field shows more than 2 dB quantum noise reduction over a bandwidth larger than 1 GHz across all four η_{esc}-values. With the ability to increase the detection efficiency to 91.2% ($\eta_c = 95\%$) more than 3 dB squeezing is expected over a bandwidth of 1.5 GHz for $\eta_{esc} \geq 85\%$.

Experimental work 12

> "We have a habit in writing articles published in scientific journals to make the work as finished as possible, to cover all the tracks, to not worry about the blind alleys or to describe how you had the wrong idea first, and so on. So there isn't any place to publish, in a dignified manner, what you actually did in order to get to do the work."
>
> – R. P. Feynman
> opening line of Nobel Lecture 1965 [41].

–Well, maybe a thesis is the perfect place?

In this chapter we discuss the experimental efforts made towards demonstrating the feasibility of integrated silicon nitride racetrack resonators as sources of bright squeezed optical fields. As will become evident, this work has not followed a straight road to success, but rather explored a bumpy trail up and down the technical pitfalls of developing a novel on-chip quantum light source. In particular, the challenges associated with interrogating the quantum noise of bright fields has been more severe than anticipated, and so far they have only been partially tackled.

12.1 Realization of integrated silicon nitride devices

An imperative prerequisite for the work discussed in this chapter was the materialization of integrated silicon nitride resonators fabricated as per the design devised in Chapter 11. It was initially planned that the microfabrication should be undertaken at the in-house cleanroom facility Danchip, which would in principle allow for an iterative optimization procedure with feedback from the optical experiments. And a lot of time was spent in the cleanroom trying to do so – both by the author and by Ying-Wei Lu who was a postdoc in the group at the time – but it was relatively soon realized that the lack of previous experience in the group with fabrication of low-loss silicon nitride waveguide structures would make it exceedingly difficult to achieve the set goals within the time frame of the project.

From the research literature on silicon nitride waveguide devices we were aware that the foundry LioniX based in Enschede, The Netherlands, had previously been involved in fabrication of silicon nitride waveguide devices achieving state-of-the-art

propagation loss figures. Motivated by the unsuccessful in-house fabrication efforts we initiated a correspondence with the company in April 2013, and five months later an order was placed with LioniX. Finally on April 25th 2014 we received the first batch of silicon nitride devices. Figures 12.1 and 12.2 below show top view and cross sectional SEM micrographs of exemplary devices from the batch. Details on the mask used for the microfabrication process are provided in Appendix C.

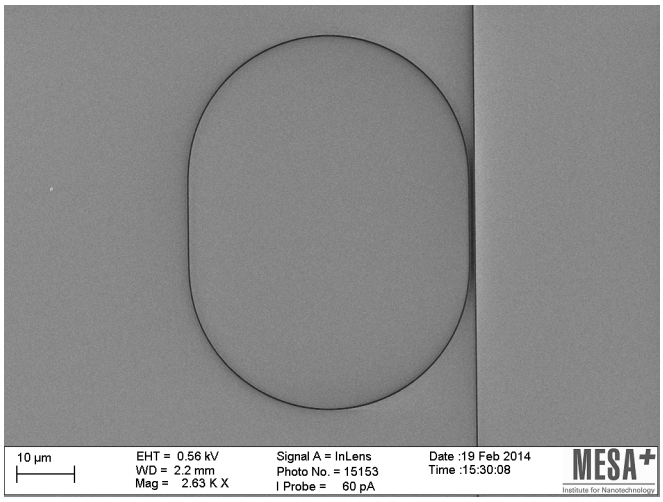

Figure 12.1: SEM micrograph of a silicon nitride RTR side-coupled to a bus waveguide prior to deposition of the upper oxide cladding layer. The particular device has a 25 μm radius of curvature. Image courtesy of E. Schreuder (LioniX BV).

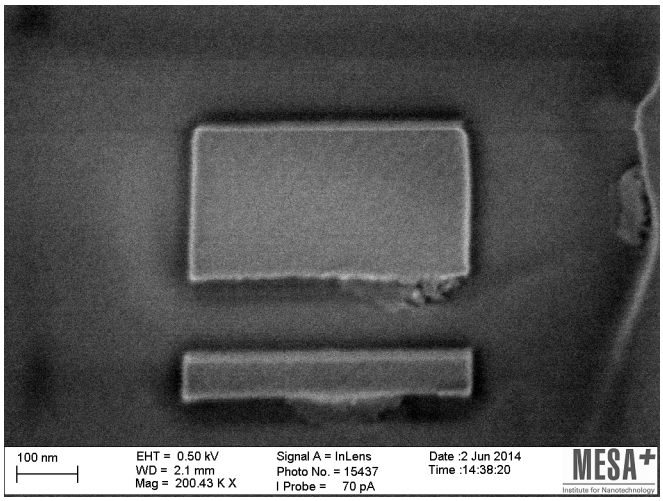

Figure 12.2: SEM micrograph of the cross sectional waveguide structure showing the double layer stack architecture. The width of the particular waveguide is slightly smaller than the target value of 500 nm. Image courtesy of E. Schreuder (LioniX BV).

With the aim of exploring a range of RTR configurations, and to account for possible deviations from the expected loss figures provided by vendor, a number of different device configurations were accommodated in the first batch. More specifically, the fabricated devices include side-coupled RTRs with radii of curvature R of 25 μm, 50 μm, and 75 μm, and for each RTR size the coupling lengths L_c is varied across values of 2, 5, 8, 9, and 10 μm. Also, straight waveguides without RTRs were included on each chip, intended for spatial mode shaping of the local oscillator field. Finally, a large number of propagation loss calibration chips were included, consisting of spiral delay line waveguides for cut-back measurements, covering 8 different lengths between 0.5 cm and 8 cm (cf. Section 12.4.1).

12.2 Titanium sapphire laser

As mentioned in Chapter 6, working with optical microresonators requires a widely tunable laser source, simply because the free spectral range scales inversely with the resonator round-trip length, e.g. the target RTR design in Table 11.3 has a circumference of 334 μm resulting in a free spectral range of 540 GHz. For an over-coupled RTR, resonance linewidths (FWHM) of about 4-5 GHz are expected, and for characterization purposes a suitable laser should be capable of scanning continuously across a frequency range larger than that. Last, but not least, the application of squeezed light generation requires the laser to be shot noise limited. Considering these requirements a cw Ti:sapphire (Ti^{3+}:Al_2O_3) laser system is an adequate choice for the experiment. The operational principle of the Ti:sapphire laser is determined by the state of the outer 3d electron of the Ti^{3+} ion, and the large wavelength tuning range, approximately covering the range 650 - 1100 nm, is a result of state broadening because of coupling to lattice vibrations of the bulk crystal (see Fig. 12.3).

12.2.1 SolsTiS-SRX operation in brief

Thus motivated, the SolsTiS-SRX laser produced by M-Squared was selected as light source for the experiment. It is a cw Ti:sapphire laser, which in our configuration is pumped by a 532 nm 10 W Finesse laser from Laser Quantum. Using the full 10 W pump power the maximum output of the SolsTiS is 2.6 W at 780 nm. However, the system was usually operated at reduced pump power levels of 9 W or 7 W with a corresponding SolsTiS output at 850 nm of 1.96 W or 1.35 W, respectively. This is already more than plenty for the application and thus the power was generally reduced significantly, using external high-power polarization optics. As shown in Fig. 12.4 the SolsTiS has a traveling wave bow-tie laser cavity layout. Coarse tuning of the output wavelength is accomplished by rotating the birefringent filter (BRF) and fine tuning by electronically adjusting the étalon spacing (FSR $\sim$ 0.5 nm). For long-term single mode operation the étalon can be locked by means of a servo using a dither technique. In the SRX model, a small fraction of the laser output

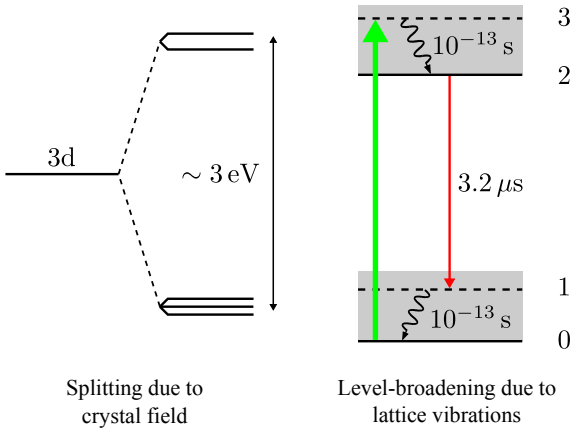

Figure 12.3: The Ti:sapphire laser operation is determined by the outer electron of the Ti^{3+} ion. In the presence of the crystal field the inital 3d state splits into a 3-fold degenerate ground state and a 2-fold degenerate excited state, separated by approximately 3 eV. Due to coupling to the large number of lattice vibrations of the bulk crystal the discrete levels are turned into continuous distributions of ground and excited states. This leads to the formation of an effective 4-level laser scheme: the pump excites the electron from its ground state (level 0) to the excited state (level 3), followed by a fast relaxation to the lowest excited-state (level 2). An optical transition then occurs to a vibronic level of the ground state (level 1), and another fast relaxation process takes the Ti^{3+} ion back to its ground state [104].

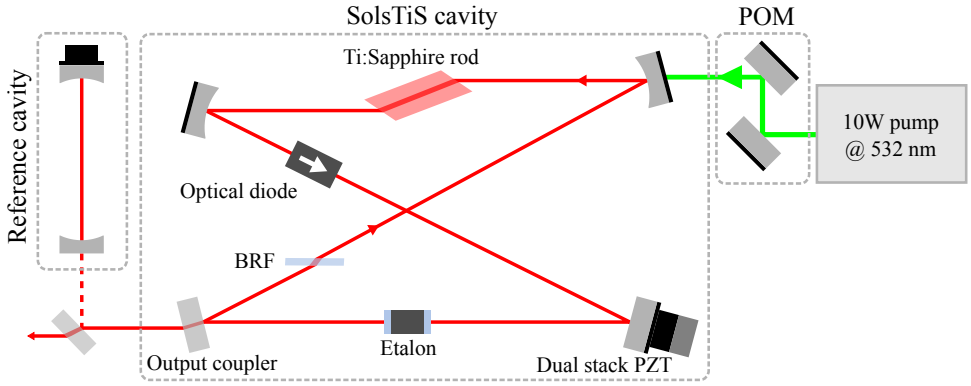

Figure 12.4: Schematic illustration of the M-Squared SolsTiS-SRX intracavity layout including reference cavity and pump optics module (POM) for pump beam alignment.

is directed to a temperature stabilized reference cavity ($\mathcal{F} = 47$, FSR = 3 GHz) for linewidth narrowing (<50 kHz relative to reference cavity) and to ensure single mode operation during frequency scanning. With the system locked (both étalon and reference cavity) the laser cavity is slaved to the reference cavity through servo feedback to the fast part of a dual stack piezo actuator on one of the intracavity mirrors. In this configuration the laser output frequency is scanned by scanning the length of the reference cavity.

12.2.2 Laser noise properties

An essential prerequisite for measuring squeezing is to assure that the laser – serving both as pump for the squeezing process and as local oscillator for the detection – is in fact shot noise limited from a certain frequency on. For the $\chi^{(3)}$-based squeezing process investigated here, shot noise limitation of the pump is absolutely necessary as the Kerr effect is intrinsically sensitive to fluctuations in both amplitude and phase quadrature of the pump field [133]. In the following we present the results of two types of measurements that have been performed in order to characterize the noise properties of the laser.

Relative intensity noise measurement

First, we have characterized the noise in the power emitted from the laser, commonly termed *intensity noise*. The total time-dependent power can be considered composed of two parts:

$$P(t) = \langle P \rangle + \delta P(t), \tag{12.1}$$

where $\langle P \rangle$ is the time-averaged mean power and $\delta P(t)$ a noise term with $\langle \delta P(t) \rangle = 0$. The most common quantitative measure of the noise is the *relative intensity noise (RIN)* , defined as the power noise normalized to the total average power [98],

$$RIN = \frac{\langle \delta P(t)^2 \rangle}{\langle P \rangle^2}. \tag{12.2}$$

Using that the noise power measured over a bandwidth Δf is related to the noise spectral density by $\langle \delta P(t)^2_{\Delta f} \rangle = 2\Delta f S_P(\Omega)$, where the factor of 2 accounts for both positive and negative frequencies, we can express the RIN spectral density as

$$RIN = \frac{2S_P(\Omega)}{\langle P \rangle^2}, \tag{12.3}$$

which is ultimately the quantity of interest.

Experimentally, the RIN is measured by converting the optical signal to an electrical signal by means of a fast photodetector (Thorlabs PDA-10A, 150 MHz bandwidth). Exploiting that the electrical power is proportional to the optical power squared, $P_E = k\langle P \rangle^2$, the RIN can be evaluated as the corresponding ratio of electrical power fluctuations to total electrical power [99]. Both quantities are readily

measured using an oscilloscope and a spectrum analyzer, respectively (Fig. 12.5). The total photocurrent noise power $\Delta P_E(\Omega)$ is the sum of laser noise $N_L(\Omega)$ and technical noise $N_T(\Omega)$ from the detector and the spectrum analyzer, and the relevant spectral density of the laser noise can be deduced as

$$2S_P(\Omega) = \frac{\Delta P_E(\Omega) - N_T(\Omega)}{\Delta f}, \tag{12.4}$$

where Δf is given by the resolution bandwidth (RBW) used for the measurement. The average electrical power is determined from the dc photocurrent as $P_E = g_T I_{dc}^2$, where g_T is the transimpedance gain of the detector. The actually measured value is the output voltage from the detector, given by $U_{out} = R_{out} I_{dc}$, where R_{out} is the detector output impedance. Combining the expressions we find

$$P_E = U_{out}^2 \frac{g_T}{R_{out}^2}. \tag{12.5}$$

Combining (12.4) and (12.5) we can express the RIN in terms of experimentally measurable quantities,

$$RIN = \frac{R_{out}^2}{U_{out}^2} \frac{\Delta P_E(\Omega) - N_T(\Omega)}{g_T \Delta f}. \tag{12.6}$$

Since the purpose of the measurement is to verify that the laser is shot noise limited from a certain frequency on, the theoretically expected shot noise level must be evaluated as well as function of the mean total optical power. Following [99] the shot noise is given by

$$N_{sn} = 2q g_T I_{dc} = 2q U_{out} \frac{g_T}{R_{out}}, \tag{12.7}$$

where q is the elementary charge. Normalization to the total power yields the corresponding RIN level

$$RIN_{sn} = \frac{2qR_{out}}{U_{out}}. \tag{12.8}$$

Using the setup sketched in Fig. 12.5 we have measured the RIN of the SolsTiS laser output. The corresponding data is plotted in Fig. 12.6. At frequencies around 1 MHz strong intensity fluctuations are observed due to relaxation oscillations of the laser, but for higher frequencies shot noise limited performance is achieved. For a power of 2.78 mW the laser is shot noise limited from 3 MHz and up. Extrapolating the tendency of the data to higher power levels we find that the laser is shot noise limited at a power of 200 mW from a frequency of about 7 MHz and up.

Homodyne measurement

To fully characterize the laser noise properties a second set of measurements were performed using balanced homodyne detection (cf. Sec. 2.2.3) to acquire full tomographic information about the field fluctuations as function of detection frequency.

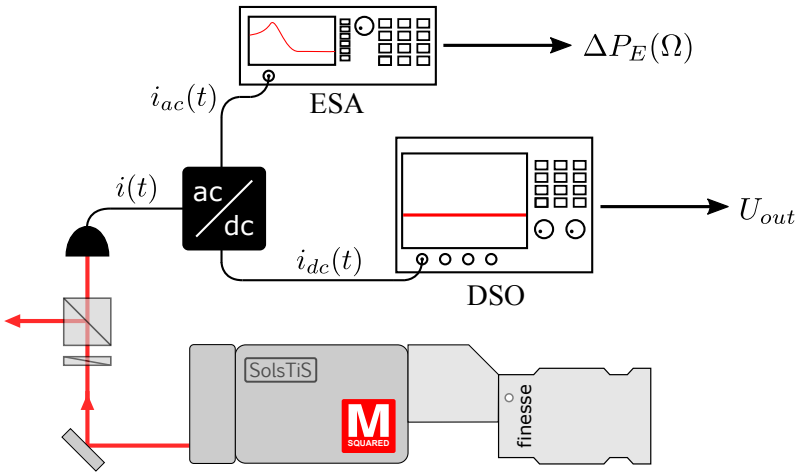

Figure 12.5: RIN measurement setup. The generated photocurrent is split using an ac/dc splitter. The ac signal is directed to an electronic spectrum analyzer for measuring the noise power spectrum and the dc part is monitored on a digital oscilloscope for measuring the total electrical power. The optical power level is controlled using a $\lambda/2$-plate and a polarizing beamsplitter cube.

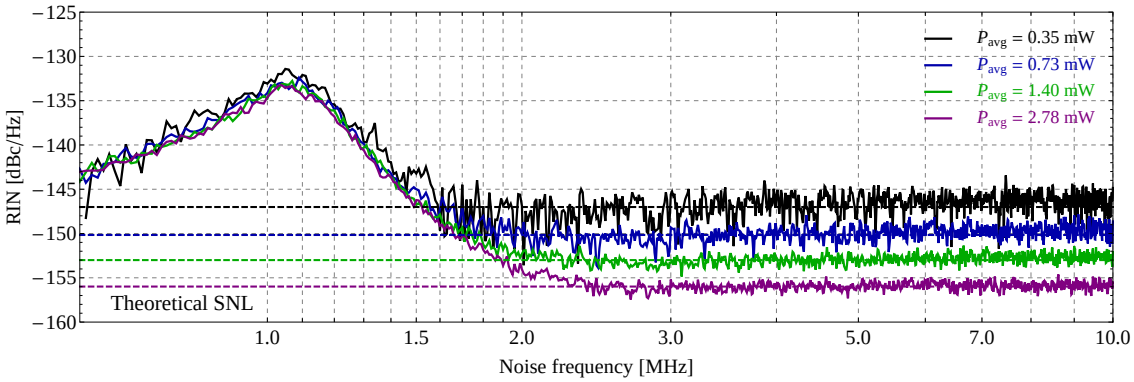

Figure 12.6: Relative intensity noise measurement of SolsTiS laser output at four different power levels. The optical power was detected using a Thorlabs PDA10A photodetector with $g_T = 10\,\mathrm{kV/A}$ and $R_{out} = 50\,\Omega$. The data was recorded with RBW $= 91\,\mathrm{kHz}$. Dashed lines indicate the theoretical shot noise levels for the used optical powers calculated from (12.8). Accounted for in the analysis is also a measured 6 dB attenuation of the ac photocurrent by the ac/dc splitter and the $50\,\Omega$ input impedance of the spectrum analyzer.

The high-pass filtered differential homodyne photocurrent has directed to a spectrum analyzer and measured in zero-span mode for different detection frequencies, while slowly sweeping through the noise quadratures by a low-frequency scan of the LO phase. Figure 12.7 shows the result of such measurements for detection frequencies $\Omega = 1, 1.5, \text{and } 2\,\text{MHz}$. From the previous RIN measurements we know that the laser exhibits large excess amplitude noise at low frequencies and that enables us to identify the upper turning points of the quadrature noise trace as amplitude quadrature measurements. In between maxima the noise drops to the shot noise level meaning that excess phase noise is not present in the light field. Also we observe that that the excess amplitude noise vanishes for increasing frequencies. A characterization of the homodyne detector performance is provided in Appendix E.

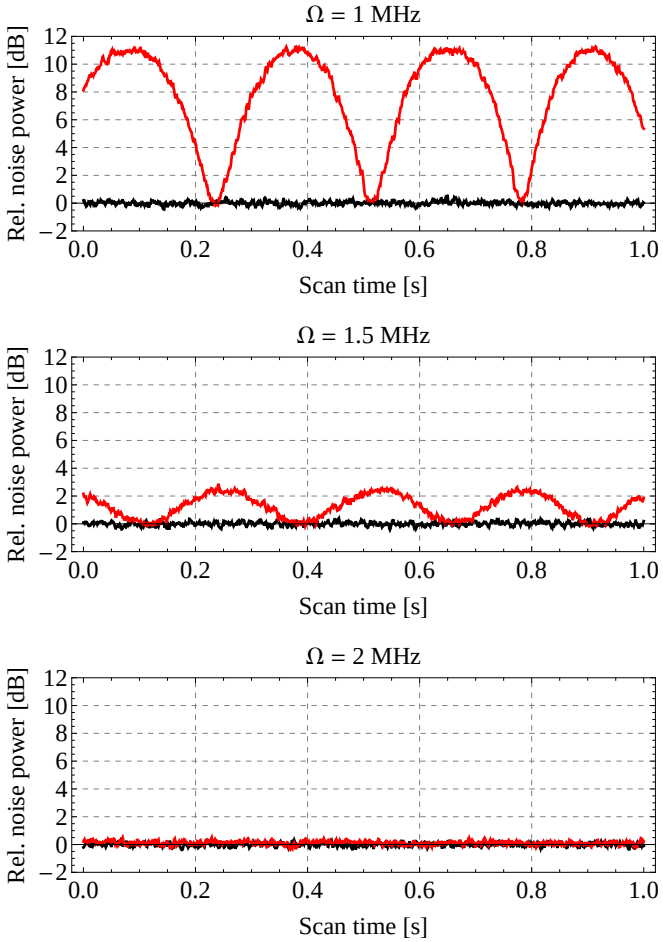

Figure 12.7: Homodyne measurement of laser output noise. Black: shot noise, Red: quadrature noise. Signal power, 24 μW; local oscillator power 6.1 mW; mode matching visibility 96.9%. Zero-span, RBW=200 kHz and VBW=82 Hz.

12.3 Experimental setup

We are now finally in a position to present the devised setup for optical experimentation with the acquired integrated silicon nitride resonators and discuss the efforts made so-far towards demonstration of on-chip quadrature squeezing. As is always the case, this experimental system has also been an ever-evolving organism and the setup outlined in Fig. 12.8 is just the latest iteration. In particular, the state interrogation stage has been a perpetual construction site, as discussed in later sections. For the characterization measurements presented in Section 12.4 only the "signal"

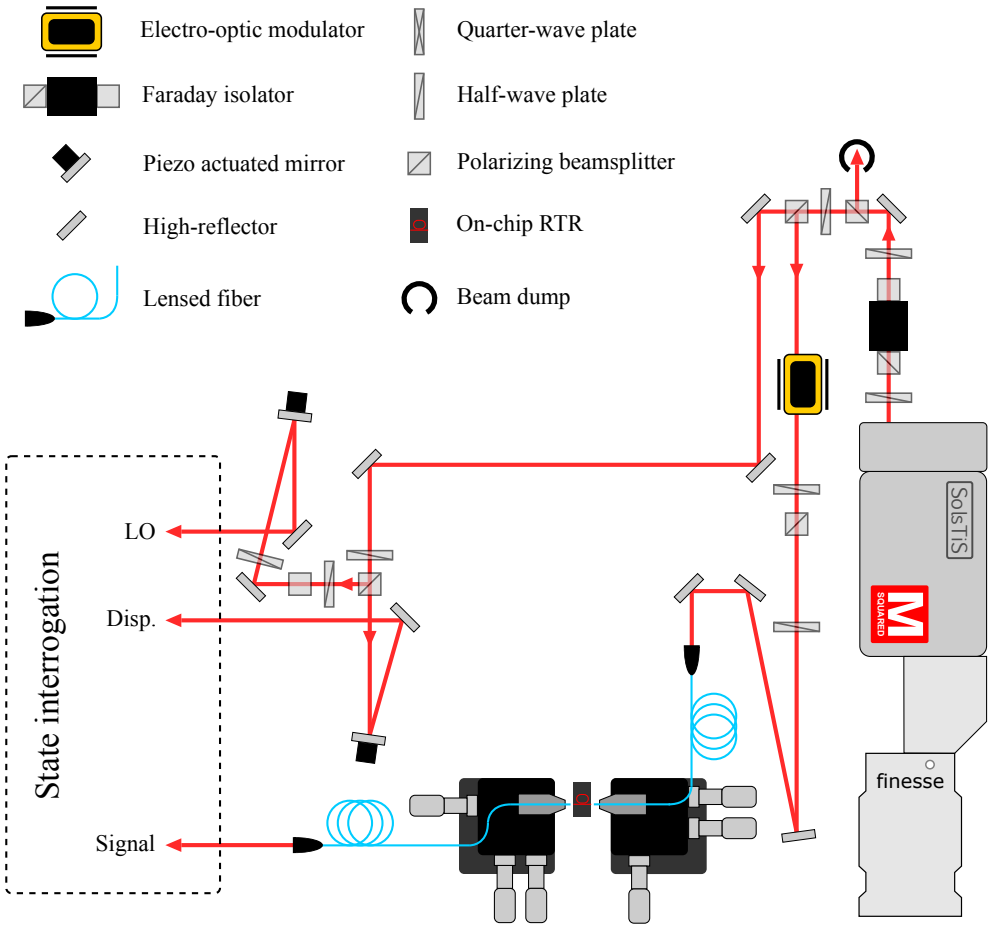

Figure 12.8: Schematic illustration of the experimental setup (lenses have been omitted for the sake of clarity). Aspherical lenses are used for fiber in- and outcoupling - on the input side a Thorlabs C560-TME (f = 13.86 mm) and on the output side a New Focus 5724-H-B (f=8.0 mm); EOM - New Focus 4002; Faraday isolator - Linos FI-850-5SV; High reflectors in signal beam - Layertec #109770; PBSs - B. Halle PTW 1.10 *or* CVI PBS-830-040; Half-wave plates - B. Halle RZQ 2.10 (zero order) *or* Eksma d20 ZO l/2@852 nm (zero order); Quarter-wave plate - B. Halle RZQ 4.10 (zero order); Lensed fiber - OZ Optics TSMJ-3A-780-5/125-0.25-5-2-10-1-AR (single mode at 780 nm, AR coated for 720-860 nm).

beam path was used and in this case the chip output was just detected with a simple photodetector. The more involved state interrogation techniques implemented for quantum noise measurements of the output field from the chip will be presented in Section 12.5.

12.4 Chip characterization measurements

Prior to any attempts of generating on-chip squeezed states, the integrated devices were subjected to a series of optical characterization measurements in order to asses the optical loss properties of the waveguides and loaded quality factors of the RTRs as function of coupling efficiency. We were especially curious to evaluate the chip-fiber coupling loss to see if the tapered double layer stack design would actually perform according to the promising numerical estimates.

12.4.1 Characterization I: Coupling and linear propagation loss

We have previously seen that the integrated device is associated with two types of loss – coupling loss and propagation loss – and together they constitute the total *insertion loss* of the device. In the theoretical analysis above we have learned the importance of knowing the individual contributions of the two loss sources as they affect different aspects of the device performance. The cut-back method enables an experimental evaluation and separation of these losses. The underlying assumption of the method is that the coupling loss into each waveguide is the same, and that propagation losses depend linearly on the waveguide length. In this case a series of measurements of the total insertion loss for step wise reductions (cut backs) of the length enables fitting of the loss suffered per unit length. And by extrapolation the total coupling loss can be determined as the inflicted loss at zero length. The method has its origin in the fiber optics community where reduction of the propagation length can easily be done by cleaving the fiber. For integrated waveguides this is more tricky, and for the particular ones considered here it is not even possible because of the inverse waveguide tapers. A common implementation of the method is instead to use a series of spiral delay-line waveguides with different lengths (Fig. 12.9).

Figure 12.10 (a) shows exemplary data for such measurements. These measurements were taken using a lensed fiber for in-coupling and collecting the output with a high-NA objective[1]. The waveguide insertion loss is calculated relative to the transmission measured with the fiber output coupled directly to the objective. The corresponding fitting results are summarized in Table 12.1, and we see that the measured propagation loss is consistent with the values assumed in Chapter 11. For comparison a second cut-back measurement was performed on W2315-2/0D but using lensed fibers for both in- and out-coupling. The two measurement are plotted

[1]Spindler & Hoyer, x63/0.85.

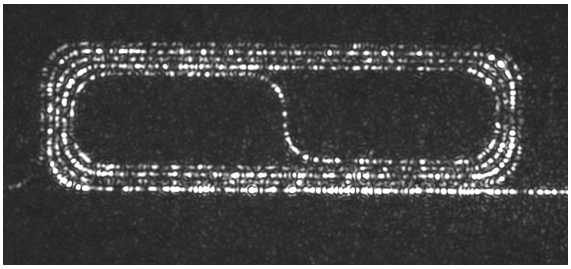

Figure 12.9: Photo of an optically excited spiral delay-line waveguide with a total length of 3 cm.

together in Fig. 12.10 (b). The two measurements yield very similar propagation loss values but the coupling loss is 1.69 dB larger for the dual-fiber configuration. Consequently, we find a coupling loss of 2.66 dB/facet using lensed tapered fibers. This is a somewhat disappointing result compared to the theoretical value of 0.75 dB/facet anticipated in Section 11.1.4, and we wish to investigate this issue further in the future. Also relevant would be to extend the above characterization by quantifying the separate contributions to the total measured loss due to scattering and linear absorption. A convenient technique for doing so has been presented by Borselli et. al. [20].

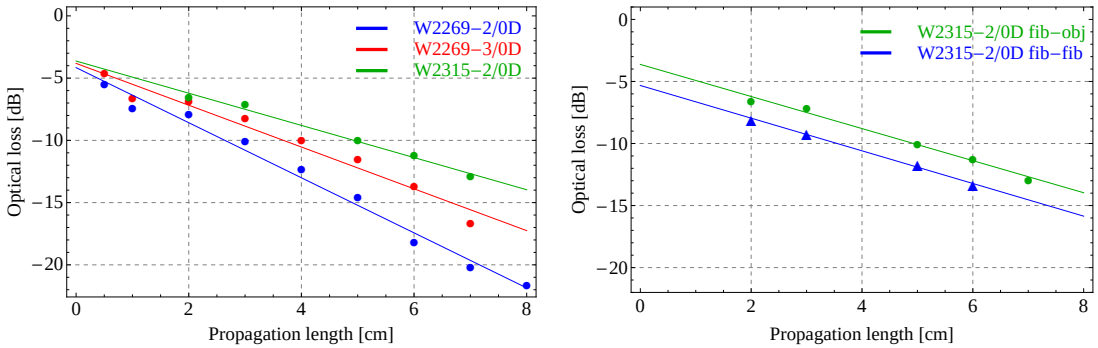

(a) (b)

Figure 12.10: (a) Exemplary cut-back measurements of propagation loss for three different characterization chips from wafers W2269 and W2315. Some of the characterized waveguides exhibited abnormally large loss due to presence of strong scattering centers in the guide. The corresponding measurement points have been omitted. (b) Comparison of cut-back measurements performed using high-NA objective (green) and lensed fiber (blue) for chip out-coupling.

12.4.2 Characterization II: RTR resonances

To map out the RTR resonances and evaluate the corresponding Q values, the laser is first tuned on resonance by tuning the BRF and étalon. The chip is simulta-

Chip ID#	**Propagation loss** [dB/cm]	**Coupling loss** [dB]
W2269-2/0D	2.21 ± 0.10	4.15 ± 0.47
W2269-3/0D	1.68 ± 0.13	3.81 ± 0.54
W2315-2/0D	1.29 ± 0.08	3.63 ± 0.40
*W2315-2/0D	1.31 ± 0.06	5.32 ± 0.25

Table 12.1: Fitted propagation and coupling loss from the cut-back measurements shown in Fig. 12.10 (a) and (b). Dual-fiber measurement result is marked with *.

neously monitored using an imaging system positioned vertically above[2], and the laser frequency is tuned into the resonance until a maximum intensity of the observed scattered light is reached. As shown in Fig. 12.11 the scattered light intensity largely depends on resonator Q value due to the different intracavity field enhancement factors. Fast sweeps of the laser frequency across the resonance are then made by scanning the reference cavity length using an external symmetric triangular ramp signal. We have found that the SolsTiS comfortably performs frequency sweeps over a range of 25 GHz around 850 nm.

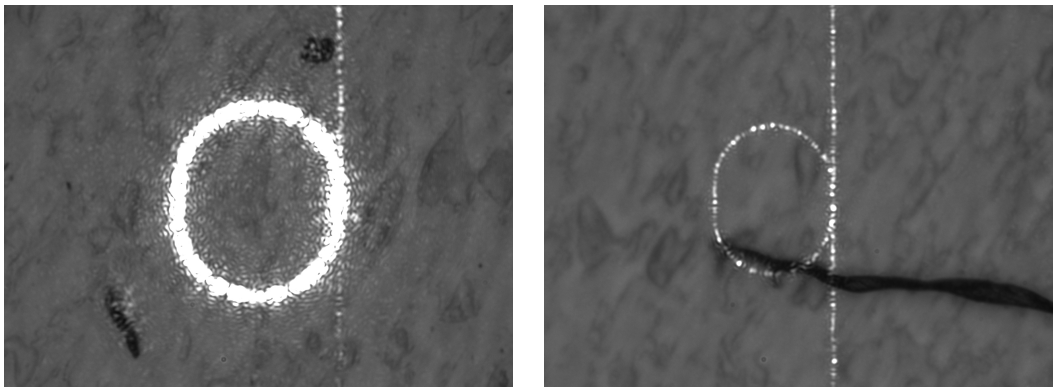

(a) (b)

Figure 12.11: Observed scattering from two resonantly excited RTRs. (a) High-Q resonator with $L_c = 2\,\mu$m. (b) Low-Q resonator with $L_c = 10\,\mu$m.

Exemplary transmission measurements for a series of adjacent RTRs in a group of 5 waveguides, for which the coupling length is gradually increased, are shown in Fig. 12.12. As expected, the fitted linewidths are in the few-GHz range, and increase for larger coupling lengths – only the last one deviates somewhat in that respect. The measured quality factors are generally in the range of about $Q = 6 \cdot 10^4$ to $Q = 10^5$.

[2]Navitar 12X Zoom mounted with a CCD camera.

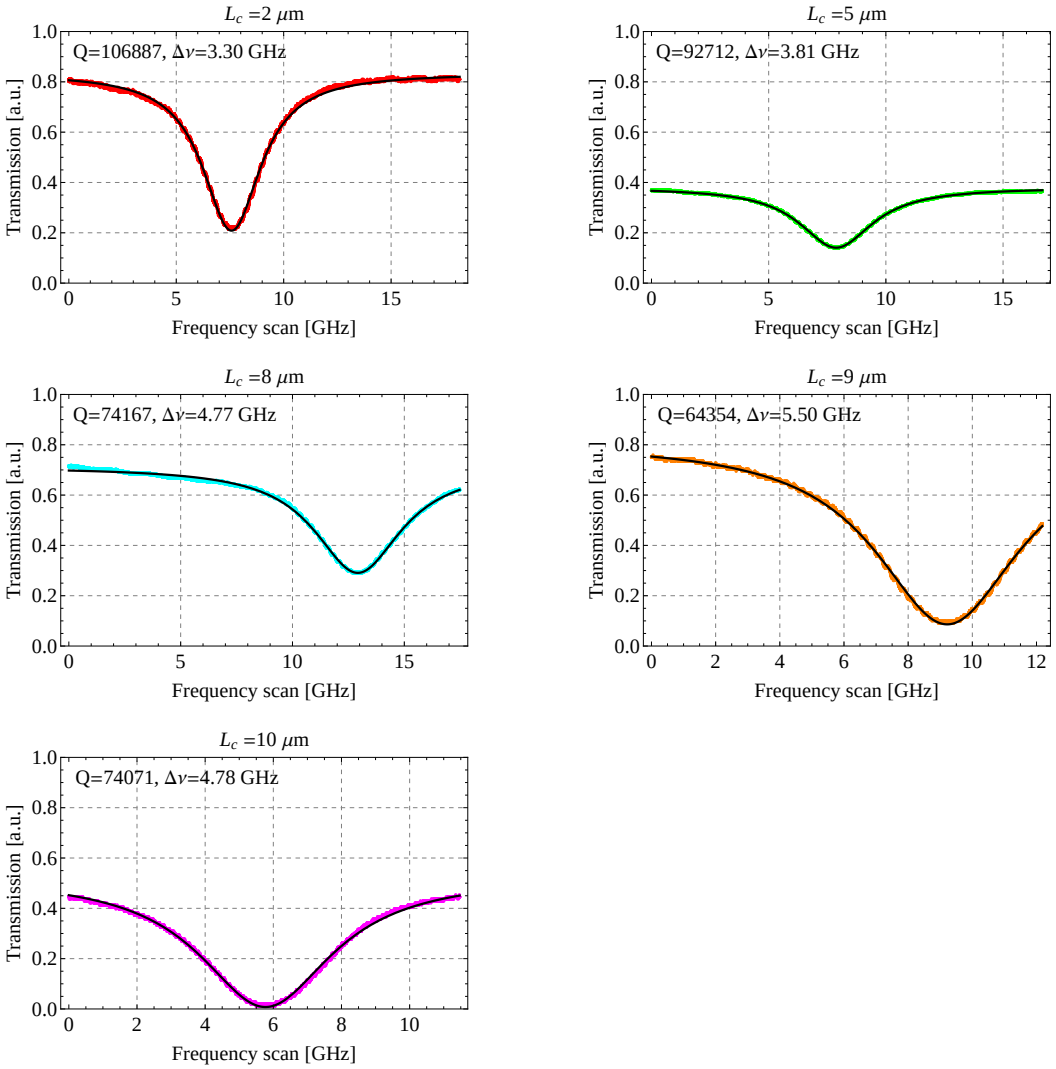

Figure 12.12: Transmission measurements of RTR resonances for waveguides W2315-2/4B-21 to W2315-2/4B-25.

12.5 Interrogation of the chip output noise

The primary goal of this project has been to demonstrate generation of squeezed light from the integrated resonant circuits discussed at length in the preceding, and to that end a quantum noise limited tomography of the output state quadrature noise is required. Performing state tomography of the quantum noise properties of a weak field is generally straightforward to do by implementation of a homodyne detection scheme, as already shown previously in this chapter and for squeezed light in the context of cavity optomechanics in Part II. Unfortunately, it is not as easily done for the chip output field because of the high optical powers needed to pump the weak third order nonlinearity, and because the (potentially) generated squeezing resides at rf sideband frequencies around the intense pump, making it difficult to separate the two parts.

In the following sections we discuss, in chronological order of implementation, the strategies by which detection of squeezing in the chip output field (henceforth simply referred to as the signal) has been attempted. Sadly, none of them has proven successful yet, and the work is still on-going. For that reason we will predominantly keep the presentation at a discussion-level and focus on identifying the crux for why the individual schemes did not work out.

12.5.1 Take I: Homodyne measurement

With the hope of performing a standard balanced homodyne characterization of the signal we first attempted to separate the rf sidebands from the bright pump by means of a "high" finesse cavity, which on resonance would transmit the pump and reflect off sidebands with frequency larger than the cavity linewidth. For the scheme to work optimally, the cavity should be impedance matched, as otherwise a portion of the bright pump will be back-reflected as well, and the linewidth should be sufficiently narrow that far-of-resonance sidebands are still within the bandwidth of the detector. Finally, a robust servo lock for stabilizing the cavity resonance to the pump frequency should be implemented. The actually implemented setup is illustrated in Fig. 12.13. For a number of reasons that seemed good at the time, a linear Fabry-Perot cavity with a finesse of $\mathcal{F} = 1300$ and a linewidth of $\Delta\nu = 1\,\mathrm{MHz}$ was opted for. In retrospect a ring cavity geometry would probably have been preferable as that facilitates separation of the reflected light from the bright incident signal, avoiding the need of an optical isolator for the purpose. For frequency stabilization of the cavity a servo controller was built and tailored for the particular application through iterative optimization of the circuit based on measurements of the feedback loop transfer function and notching of resonances.

As a first obstacle it was realized that the cavity impedance matching was only 96%. As shown in Appendix E, shot noise limited operation of our homodyne detector was limited to a total power of 10 mW, and to safely meet the homodyne approximation the reflected signal power should thus be reduced to below at least

200 μW. Given the high signal power – with 150 mW incident on the in-coupling fiber several tens of milliwatts were collected on the output, the exact value depending on the selected RTR – and the 4% residual pump reflection from the cavity, this requirement could not be met. As a patch solution, a subsequent displacement of the reflected signal was implemented by means of an asymmetric beamsplitter. An interference visibility of 97% was achieved between the reflected signal and the strong displacement beam, but a sufficiently stable operation of the combined system was never realized. Eventually, the SolstiS laser was identified as the culprit. As mentioned in Section 12.2.1 the intracavity étalon of the laser is stabilized by a dither lock, phase modulating the light at a factory-set frequency of 21 kHz. Despite our efforts to notch out resonances in the locking signal for the cavity a strong component from the dither remained and caused an insufficient stabilization of the cavity resonance which in turn prohibited locking of the displacement phase.

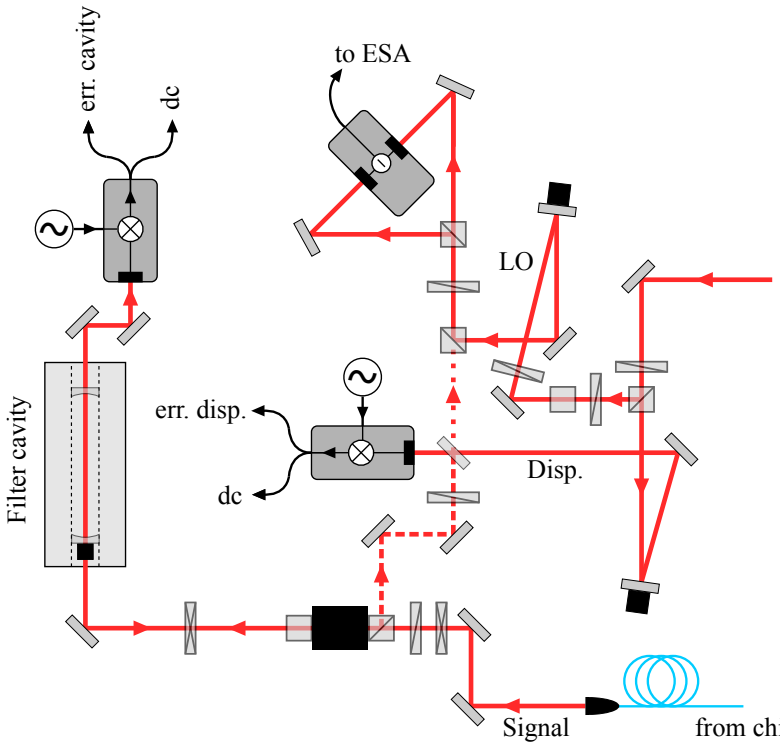

Figure 12.13: Schematic illustration of the experimental setup for cavity and displacement assisted homodyne detection. The displacement operation was implemented by means of an asymmetric beamsplitter - Layertec #107243 (PRp(45°, 710-940 nm)=7 ± 1.5%. Two resonant photodetectors with on-board down-mixing were used to generate error signals for stabilization of the cavity resonance (PDH lock) and the displacement phase (ac lock to top of interference fringe.)

12.5.2 Take II: Heterodyne measurement

Abandoning the cavity-assisted scheme, we next implemented a heterodyne detection setup as illustrated in Fig. 12.14. This was motivated by the relaxed constraint

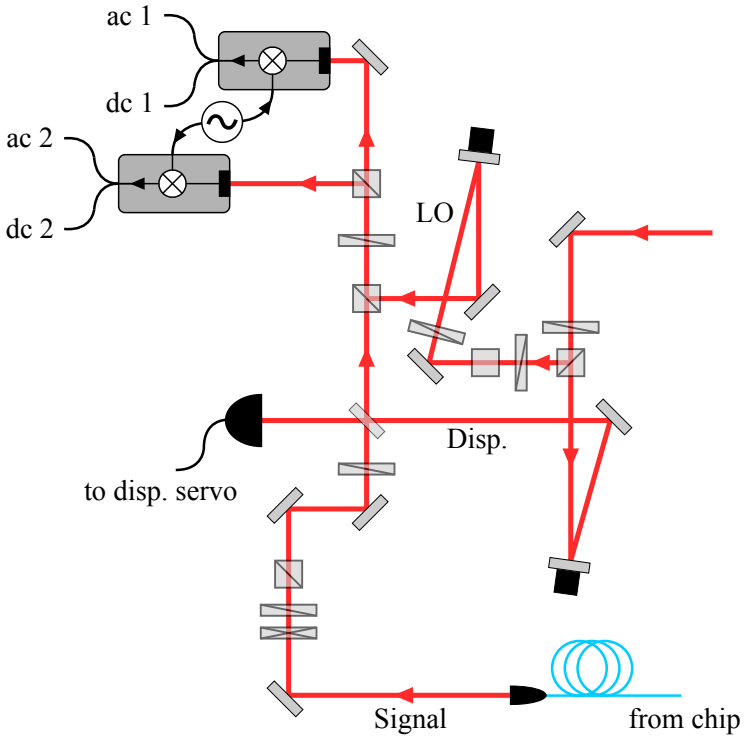

Figure 12.14: Schematic illustration of the experimental setup for heterodyne detection.

on reduction of the signal power as the scheme requires *equal* powers in signal and LO. The implementation only required minor adjustments of the optical layout, but on the electronics and data acquisition/analysis side things were complicated a bit. As described in the general presentation of heterodyne detection in Section 2.2.5, access to the individual temporal photocurrents is required in order to form the sum and difference signals. Serving that purpose two new single-diode detectors were built, also featuring on-board down-mixing of the high-pass filtered ac photocurrent. Acquisition of the temporal date was done using a digitization card[3] card and subsequent analysis and storage on a PC. To keep the total power of the equally bright signal and LO fields within the linear response regime of the detectors a displacement of the signal was still required, and with the cavity out of the setup, stabilization of the interference phase worked smoothly. A second servo was introduced for mid-fringe stabilization of the signal-LO interference. A suitable error

[3]GaGe Octopus CompuScope 8344 128 M, 50 MS/s, 4 channels.

signal was conveniently provided by the dc outputs from the heterodyne detectors.

Through a software implementation of the analysis procedure outlined in Section 2.2.5, the covariance matrix of the signal field fluctuations was evaluated on basis of the measurements, and at first glance the results were actually promissing. As an example: pumping the RTR with 150 mW, as measured immediately before the in-coupling fiber, and subsequent displacement of the output signal to a level of 5 mW the covariance matrix for the field quadrature fluctuations at a detection frequency of $\Omega = 21$ MHz was found to be:

$$\boldsymbol{\gamma} = \begin{pmatrix} 1.0702 & -0.1983 \\ -0.1983 & 0.8431 \end{pmatrix}. \tag{12.9}$$

Anti-correlations between the quadratures are evident – alluding the presence of squeezing. However, diagonalizing $\boldsymbol{\gamma}$ in order to retrieve the actual quadrature variances, we find

$$\boldsymbol{\gamma}_{diag} = \begin{pmatrix} 1.1904 & 0 \\ 0 & 0.7430 \end{pmatrix}, \tag{12.10}$$

which can only make one feel a bit uneasy since

$$\mathrm{Var}(\delta\hat{X}_1) \cdot \mathrm{Var}(\delta\hat{X}_2) = 0.884 < 1. \tag{12.11}$$

Not having the courage to challenge Heisenberg, we rather conclude that the apparent sub-minimum uncertainty state is a consequence of an insufficient determination of the shot noise level in the experiment. The heterodyne scheme does not directly provide a shot noise normalized quadrature noise measurement. Instead the shot noise level pertaining to a given performed measurement has to be evaluated afterwards – using the *exact* same power levels as for the actual measurement. In our case this was done by first far-detuning the signal from the RTR to eliminate any nonlinear modification of the noise properties. LO and signal powers were then balanced to a total power equal to the previously used, and the measurement was performed. The resulting covariance matrix was used for normalization. This procedure does not provide a very robust and reliable determination of the shot noise level and that precludes an unambiguous demonstration of squeezing unless a very strong reduction of the noise is achieved. On that basis the heterodyne setup was decommissioned.

12.5.3 Take III: Self homodyne measurement

The so-far last attempt to realize a suitable state interrogation method is a scheme combining self homodyne detection with a scanning-phase displacement operation, as illustrated in Fig. 12.15. By choosing the displacement beam to be only slightly larger in amplitude than the signal the resulting state, as the phase ϕ_{disp} is scanned through, will in a certain region of phase space have a largely reduced amplitude, given by the classical phasor sum of the interfering carrier components. The sideband fluctuation state of the signal is unaffected by the operation an maintain a

constant phase relative to the phase space frame. Assuming a weak Kerr-squeezed input signal, self homodyne measurement of the displaced signal will within the low-power region project out both the amplitude and phase quadratures, corresponding to positions (3.) and (4.), respectively, in Fig. 12.15. Our experimental implementation of the scheme is illustrated in Fig. 12.16.

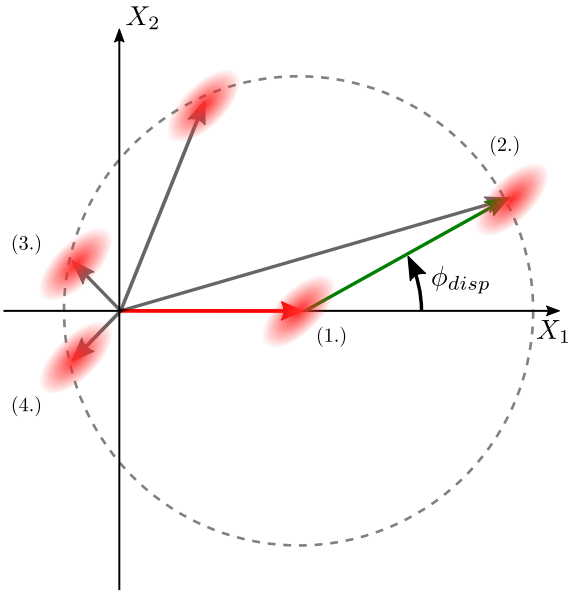

Figure 12.15: The principle of displacement assisted self homodyne detection. The initial signal (1.; red) is interfered with a displacement beam (green) of slightly larger amplitude, resulting in a displacement of the signal fluctuation state by an amount given by the phasor sum of the interfering field amplitudes (2.; grey). As the displacement phase ϕ_{disp} is scanned the resulting state describes an off-center circle in phase space, and in a small region the amplitude is largely reduced compared to the initial signal. Assuming a weakly Kerr-squeezed signal input with a squeezing phase $\theta_s = -\pi/4$, self homodyne detection of the phase-scanned displaced state will for certain phases project out the the squeezed (3.) and anti-squeezed (4.) quadratures.

The main difficulty about the scheme is the large high-power part of the scan cycle (1. and 4. quadrant of the phase space in Fig. 12.15). In this region the resulting signal power is much larger than what the detectors can withstand, causing saturation or even permanent damage. The problem was resolved by inserting a home-built protection shutter[4] following the displacement beamsplitter, that would block the signal beam conditioned on reaching a set threshold power in the other output of the displacement beamsplitter. Data acquisition was done by time-domain sampling

[4]The device was built from an old laptop hard disk drive exploiting the fast motion of the actuator arm. Information about this type of shutter can be found on the homepage of the Atom Optics group at The University of Melbourne `http://optics.ph.unimelb.edu.au/atomopt/shutter/shutter.html` or in [115].

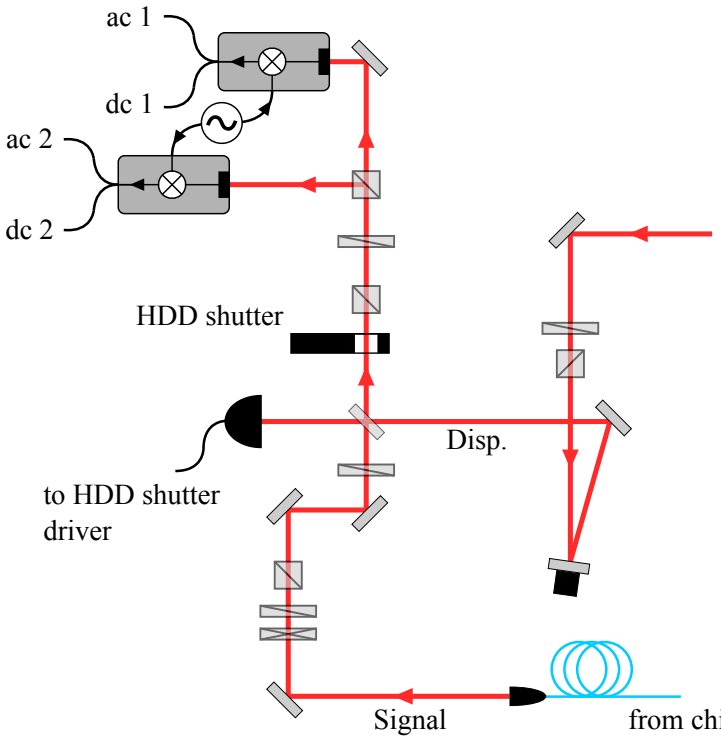

Figure 12.16: Schematic illustration of the experimental setup for self homodyne detection. The setup largely resembles that used for heterodyne detection but now without need for an external local oscillator. A protection shutter was added after the displacement beamsplitter blocking the signal during the high-power parts of the scan. Data acquisition was performed by time-domain sampling of both the ac and dc photocurrents from both detectors.

.

of the two individual photocurrents, as in the heterodyne case, but now with the important improvement that the shot noise level is simultaneously determined, cf. Section 2.2.4.

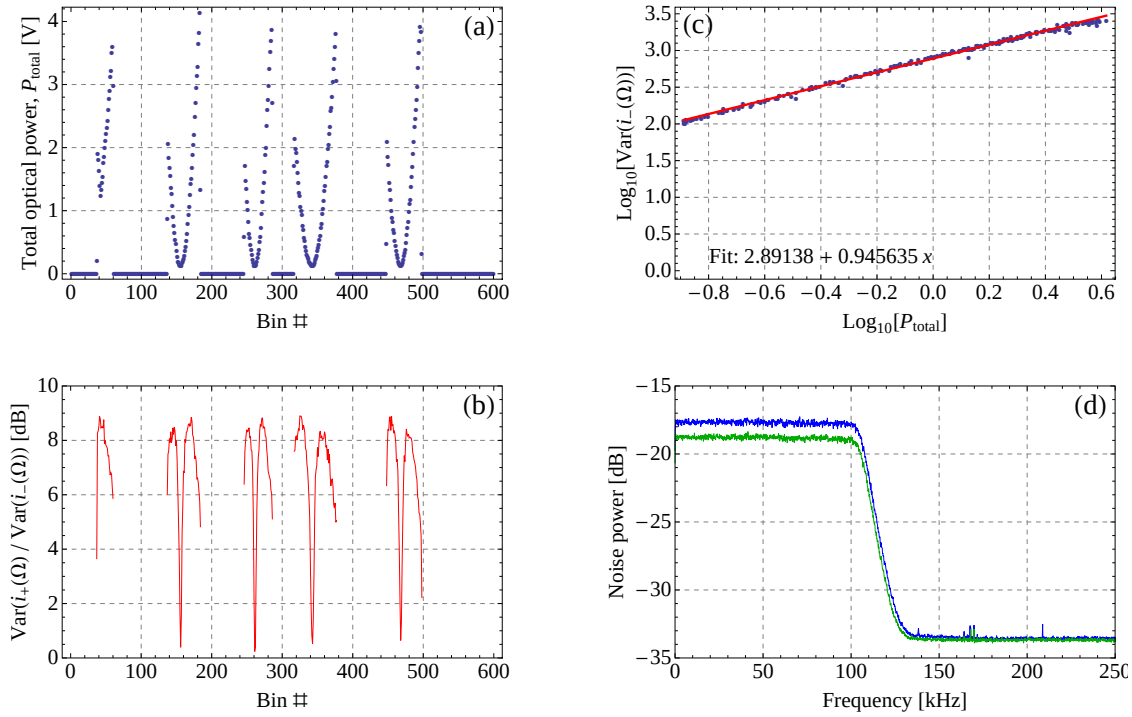

Figure 12.17: Displacement-assisted self homodyne measurement of the chip output signal at $\Omega = 29$ MHz. The signal output power from the chip was was 7.75 mW and the displacement power 9 mW. The full data set consists of 3000000 samples, which in the post processing have been analyzed in bins of 5000. The four panels show: (a) Total optical power, (b) Shot noise normalized quadrature variance, (c) Scaling of the measured shot noise with power, and (c) Diagnostics FFT of the individual ac photocurrents revealing the 100 kHz low pass filters used in both channels before the digitization card.

.

As a basis for discussing the performance of the detection scheme, an exemplary data set is shown in Fig. 12.17. Panel (a) shows the sum of the measured dc photocurrents proportional to the total power. For the particular power levels used for this measurement (7.75 mW in the signal and 9 mW in the displacement beam) only the top part of the interference fringe was bright enough to require shutter action. We observe that the shutter indeed takes out that part as required, but a delay in the shutter response causes the closing window to the asymmetrically placed with respect to the fringe. Forming the sum and difference ac photocurrents we plot in panel (b) the quantity of primary interest, namely the shot noise normalized quadrature variance. In accordance with our expectation, the variance drops towards the shot noise level at the bottom of the scan (phase in between (3.) and (4.)

in Fig. 12.15), however the strong excess noise observed for neighboring quadrature phases has so-far not been explained. As a means of diagnosing the system, we plot in panel (c) the shot noise scaling as function of total power, confirming that the measurements are shot noise limited. Likewise, an FFT of the raw ac photocurrents (panel (d)) shows no indication of excess technical noise in the setup.

An untimely exit Despite the large unexplained excess noise observed in the above data we are convinced that our search has converged towards a suitable detection scheme for interrogation of the quantum noise properties of the chip output field. The fact that the diagnostics plots do not reveal any technical causes for the noise indicates that it is a consequence of interaction with the nonlinear RTR. That is a spark of hope for eventually demonstrating generation of squeezing from an integrated source.

Sadly, pathological behavior of the pump laser started to occur in the beginning of February 2015, and it was soon realized that the system had to be shipped off for repair at the production facility where it remains situated. This unfortunate development has obviously precluded any further investigation and experimental progress on the project.

Conclusion and outlook 13

In this Part of the thesis we have been concerned with the development of a novel on-chip source of squeezed light. Achieving this goal is an important prerequisite for technological implementations of quantum enhanced optical methods, as present sources are based on bulk optics components and unfitted for integration with current electro-optical technology. But the road is rugged, and one is faced with a number of challenges in transforming state-of-the-art macroscopic systems into a micro-sized chip-based architecture.

A key objective for the work presented has been to identify a feasible device design, both in terms of performance and fabricational complexity. As presented in Chapters 10 and 11 we have addressed this task by combining a theoretical quantum noise model with extensive numerical simulations, and on that basis we have concluded that a laterally coupled silicon nitride racetrack resonator is a promising candidate for efficient integrated generation of broadband single mode quadrature squeezed light. An optimized device design has been specified in full detail, and as expected, optical loss associated with propagation in the device and interfacing are found to be the primary limiting factors to the performance of the device. We have addressed the later issue by proposing an asymmetric double layer stack waveguide geometry with inverse tapers at the chip facets as a means of robust and efficient interfacing. Numerical simulations of the structure yields a promising coupling loss of only 0.75 dB/facet. Evaluating the achievable degree of squeezing from the device we find that 4.5 dB of quantum noise reduction is within reach, assuming a linear propagation loss of 1 dB/cm.

Based on the devised design a batch of integrated silicon nitride resonators has been ordered and delivered from the foundry LioniX, and these structures have formed the basis for a subsequent experimental pursuit with the objective of demonstrating generation of squeezed light from integrated structures. This work has been the topic of Chapter 12. The linear propagation loss of the devices has been measured to be at best 1.3 dB/cm, but what is more critical is that the coupling loss was found to be 2-3 dB/facet, posing a major limitation to the device feasibility.

As discussed at length, interrogation of the chip output field noise properties has been a challenging affair, and so far squeezing has not been observed. The main source of the challenge lies in the process by which squeezing is generated in the device. Silicon nitride is a Kerr media, and the nonlinear process responsible for generation of single mode squeezing is degenerate self-phase modulation of the

pump field. The resulting squeezing resides as correlated sidebands at rf frequencies around the bright pump, and efficient separation of the two parts has turned out not to be straightforward. A number of detection strategies have been investigated and we have finally concluded that the best suited solution for our present setup is a self homodyne scheme assisted by a displacement operation on the signal field. This circumvents the need for separating pump and sidebands, and allows – in principle – for a full tomography of the signal quadrature noise.

Despite not having reached the set goal for the project, much valuable knowledge on the challenges of integrating continuous variable quantum light sources has been gained, and that will hopefully serve as a stepping stone for future continuation of the research. So far, only one nonlinear host material out many has been explored, and it is likely that silicon nitride is not the optimal choice. An interesting alternative to explore would be Hydex glass showing a propagation loss below 0.06 dB/cm. The nonlinearity is about a factor of 10 lower than for silicon nitride, but strong nonlinear interactions in resonant Hydex structures similar to the ones considered here has already been demonstrated in the telecom range [103]. Being a Kerr media as well, going to Hydex does not resolve the state interrogation problem. To this end one might consider exploring the feasibility of microresonators fabricated from second order nonlinear materials as used in ordinary parametric down-conversion squeezed light sources. In this way one would benefit both from the much stronger nonlinearities and the large frequency separation between pump and converted fields. Worth mentioning in this context is, that second harmonic generation has recently been demonstrated in high Q lithium niobate microdisk resonators [132].

Appendices

Rotating frame transformation A

It is often convenient to transform a Hamiltonian operator $\hat{H}$ into a frame rotating at a particular frequency. In this appendix we derive the general unitary transformation that accomplishes this and its transformation of the annihilation and creation operators.

To do so, we consider the Schrödinger equation

$$i\hbar\frac{d}{dt}|\Psi\rangle = \hat{H}|\Psi\rangle. \tag{A.1}$$

Transforming the Hamiltonian into a frame rotating at frequency ω' is equivalent to a transformation into the interaction picture where the interaction Hamiltonian is that of the free field at the rotating frame frequency, i.e. $\hat{H}' = \hbar\omega'\hat{a}^\dagger\hat{a}$. The corresponding unitary transformation operator is

$$\hat{U} = e^{i\hat{H}'t/\hbar} = e^{i\omega' t\hat{a}^\dagger\hat{a}}. \tag{A.2}$$

We now apply this transformation to the Schrödinger equation, through the action of $\hat{U}$ on the wavefunction: $|\tilde{\Psi}\rangle = \hat{U}|\Psi\rangle$.

$$i\hbar\frac{d}{dt}|\Psi\rangle = \hat{H}|\Psi\rangle \xrightarrow{\hat{U}} i\hbar\frac{d}{dt}\left(\hat{U}^\dagger|\tilde{\Psi}\rangle\right) = \hat{H}\hat{U}^\dagger|\tilde{\Psi}\rangle \tag{A.3}$$

$$\Leftrightarrow i\hbar\left(\left(\frac{d}{dt}\hat{U}^\dagger\right)|\tilde{\Psi}\rangle + \hat{U}^\dagger\frac{d}{dt}|\tilde{\Psi}\rangle\right) = \hat{H}\hat{U}^\dagger|\tilde{\Psi}\rangle \tag{A.4}$$

Rearranging terms and multiplying by $\hat{U}$ from the left we get

$$i\hbar\frac{d}{dt}|\tilde{\Psi}\rangle = \hat{U}\hat{H}\hat{U}^\dagger|\tilde{\Psi}\rangle - i\hbar\hat{U}\left(\frac{d}{dt}\hat{U}^\dagger\right)|\tilde{\Psi}\rangle \tag{A.5}$$

$$= \hat{U}\left(\hat{H} - i\hbar\frac{d}{dt}\right)\hat{U}^\dagger|\tilde{\Psi}\rangle \tag{A.6}$$

$$= \tilde{H}|\tilde{\Psi}\rangle. \tag{A.7}$$

Thus, the rotating frame Hamiltonian is given by

$$\tilde{H} = \hat{U}\left(\hat{H} - i\hbar\frac{d}{dt}\right)\hat{U}^\dagger. \tag{A.8}$$

We can now derive the effect of the rotating frame transformation on the annihilation and creation operators, using the general Baker-Hausdorf operator lemma:

$$e^{i\lambda\hat{A}}\hat{B}e^{-i\lambda\hat{A}} = \hat{B} + i\lambda[\hat{A},\hat{B}] + \frac{(i\lambda)^2}{2!}[\hat{A},[\hat{A},\hat{B}]] + ... \tag{A.9}$$

For the annihilation operator we get

$$\hat{U}\hat{a}\hat{U}^\dagger = e^{i\omega' t\hat{a}^\dagger\hat{a}}\hat{a}e^{-i\omega' t\hat{a}^\dagger\hat{a}} \tag{A.10}$$

$$= \hat{a} + (-i\omega' t)\hat{a} + \frac{1}{2!}(-i\omega' t)\hat{a} + ... \tag{A.11}$$

$$= e^{-i\omega' t}\hat{a}, \tag{A.12}$$

and similarly for the creation operator

$$\hat{U}\hat{a}^\dagger\hat{U}^\dagger = \left(\hat{U}\hat{a}\hat{U}^\dagger\right)^\dagger = e^{i\omega' t}\hat{a}^\dagger. \tag{A.13}$$

Using the above results and the unitarity property of the transformation operator we find that the number operator is unaffected by the transformation:

$$\hat{U}\hat{n}\hat{U}^\dagger = \hat{U}\hat{a}^\dagger\hat{a}\hat{U}^\dagger = \hat{U}\hat{a}^\dagger\hat{U}^\dagger\hat{U}\hat{a}\hat{U}^\dagger = \hat{n}. \tag{A.14}$$

This is of course expected as the rotating frame transformation is just a shift of the energy zero point, which only affects the phases and not the number of excitations.

Derivation of the output squeezing spectrum

B

This Appendix is intended as a supplement to Chapter 10 providing a fully detailed derivation of the output fluctuation quadrature spectrum (10.17), formally defined by

$$S_\theta(\Omega) = 1 + :S_\theta(\Omega): \tag{B.1}$$

$$= 1 + \int d\Omega' \langle : \delta\hat{X}_\theta(\Omega)\delta\hat{X}_\theta(\Omega') : \rangle, \tag{B.2}$$

where the generalized output field fluctuation quadrature is

$$\delta\hat{X}_\theta(\Omega) = \delta\hat{a}_{out}(\Omega)e^{-i\theta} + \delta\hat{a}^\dagger_{out}(-\Omega)e^{i\theta}. \tag{B.3}$$

As onset for the derivation we will take the expression in (10.12) for the output field fluctuations

$$\boldsymbol{\delta a}_{out}(\Omega) = [\mathbf{M} - (\gamma - i\Omega)\mathbf{I}_2]^{-1} \times \Big([\mathbf{M} + (\gamma_c - \gamma_0 + i\Omega)\mathbf{I}_2]\, \boldsymbol{\delta a}_{in}(\Omega) + 2\sqrt{\gamma_0\gamma_c}\boldsymbol{\delta b}(\Omega) \Big). \tag{B.4}$$

with the system matrix given by

$$\mathbf{M} = -i \begin{pmatrix} 2|\epsilon| - \Delta_p & \epsilon \\ -\epsilon^* & -2|\epsilon| + \Delta_p \end{pmatrix} \tag{B.5}$$

Output mode Carrying out the matrix multiplications in (10.12) we find for the output mode fluctuations

$$\delta\hat{a}_{out}(\Omega) = \frac{1}{D(\Omega)} \left[N_1(\Omega)\delta\hat{a}_{in}(\Omega) + C_1\delta\hat{a}^\dagger_{in}(-\Omega) + N_2(\Omega)\delta\hat{b}_{in}(\Omega) + C_2\delta\hat{b}^\dagger_{in}(-\Omega) \right], \tag{B.6}$$

where we have introduced the abbreviated quantities

$$\begin{aligned} N_1(\Omega) &= -\left(\gamma + i(\Delta_p - \Omega)\right)\left(\gamma_c - \gamma_0 + i(\Delta_p + \Omega)\right) \\ &\quad +2i|\epsilon|(\gamma + \gamma_c - \gamma_0 + 2i\Delta_p) + 3|\epsilon|^2 \qquad \text{(B.7)} \\ N_2(\Omega) &= -2\sqrt{\gamma_0\gamma_c}\left(\gamma + i(\Delta_p - \Omega) - 2i|\epsilon|\right) \qquad \text{(B.8)} \\ C_1 &= i(\gamma + \gamma_c - \gamma_0)\epsilon \qquad \text{(B.9)} \\ C_2 &= 2i\epsilon\sqrt{\gamma_0\gamma_c} \qquad \text{(B.10)} \\ D(\Omega) &= \Delta^2 + (\gamma - i\Omega)^2 - 4\Delta_p|\epsilon| + 3|\epsilon|^2 \qquad \text{(B.11)} \end{aligned}$$

Second-order moments The quantity of interest for deriving the squeezing spectrum (B.2) is the normal-ordered second-order moment

$$\begin{aligned} \langle : \delta\hat{X}_\theta(\Omega)\delta\hat{X}_\theta(\Omega') : \rangle &= \langle : \delta\hat{a}_{out}(\Omega)\delta\hat{a}_{out}(\Omega')e^{-2i\theta} + \delta\hat{a}_{out}(\Omega)\delta\hat{a}^\dagger_{out}(-\Omega') \\ &\quad +\delta\hat{a}^\dagger_{out}(-\Omega)\delta\hat{a}_{out}(\Omega') + \delta\hat{a}^\dagger_{out}(-\Omega)\delta\hat{a}^\dagger_{out}(-\Omega')e^{2i\theta} : \rangle \\ &= e^{-2i\theta}\langle\delta\hat{a}_{out}(\Omega)\delta\hat{a}_{out}(\Omega')\rangle + e^{2i\theta}\langle\delta\hat{a}^\dagger_{out}(-\Omega)\delta\hat{a}^\dagger_{out}(-\Omega')\rangle \\ &\quad +2\langle\delta\hat{a}^\dagger_{out}(-\Omega)\delta\hat{a}_{out}(\Omega')\rangle, \qquad \text{(B.12)} \end{aligned}$$

and in particular the three second-order moments of the output fields in (B.12) have to be evaluated to determine the quadrature noise spectrum. In the following we will identify the non-zero contributions to each of the three second-order moments, assuming vacuum fluctuation inputs. In this case the frequency space fluctuation correlation functions are

$$\langle\hat{a}_{in}(\Omega)\hat{a}^\dagger_{in}(\pm\Omega')\rangle = \delta(\Omega \pm \Omega'), \qquad \text{(B.13)}$$

$$\langle\hat{b}_{in}(\Omega)\hat{b}^\dagger_{in}(\pm\Omega')\rangle = \delta(\Omega \pm \Omega'). \qquad \text{(B.14)}$$

To simplify the notation we leave out the "*in*" subscripts in the following, and for the same reason we also suppress the "δ" identifying fluctuation operators.

$$\begin{aligned} &\langle\hat{a}_{out}(\Omega)\hat{a}_{out}(\Omega')\rangle \\ &\quad= \Big\langle \frac{1}{D(\Omega)}\Big(N_1(\Omega)\hat{a}(\Omega) + C_1\hat{a}^\dagger(-\Omega) + N_2(\Omega)\hat{b}(\Omega) + C_2\hat{b}^\dagger(-\Omega)\Big) \\ &\qquad\times \frac{1}{D(\Omega')}\Big(N_1(\Omega')\hat{a}(\Omega') + C_1\hat{a}^\dagger(-\Omega') + N_2(\Omega')\hat{b}(\Omega') + C_2\hat{b}^\dagger(-\Omega')\Big)\Big\rangle \\ &\quad= \frac{1}{D(\Omega)D(\Omega')}\Big\{N_1(\Omega)C_1\Big\langle\hat{a}(\Omega)\hat{a}^\dagger(-\Omega')\Big\rangle + N_2(\Omega)C_2\Big\langle\hat{b}(\Omega)\hat{b}^\dagger(-\Omega')\Big\rangle\Big\} \\ &\quad= \frac{1}{D(\Omega)D(\Omega')}\Big\{N_1(\Omega)C_1 + N_2(\Omega)C_2\Big\}\delta(\Omega + \Omega') \qquad \text{(B.15)} \end{aligned}$$

$$
\begin{aligned}
&\langle \hat{a}_{out}{}^{\dagger}(-\Omega)\hat{a}^{\dagger}_{out}(-\Omega')\rangle \\
&\quad= \Big\langle \frac{1}{D(\Omega)}\Big(N_1^*(-\Omega)\hat{a}^{\dagger}(-\Omega) + C_1^*\hat{a}(\Omega) + N_2^*(-\Omega)\hat{b}^{\dagger}(-\Omega) + C_2^*\hat{b}(\Omega)\Big) \\
&\qquad\times \frac{1}{D(\Omega')}\Big(N_1^*(-\Omega')\hat{a}^{\dagger}(-\Omega') + C_1^*\hat{a}(\Omega') + N_2^*(-\Omega')\hat{b}^{\dagger}(-\Omega') + C_2^*\hat{b}(\Omega')\Big)\Big\rangle \\
&\quad= \frac{1}{D(\Omega)D(\Omega')}\Big\{C_1^*N_1^*(-\Omega')\Big\langle\hat{a}(\Omega)\hat{a}^{\dagger}(-\Omega')\Big\rangle + N_2^*(-\Omega')C_2^*\Big\langle\hat{b}(\Omega)\hat{b}^{\dagger}(-\Omega')\Big\rangle\Big\} \\
&\quad= \frac{1}{D(\Omega)D(\Omega')}\Big\{C_1^*N_1^*(-\Omega') + N_2^*(-\Omega')C_2^*\Big\}\delta(\Omega+\Omega')
\end{aligned}
\tag{B.16}
$$

$$
\begin{aligned}
&\langle \hat{a}_{out}{}^{\dagger}(-\Omega)\hat{a}_{out}(\Omega')\rangle \\
&\quad= \Big\langle \frac{1}{D(\Omega)}\Big(N_1^*(-\Omega)\hat{a}^{\dagger}(-\Omega) + C_1^*\hat{a}(\Omega) + N_2^*(-\Omega)\hat{b}^{\dagger}(-\Omega) + C_2^*\hat{b}(\Omega)\Big) \\
&\qquad\times \frac{1}{D(\Omega')}\Big(N_1(\Omega')\hat{a}(\Omega') + C_1\hat{a}^{\dagger}(-\Omega') + N_2(\Omega')\hat{b}(\Omega') + C_2\hat{b}^{\dagger}(-\Omega')\Big)\Big\rangle \\
&\quad= \frac{1}{D(\Omega)D(\Omega')}\Big\{C_1^*C_1\Big\langle\hat{a}(\Omega)\hat{a}^{\dagger}(-\Omega')\Big\rangle + C_2^*C_2\Big\langle\hat{b}(\Omega)\hat{b}^{\dagger}(-\Omega')\Big\rangle\Big\} \\
&\quad= \frac{1}{D(\Omega)D(\Omega')}\Big\{C_1^*C_1 + C_2^*C_2\Big\}\delta(\Omega+\Omega')
\end{aligned}
\tag{B.17}
$$

Denominator Since $D(-\Omega) = D(\Omega)^*$ the common denominator for the three moments is given by

$$
|D(\Omega)|^2 = \Big[\Delta_p^2 + \gamma^2 - \Omega^2 - 4\Delta_p|\epsilon| + 3|\epsilon|^2\Big]^2 + 4\gamma^2\Omega^2 \tag{B.18}
$$

Numerators We now evaluate the numerators, implicitly integrating over Ω and setting $\Omega = -\Omega'$ due to the δ-functions. From eqn. (B.17) we get

$$
M_1 = |C_1|^2 + |C_2|^2 = (\gamma + \gamma_c - \gamma_0)^2|\epsilon|^2 + 4|\epsilon|^2\gamma_0\gamma_c = 4\gamma_c\gamma|\epsilon|^2 \tag{B.19}
$$

For the two remaining moments (B.15) and (B.16) we observe that

$$
\langle \hat{a}_{out}(\Omega)\hat{a}_{out}(\Omega')\rangle = \langle \hat{a}^{\dagger}_{out}(-\Omega)\hat{a}^{\dagger}_{out}(-\Omega')\rangle^* \tag{B.20}
$$

Exploiting this we can write the two moments' composite contribution to the normal ordered quadrature moment as (numerator only)

$$
M_2(\Omega) = e^{-2i\theta}\{C_1N_1(\Omega) + C_2N_2(\Omega)\} + e^{2i\theta}\{C_1^*N_1^*(\Omega) + C_2^*N_2^*(\Omega)\} \tag{B.21}
$$

With the redefinitions $C_1 = i\bar{C}_1 e^{2i\phi}$ and $C_2 = i\bar{C}_2 e^{2i\phi}$, where $\{\bar{C}_1, \bar{C}_2\} \in \mathbb{R}$, (using the definition of the pump parameter) we can write

$$\begin{aligned} M_2(\Omega) &= i\bar{C}_1\Big\{e^{-2i(\theta-\phi)}N_1(\Omega) - e^{2i(\theta-\phi)}N_1^*(\Omega)\Big\} \\ &\quad + i\bar{C}_2\Big\{e^{-2i(\theta-\phi)}N_2(\Omega) - e^{2i(\theta-\phi)}N_2^*(\Omega)\Big\} \qquad \text{(B.22)} \\ &= i\bar{C}_1\Big\{\cos\Psi(N_1(\Omega) - N_1^*(\Omega)) - i\sin\Psi(N_1(\Omega) + N_1^*(\Omega))\Big\} \\ &\quad + i\bar{C}_2\Big\{\cos\Psi(N_2(\Omega) - N_2^*(\Omega)) - i\sin\Psi(N_2(\Omega) + N_2^*(\Omega))\Big\} \qquad \text{(B.23)} \end{aligned}$$

where $\Psi = 2(\theta - \phi)$. Re-grouping the expression into real and imaginary parts we get

$$\begin{aligned} M_2(\Omega) = 2\sin\Psi\Big[\bar{C}_1\mathrm{Re}\{N_1(\Omega)\} + \bar{C}_2\mathrm{Re}\{N_2(\Omega)\}\Big] \\ - 2\cos\Psi\Big[\bar{C}_1\mathrm{Im}\{N_1(\Omega)\} + \bar{C}_2\mathrm{Im}\{N_2(\Omega)\}\Big] \qquad \text{(B.24)} \end{aligned}$$

From (B.7)-(B.11) we get

$$\bar{C}_1\mathrm{Re}\{N_1(\Omega)\} + \bar{C}_2\mathrm{Re}\{N_2(\Omega)\} = -2\gamma_c|\epsilon|\Big[\gamma^2 + \Omega^2 - \Delta_p^2 + 4\Delta_p|\epsilon| - 3|\epsilon|^2\Big] \qquad \text{(B.25)}$$

$$\bar{C}_1\mathrm{Im}\{N_1(\Omega)\} + \bar{C}_2\mathrm{Im}\{N_2(\Omega)\} = -2\gamma_c|\epsilon|\Big[2\gamma(2|\epsilon| - \Delta_p)\Big] \qquad \text{(B.26)}$$

Spectrum Finally, we can insert (B.18), (B.19), (B.24), (B.25), and (B.26) into (B.12) to get the normal ordered spectral density

$$\begin{aligned} :S_\theta^{SPM}(\Omega): \;&=\; G\cdot\Big[2\gamma|\epsilon| - 2\gamma\Big[2|\epsilon| - \Delta_p\Big]\cos 2(\theta-\phi) \\ &\quad -\Big[\gamma^2 + \Omega^2 - \Delta_p^2 + 4\Delta_p|\epsilon| - 3|\epsilon|^2\Big]\sin 2(\theta-\phi)\Big] \qquad \text{(B.27)} \end{aligned}$$

where

$$G = \frac{4\gamma_c|\epsilon|}{\Big[\Delta_p^2 + \gamma^2 - \Omega^2 - 4\Delta_p|\epsilon| + 3|\epsilon|^2\Big]^2 + 4\gamma^2\Omega^2}. \qquad \text{(B.28)}$$

In applying the normal ordering operator in (B.12) the operator products are directly turned into normal ordered form without accounting for the commutation relation. As a result, a vacuum variance term has been neglected in the above normal ordered spectral density. In order to get the full measurable fluctuation spectrum this term has to be reintroduced, as done in (B.2).

Fabrication mask and chip labeling C

This Appendix contains details on the mask layout used for fabrication of the first batch of silicon nitride devices discussed in Part III. The mask layout was designed and described by U. Hoff, and the mask file was programmed by LioniX BV.

As a reference for future work, an explanation of the devised labeling convention, by which each of the 4995 individual structures resulting from the first fabrication run is uniquely identifiable, is also provided. The delivered batch included 3 full 4-inch wafers (W2269, W2315, and W2316).

C.1 Chip content and labeling convention

In the fabrication process the devices were defined by UV stepper lithography in which the target circuit design is transfered to the wafer by means of a hardmask or *reticle* that defines a "unit cell" for the design. This reticle is simply reproduced as many times as possible across the wafer area. A number of different reticles can of course be combined, but to keep the expenses down only a single one was use for this first fabrication run. The used reticle layout is illustrated in Fig. C.1 and covers a final area of 20-by-20 mm on the wafer. As visible from the full fabrication mask in Fig. C.2, the reticle was reproduced 3-by-3 times within the safe processing region of the 4-inch wafer. Each reticle reproduction is labeled [0-8] (red numbers in Fig. C.2). The reticle contains 8 chips labeled [0-7], each 5-by-10 mm in size, and the specific circuit content is identified by a second label [A-D], with the translation given in Tabel C.1. Chips 2-7 containing RTRs each host a total of 25 waveguides

Chip #	**Circuit on chip**
0D, 1D	Spiral delay-lines (0D) and straight guides only (1D)
2C, 3C	Side-coupled RTR with radius $R = 75\,\mu$m
4B, 5B	Side-coupled RTR with radius $R = 50\,\mu$m
6A, 7A	Side-coupled RTR with radius $R = 25\,\mu$m

Table C.1: Translation of chip circuit content labels.

organized in groups of 5. Each guide is identified by a number [1-25] counting from the chip label. The first group of five are straight waveguides only and for the next

4 groups of five waveguides containing RTRs the coupling length L_c is increased with increasing waveguide number through the values 2, 5, 8, 9, and 10 μm.

In order to store and retrieve data from performed characterization measurements in a reliable way, a labeling convention was introduced, enabling unambiguous identification of individual waveguides structures and their original position on the wafer. Thus, each waveguide is referred to by an ID of the form:

WAFER - RETICLE REP#/CHIP#-WAVEGUIDE#

As an example, the ID W2269-1/4B-16 refers to the 16th waveguide on chip 4B in first reticle reproduction on wafer W2269.

C.2 Reticle mask

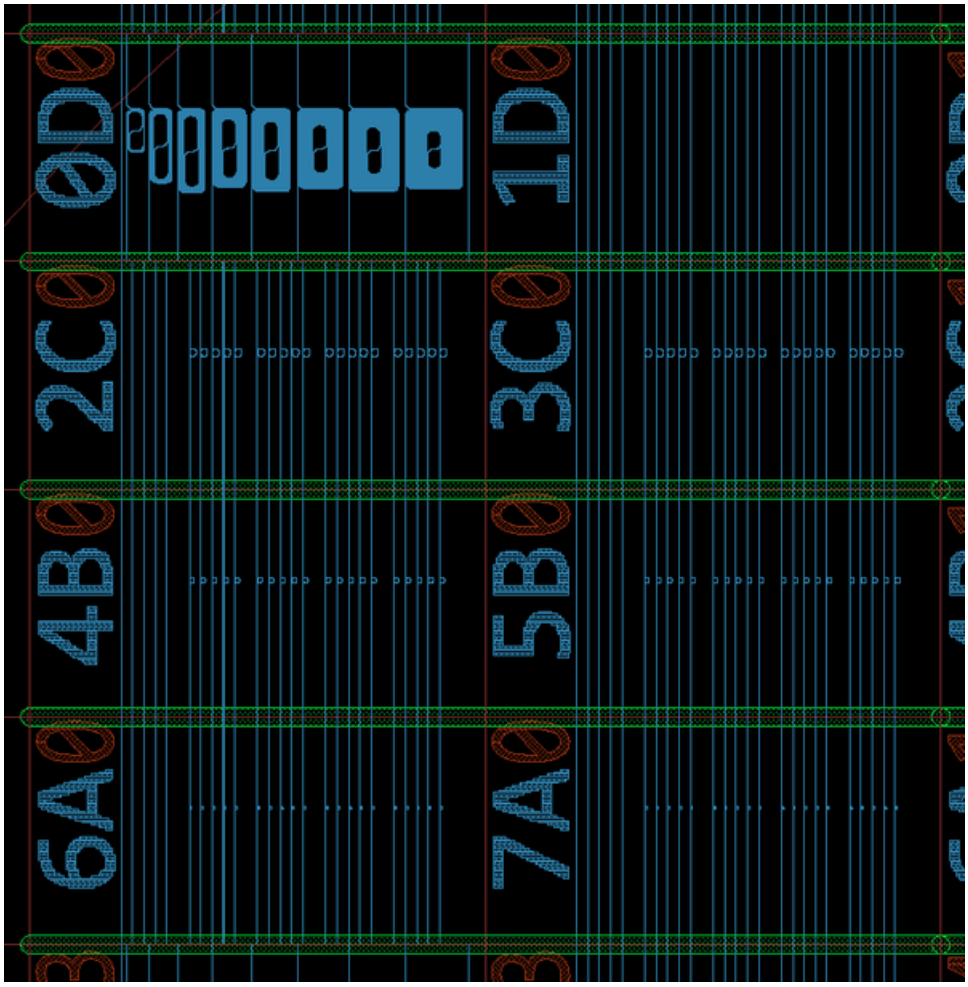

Figure C.1: Layout of the 20-by-20 mm reticle used for UV stepper lithography.

C.3 Complete wafer mask

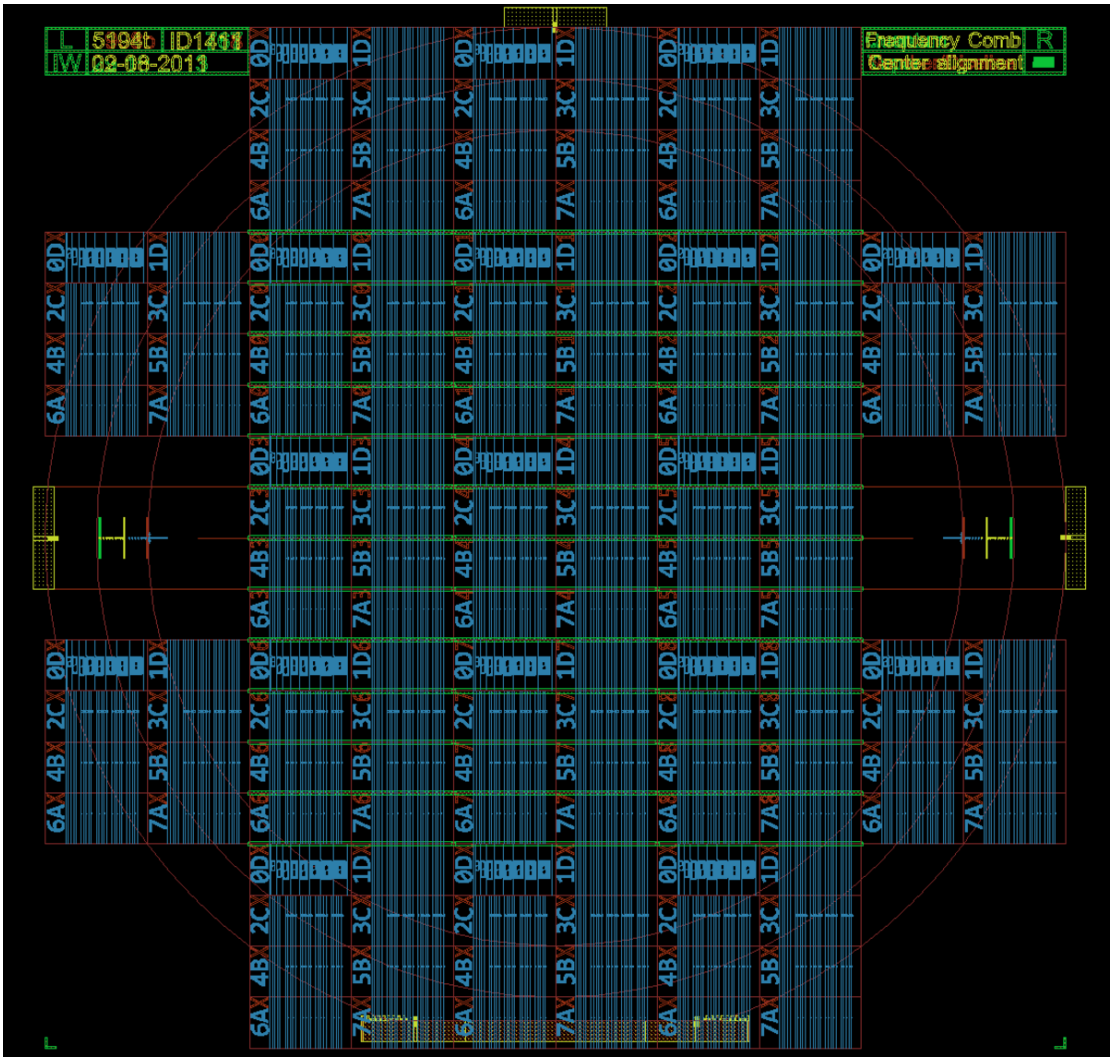

Figure C.2: Complete mask for fabrication of integrated silicon nitride structures on 4-inch wafers, containing a final total of 72 chips. Silicon nitride waveguide structures are indicated in blue, and regions where inverse tapering is applied are indicated in green.

Electronics D

This appendix contains the schematics of electronics components that have been developed for the experimental work presented in this thesis, including

- homodyne detector
- resonant detectors for error signal generation time-domain selfhomodyne and heterodyne detection
- servo controller for cavity and displacement phase stabilization
- driver for protective HDD shutter

D.1 Homodyne detector

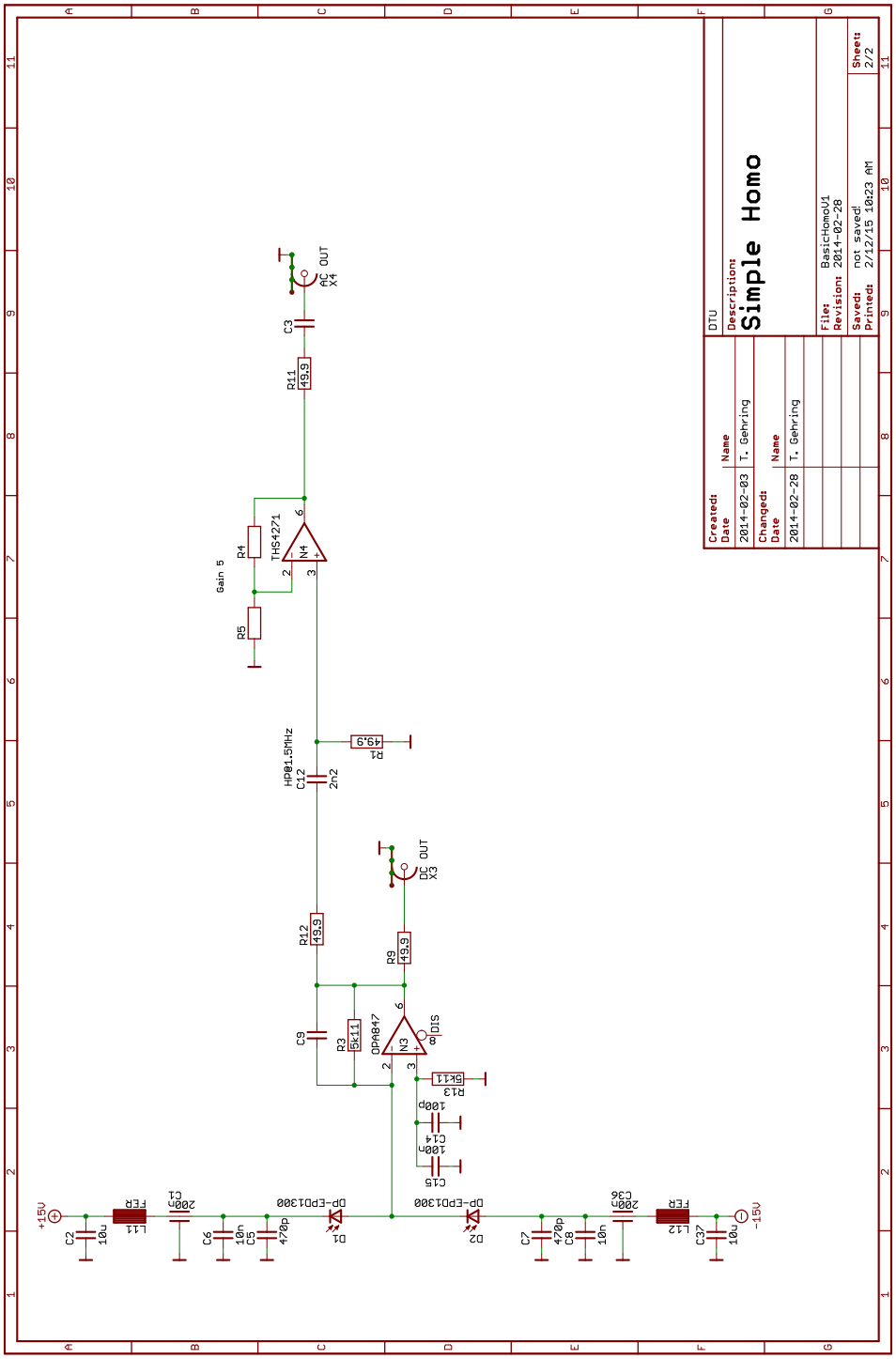

Figure D.1: Schematic of the homodynedetector electronics used for the integrated squeezer project. The circuit was developed by Tobias Gehring.

D.2 Resonant detector

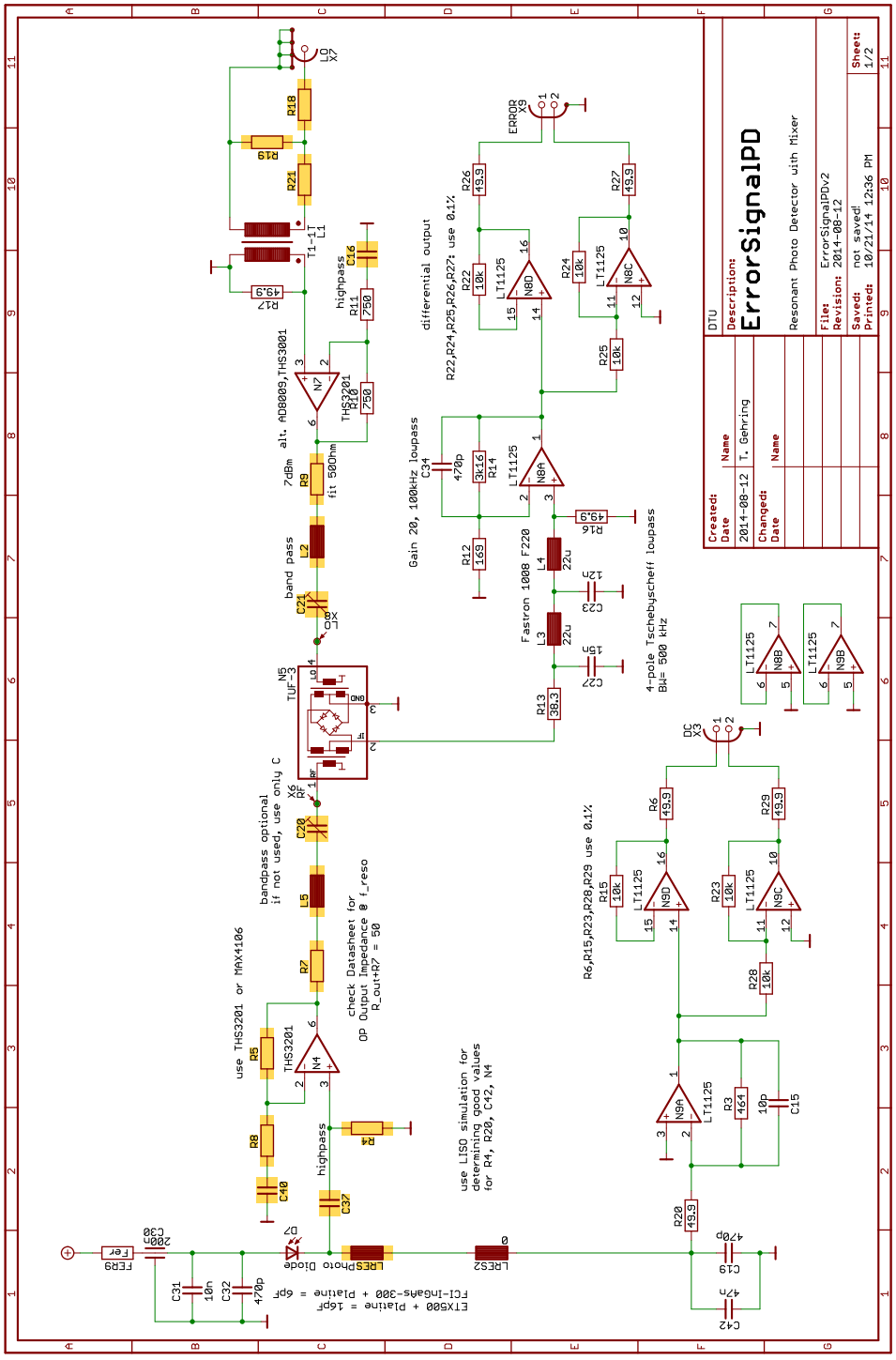

Figure D.2: Schematic of resonant photodetector. The circuit was developed by Tobias Gehring.

D.3 Servo controller

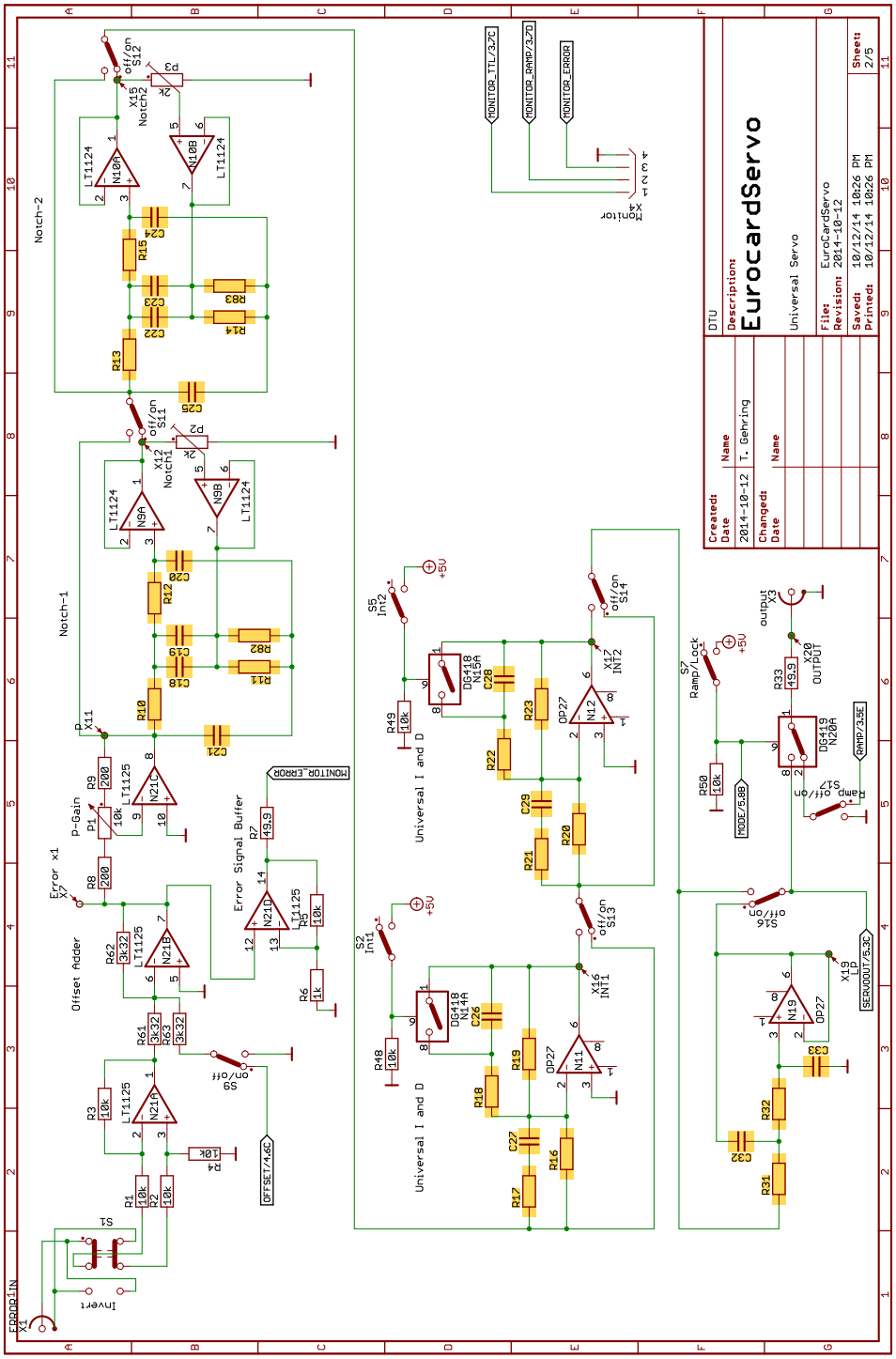

Figure D.3: Schematic of servo controller. The circuit was developed by Tobias Gehring.

D.4 Driver for HDD shutter

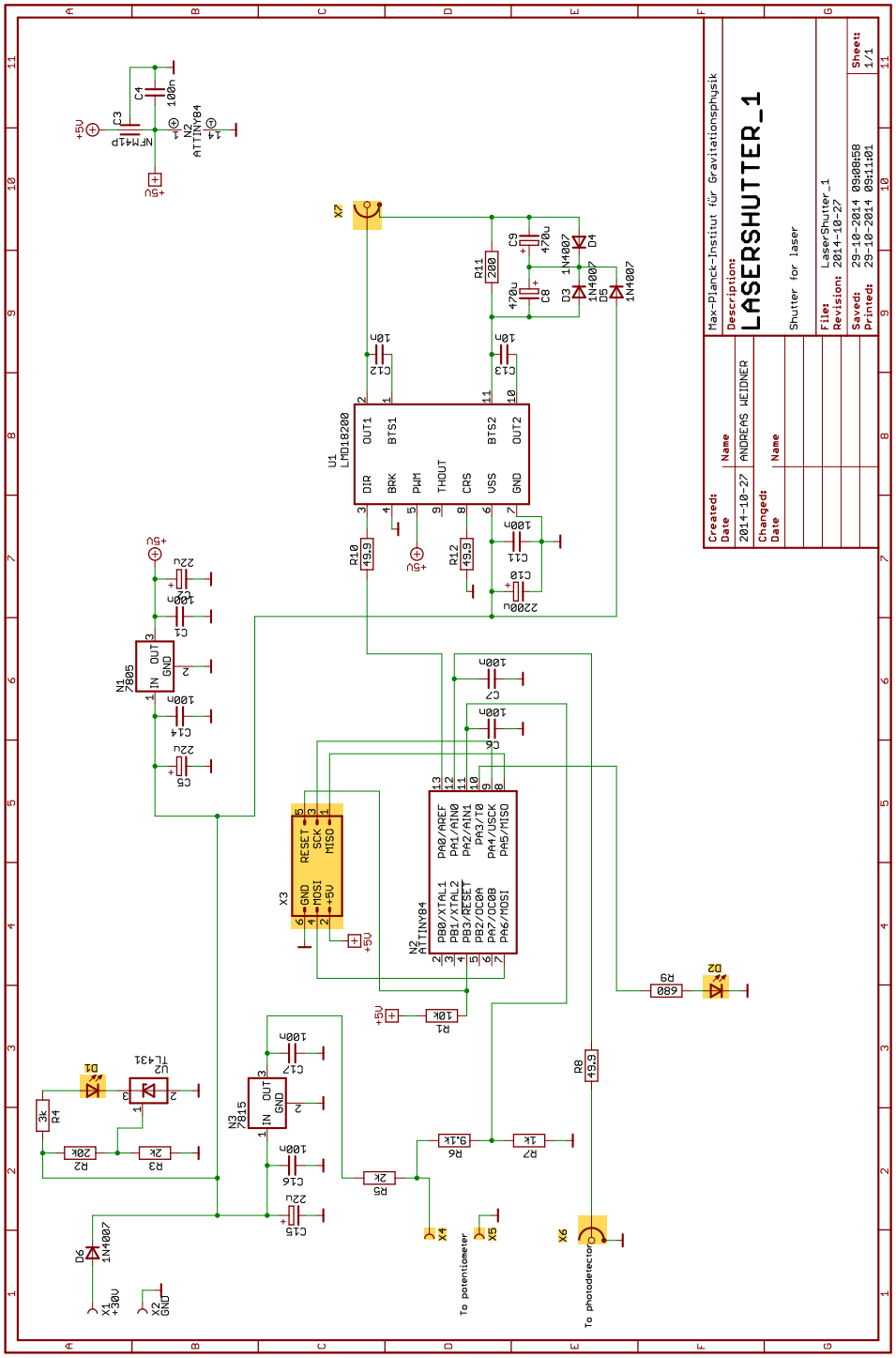

Figure D.4: Schematic for HDD shutter. The circuit was developed by Ruben Grigoryan.

Detector characterization measurements

E

In this Appendix we present characterization measurements of the homodyne detector used in Part III.

E.1 Homodyne detector (#tg-v1-1)

Summary of detector properties:

- Constructed according to the circuit schematics in Section D.1.
- The differential photocurrent is formed directly on the board and the photodiodes are mounted back-to-back in order to minimize the differential phase shifts between the photocurrents.
- Fitted with two Hamamatsu S5971 Si PIN photodiodes with a responsivity at $\lambda = 850\,\mathrm{nm}$ of $R_\lambda = 0.62\,\mathrm{A/W}$ [51], corresponding to a quantum efficiency of $\eta_{qe} = 90.1\%$.

To determine the power and frequency range in which the detector shows quantum noise limited performance, a series of shot noise measurements (vacuum at the signal input port of the homodyne detector) was made for increasing local oscillator powers in the range $160\,\mu\mathrm{W}$ to $19.9\,\mathrm{mW}$. The amplified and high-pass filtered ac output from the detector was recorded on a spectrum analyzer. A set of sample traces are plotted in Fig. E.1. The noise power approximately increase by $3\,\mathrm{dB}$ for a doubling of the total power, consistent with a proper shot noise scaling. To examine this matter further, we extract the variance in a $1\,\mathrm{MHz}$ bandwidth for a set of detection frequencies and as function of the total optical power. In a $\log - \log$ plot of the variance versus the optical power shot noise scaling is characterized by a linear trend with slope 1. The corresponding plots in Fig. E.2 show that this is indeed the case for frequencies up to $\Omega = 25\,\mathrm{MHz}$ and a total optical power below $10\,\mathrm{mW}$.

Finally, the signal clearance from electronic noise has been evaluated, and from Fig. E.3 we observe that the best performance is achieved at rather low frequencies of 5-10 MHz.

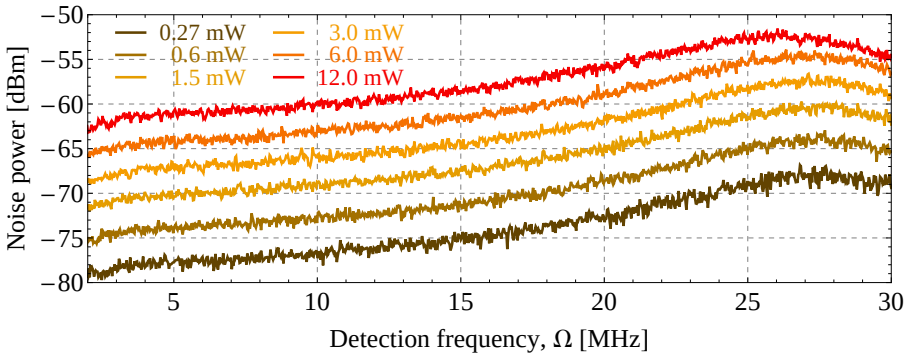

Figure E.1: Homodyne photocurrent spectra for shot noise measurements with different total powers. Data was acquired with RBW = 200 kHz and VBW = 200 kHz. Electronic noise is subtracted.

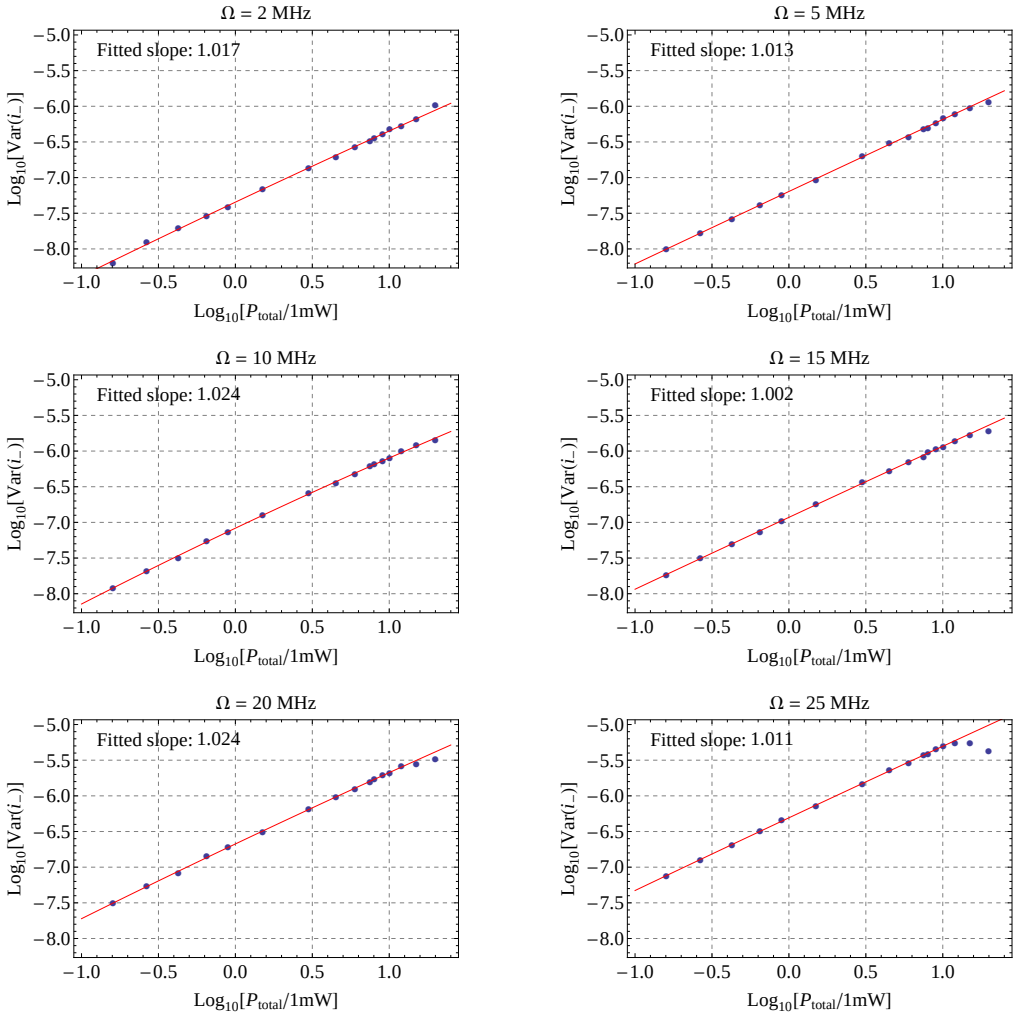

Figure E.2: Shot noise scaling as function of total optical power for different detection frequencies. The linear fit included data points up to a total power of 10 mW.

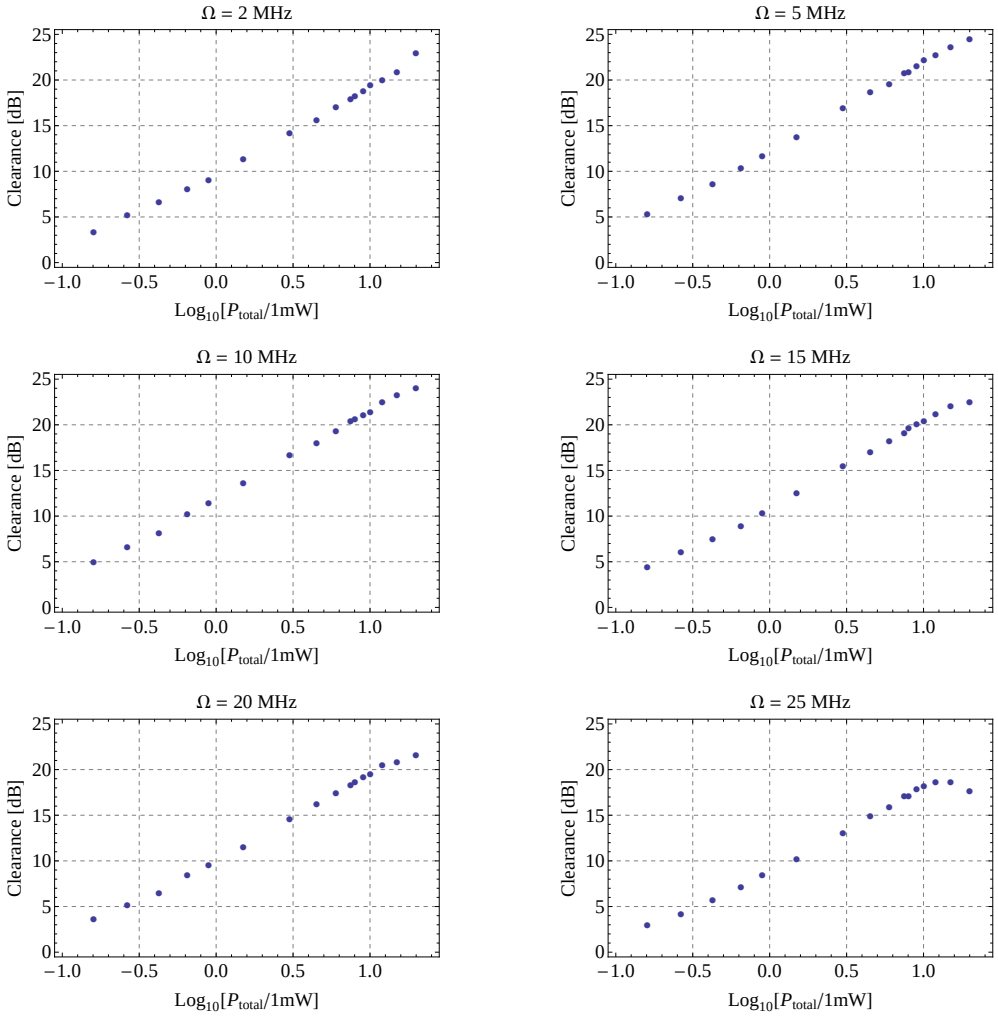

Figure E.3: Signal clearance from electronic noise as function of total optical power and detection frequency.

Bibliography

[1] J F Allen and A D Misener. Flow of Liquid Helium II. *Nature*, 141:75, 1938.

[2] M H Anderson, J R Ensher, M R Matthews, C E Wieman, and E A Cornell. Observation of Bose-Einstein Condensation in a Dilute Atomic Vapor. *Science*, 269:198–201, 1995.

[3] G Anetsberger, R Rivière, A Schliesser, O Arcizet, and T J Kippenberg. Ultralow-dissipation optomechanical resonators on a chip. *Nature Photon.*, 2: 627–633, 2008.

[4] G Anetsberger, O Arcizet, Q P Unterreithmeier, R Rivière, A Schliesser, E M Weig, J P Kotthaus, and T J Kippenberg. Near-field cavity optomechanics with nanomechanical oscillators. *Nature Phys.*, 5:909–914, 2009.

[5] G Anetsberger, E Gavartin, O Arcizet, Q P Unterreithmeier, E M Weig, M L Gorodetsky, J P Kotthaus, and T J Kippenberg. Measuring nanomechanical motion with an imprecision below the standard quantum limit. *Phys. Rev. A*, 82:061804(R), 2010.

[6] D Armani. *Ultra-High-Q Planar Microcavities and Applications*. PhD thesis, California Institute of Technology, 2005.

[7] D K Armani, T J Kippenberg, S M Spillane, and K J Vahala. Ultra-high-Q toroid microcavity on a chip. *Nature*, 421:925–928, 2003.

[8] S Ast, A Samblowski, M Mehmet, S Steinlechner, T Eberle, and R Schnabel. Continuous-wave nonclassical light with gigahertz squeezing bandwidth. *Opt. Lett*, 37:2367–2369, 2012.

[9] S Ast, M Mehmet, and R Schnabel. High-bandwidth squeezed light at 1550 nm from a compact monolithic PPKTP cavity. *Opt. Express*, 21:13572–13579, 2013.

[10] H-A Bachor and T C Ralph. *A Guide to Experiments in Quantum Optics*. Wiley-VCH, 2004.

[11] H.-A. Bachor and T.C. Ralph. Quantum noise transfer functions: A practical tool in quantum optics. In H J Carmichael, R J Glauber, and M O Scully, editors, *Directions in Quantum Optics*, volume 561 of *Lecture Notes in Physics*, pages 313–332. Springer Berlin Heidelberg, 2001.

[12] T Bagci, A Simonsen, S Schmid, L G Villanueva, E Zeuthen, J Appel, J M Taylor, A Sørensen, K Usami, A Schliesser, and E S Polzik. Optical detection of radio waves through a nanomechanical transducer. *Nature*, 507:81–85, 2014.

[13] M Bahrami, M Paternostro, A Bassi, and H Ulbricht. Proposal for Noninterferometric Test of Collapse Models in Optomechanical Systems. *Phys. Rev. Lett.*, 112:210404, 2014.

[14] J F Bauters, M J R Heck, D D John, Barton J S, C M Bruinink, A Leinse, R G Heideman, D J Blumenthal, and J E Bowers. Planar waveguides with less than 0.1 dB/m propagation loss fabricated with wafer bonding. *Opt. Express*, 19:24090–24101, 2011.

[15] K Bergman and H A Haus. Squeezing in fibers with optical pulses. *Opt. Lett.*, 16:663–665, 1991.

[16] A J Berkley, H Xu, R C Ramos, M A Gubrud, F W Strauch, P R Johnson, J R Andersen, A J Dragt, C J Lobb, and F C Wellstood. Entangled macroscopic quantum states in two superconducting qubits. *Science*, 300:1548–1550, 2003.

[17] E D Black. An introduction to Pound-Drever-Hall laser frequency stabilization. *Am. J. Phys*, 69:79–87, 2001.

[18] N Bohr. The quantum postulate and the recent development of atomic theory. *Nature*, 121:580–590, 1928.

[19] N Bohr. Discussion with Einstein on epistemological problems in atomic physics. In P. A. Schilpp, editor, *Albert Einstein: Philosopher-Scientist*, The Library of Living Philosophers, pages 200–241. Evanston, 1949.

[20] M Borselli, T J Johnson, and O Painter. Accurate measurement of scattering and absorption loss in microphotonic devices. *Opt. Lett.*, 32:2954–2956, 2007.

[21] T Botter, D W C Brooks, N Brahms, S Schreppler, and D M Stamper-Kurn. Linear amplifier model for optomechanical systems. *Phys. Rev. A*, 85:013812, 2012.

[22] R W Boyd. *Nonlinear Optics*. Academic Press, 2008.

[23] G Breitenbach, T Müller, S F Pereira, J.-Ph Poizat, S Schiller, and J Mlynek. Squeezed vacuum from a monolithic optical parametric oscillator. *J. Opt. Soc. Am. B*, 12:2304–2309, 1995.

[24] B Brezger, L Hackermüller, S Uttenthaler, J Petschinka, M Arndt, and A Zeilinger. Matter-wave interferometer for large molecules. *Phys. Rev. Lett.*, 88:100404, Feb 2002. doi: 10.1103/PhysRevLett.88.100404.

[25] D W C Brooks, T Botter, S Schreppler, T P Purdy, N Brahms, and D M Stamper-Kurn. Non-classical light generated by quantum-noise-driven cavity optomechanics. *Nature*, 488:476–480, 2012.

[26] H Bruus and K Flensberg. *Many-Body Quantum Theory in Condensed Matter Physics*. Oxford University Press, 2004.

[27] C M Caves. Quantum-mechanical radiation pressure fluctuations in an interferometer. *Phys. Rev. Lett.*, 45:75–79, 1980.

[28] C M Caves. Quantum-mechanical noise in an interferometer. *Phys. Rev. D*, 23:1693–1708, 1981.

[29] N J Cerf, M Lévy, and G Van Assche. Quantum distribution of Gaussian keys using squeezed states. *Phys. Rev. A*, 63:052311, 2001.

[30] J Chan, T P Mayer Alegre, A H Safavi-Naeini, J T Hill, A Krause, S Gröblacher, M Aspelmeyer, and O Painter. Laser cooling of a nanomechanical oscillator into its quantum ground state. *Nature*, 478:89–92, 2011.

[31] M J Collett and C W Gardiner. Squeezing of intracavity and travelling-wave light fields produced in parametric amplification. *Phys. Rev. A*, 30:1386–1391, 1984.

[32] N Daldosso, M Melchiorri, F Riboli, M Girardini, G Pucker, M Crivellari, P Bellutti, A Lui, and L Pavesi. Comparison among various Si_3N_4 waveguide geometries grown within a CMOS fabrication pilot line. *J. Lightwave Technol.*, 22(7):1734–1740, 2004.

[33] N Daldosso, M Melchiorri, F Riboli, F Sbrana, L Pavesi, G Pucker, C Kompocholis, M Crivellari, P Bellutti, and A Lui. Fabrication and optical characterization of thin two-dimensional Si_3N_4 waveguides. *Mater. Sci. Semicond. Process.*, 7:453–458, 2004.

[34] K B Davis, M O Mewes, M R Andrews, N J van Druten, D S Durfee, D M Kurn, and W Ketterle. Bose-Einstein Condensation in a Gas of Sodium Atoms. *Phys. Rev. Lett.*, 75(22):3969–3973, 1995.

[35] F Diedrich, J C Bergquist, W M Itano, and D J Wineland. Laser Cooling to the Zero-Point Energy of Motion. *Phys. Rev. Lett.*, 62:403–406, 1989.

[36] P A M Dirac. *The Principles of Quantum Mechanics*. Oxford University Press, 1930.

[37] P D Drummond and D F Walls. Quantum theory of optical bistability. I: Nonlinear polarisability model. *J. Phys. A: Math. Gen.*, 13:725–741, 1980.

[38] A Dutt, S Manipatruni, A L Gaeta, P Nussenzveig, and M Lipson. On-chip optical squeezing. *arXiv*, page 1309.6371, 2013.

[39] T Eberle, S Steinlechner, J Bauchrowitz, V Händchen, H Vahlbruch, M Mehmet, H Müller-Ebhardt, and R Schnabel. Quantum Enhancement of the Zero-Area Sagnac Interferometer Topology for Gravitational Wave Detection. *Phys. Rev. Lett.*, 104:251102, 2010.

[40] M Ferrera, L Razzari, D Duchesne, R Morandotti, Z Yang, M Liscidini, J E Sipe, S Chu, B E Little, and D J Moss. Low-power continuous-wave nonlinear optics in doped silica glass integrated waveguide structures. *Nature Photon.*, 2:737, 2008.

[41] R P Feynman. The Development of the Space-Time View of Quantum Electrodynamics. Nobel Lecture, 1965. URL `http://www.nobelprize.org/nobel_prizes/physics/laureates/1965/feynman-lecture.html`.

[42] M Fujiwara, K Toubaru, and S Takeuchi. Optical transmittance degradation in tapered fibers. *Opt. Express*, 19(9):8596–9601, 2011.

[43] C W Gardiner and P Zoller. *Quantum Noise*. Springer-Verlag, second enlarged edition, 2000.

[44] C C Gerry and P L Knight. *Introductory Quantum Optics*. Cambridge University Press, 2008.

[45] R Ghobadi, S Kumar, B Pepper, D Bouwmeester, A I Lvovsky, and C Simon. Optomechanical Micro-Macro Entanglement. *Phys. Rev. Lett.*, 112:080503, 2014.

[46] R Ghodssi and P Lin, editors. *MEMS Materials and Processes Handbook*. Springer, 2011.

[47] R J Glauber. Coherent and Incoherent States of the Radiation Field. *Phys. Rev.*, 131:2766–2788, 1963.

[48] A Gondarenko, J Levy, and M Lipson. High confinement micron-scale silicon nitride high Q ring resonator. *Opt. Express*, 17:11366–11370, 2009.

[49] S Gröblacher, J B Hertzberg, M R Vanner, G D Cole, S Gigan, K C Schwab, and M Aspelmeyer. Demonstration of an ultracold micro-optomechanical oscillator in a cryogenic cavity. *Nature Phys.*, 5:485–488, 2009.

[50] L Hackermüller, K Hornberger, B Brezger, A Zeilinger, and M Arndt. Decoherence of matter waves by thermal emission of radiation. *Nature*, 427: 711–714, 2004.

[51] Hamamatsu. Si PIN photodiode. Datasheet. URL `http://www.hamamatsu.com/resources/pdf/ssd/s5971_etc_kpin1025e.pdf`.

[52] G I Harris, U L Andersen, J Knittel, and W P Bowen. Feedback Enhanced Sensitivity in Optomechanics : Surpassing the Parametric Instability Barrier. *Phys. Rev. A*, 85:061802(R), 2012.

[53] J Heersink, V Joss, G Leuchs, and U L Andersen. Efficient polarization squeezing in optical fibers. *Opt. Lett.*, 30(10):1192–1194, 2005.

[54] L G Helt, M Liscidini, A Farsi, S Clemmen, V Venkataraman, J S Levy, M Lipson, A L Gaeta, and J E Sipe. Quantum optics of spontaneous four-wave mixing in a silicon nitride microring resonator. In *CLEO: 2011 - Laser Applications to Photonic Applications*, OSA Technical Digest (CD). Optical Society of America, 2011, 2011. paper QWA4.

[55] T Herr, K Hartinger, J Riemensberger, C Y Wang, E Gavartin, R Holzwarth, M L Gorodetsky, and T J Kippenberg. Universal formation dynamics and noise of Kerr-frequency combs in microresonators. *Nature Photon.*, 6:480–487, 2012.

[56] L Hilico, C Fabre, S Reynaud, and E Giacobino. Linear input-output method for quantum fluctuations in optical bistability with two-level atoms. *Phys. Rev. A*, 46:4397–4405, 1992.

[57] P C D Hobbs. *Building electro-optical systems: making it all work*. Wiley, 2008. Chapter 3, footnote on p. 95.

[58] U B Hoff, B M Nielsen, and U L Andersen. An integrated source of broadband quadrature squeezed light. arXiv:quant-ph/1504.01054. Submitted to Optics Express. March 2015.

[59] U B Hoff, G I Harris, L S Madsen, H Kerdoncuff, M Lassen, B M Nielsen, W P Bowen, and U L Andersen. Quantum-enhanced micromechanical displacement sensitivity. *Opt. Lett.*, 38:1413–1415, 2013. URL `http://dx.doi.org/10.1364/OL.38.001413`.

[60] M Hossein-Zahed and K J Vahala. Observation of optical spring effect in a microtoroidal optomechanical resonator. *Opt. Lett.*, 32(12):1611–1613, 2007.

[61] K Ikeda, R E Saperstein, N Alic, and Y Fainman. Thermal and Kerr nonlinear properties of plasme-deposited silicon nitride/silicon dioxide waveguides. *Opt. Express*, 16(17):12987–12994, 2008.

[62] Innolight. Ultrastable, cw, single-frequency lasers. Product datasheet. URL `http://www.optonlaser.com/fichier/pdf_149.pdf`.

[63] M Jack, M Collet, and D Walls. Enhanced squeezing due to the influence of two instabilities. *Phys. Rev. A*, 51(4):3318–3327, 1995.

[64] J D Jackson. *Classical electrodynamics*. Wiley, 3rd edition, 2008.

[65] J Janousek. *Investigation of non-classical light and its applications in ultra-sensitive measurements*. PhD thesis, Technical University of Denmark, 2007.

[66] T Juffmann, A Milic, M Müllneritsch, P Asenbaum, A Tsukernik, J Tüxen, M Mayor, O Cheshnovsky, and M Arndt. Real-time single-molecule imaging of quantum interference. *Nature Nanotech.*, 7:297–300, 2012.

[67] B Julsgaard, A Kozhekin, and E S Polzik. Experimental long-lived entanglement of two macroscopic objects. *Nature*, 413:400, 2001.

[68] P Katipza. Viscosity of Liquid Helium below the λ-Point. *Nature*, 141:74, 1938.

[69] H Kerdoncuff. Feedback cooling of an optical microresonator. Master's thesis, Technical University of Denmark, 2012.

[70] N Kiesel, F Blase, U Delić, D Grass, R Kaltenbaek, and M Aspelmeyer. Cavity cooling of an optically levitated submicron particle. *PNAS*, 110(35): 14180–14185, 2013.

[71] T J Kippenberg and K J Vahala. Cavity Optomechanics: Back-Action at the Mesoscale. *Science*, 321(5893):1172–1176, 2008.

[72] T J A Kippenberg. *Nonlinear Optics in Ultra-high-Q Whispering-Gallery Optical Microcavities*. PhD thesis, California Institute of Technology, 2004.

[73] D Kleckner and D Bouwmeester. Sub-kelvin optical cooling of a micromechanical resonator. *Nature*, 444:75–78, 2006.

[74] H. Kogelnik. Theory of dielectric waveguides. In *Integrated Optics*, volume 7 of *Topics in Applied Physics*, pages 13–81. Springer Berlin Heidelberg, 1975.

[75] H Kogelnik and T Li. Laser Beams and Resonators. *Appl. Opt.*, 5(10):1550–1567, 1966.

[76] C Kothe, L S Madsen, U L Andersen, and G Björk. Experimental determination of the degree of polarization of a quantum state. *Phys. Rev. A*, 87: 043814, 2013.

[77] P Kürz, R Paschotta, K Fiedler, and J Mlynek. Bright Squeezed Light by Second-Harmonic Generation in a Monolithic Resonator. *Europhys. Lett.*, 24 (6):449–454, 1993.

[78] F Ladouceur and J D Love. *Silica-based Buried Channel Waveguides and Devices*. Chapman & Hall, 1996.

[79] P K Lam. *Quantum Electro-Optic Control and Squeezed Light*. PhD thesis, Australian National University, 1998.

[80] M Ø Lassen. *Investigation of Spatial Quantum Optical Effects with Applications in Quantum Information and Biophysics*. PhD thesis, Technical University of Denmark, 2007.

[81] M Lassen, A Berni, L S Madsen, R Filip, and U L Andersen. Gaussian Error Correction of Quantum States in a Correlated Noisy Channel. *Phys. Rev. Lett.*, 111:180502, 2013.

[82] K H Lee, T G McRae, G I Harris, J Knittel, and W P Bowen. Cooling and Control of a Cavity Optoelectromechanical System. *Phys. Rev. Lett.*, 104: 123604, 2010.

[83] J S Levy, A Gondarenko, M A Foster, A C Turner-Foster, A L Gaeta, and M Lipson. CMOS-compatible multiple-wavelength oscillator for on-chip optical interconnects. *Nature Photon.*, 4:37–40, 2009.

[84] B E Little, S T Chu, H A Haus, J Foresi, and J-P Laine. Microring Resonator Channel Dropping Filters. *J. Lightwave Technol.*, 15(6):998–1005, 1997.

[85] J D Love, W M Henry, W J Stewart, R J Black, S Lacroix, and F Gonthier. Tapered single-mode fibres and devices. Part 1: Adiabaticity criteria. *IEE Proc. J*, 138(5):343–354, 1991.

[86] M J Madou. *Fundamentals of Microfabrication: The Science of Miniaturization*. CRC Press, Second edition, 2002.

[87] L S Madsen. *Quantum information processing with mesoscopic photonic states*. PhD thesis, Technical University of Denmark, 2012.

[88] L S Madsen, A Berni, M Lassen, and U L Andersen. Experimental Investigation of the Evolution of Gaussian Quantum Discord in an Open System. *Phys. Rev. Lett.*, 109(030402), 2012.

[89] L S Madsen, V C Usenko, M Lassen, R Filip, and U L Andersen. Continuous variable quantum key distribution with modulated entangled states. *Nat. Commun.*, 3(1083), 2012.

[90] L Mandel and E Wolf. *Optical Coherence and Quantum Optics*. Cambridge University Press, 1995.

[91] M McGovern. Optical Microcavities and Coupling Methods. Bachelor thesis, University of Otago, 2006.

[92] M Mehmet, H Vahlbruch, N Lastzka, K Danzmann, and R Schnabel. Observation of squeezed states with stong photon-number oscillations. *Phys. Rev. A*, 81:013814, 2010.

[93] K W Murch, K L Moore, S Gupta, and D M Stamper-Kurn. Observation of quantum-measurement backaction with an ultracold atomic gas. *Nature Phys.*, 4:561–564, 2008.

[94] M A Nielsen and I L Chuang. *Quantum Computation and Quantum Information*. Cambridge University Press, 2000.

[95] S Nimmrichter, K Hornberger, and K Hammerer. Optomechanical Sensing of Spontaneous Wave-Function Collapse. *Phys. Rev. Lett.*, 113:020405, 2014.

[96] Y Okawachi, K Saha, J S Levy, Y H Wen, M Lipson, and A L Gaeta. Octave-spanning frequency comb generation in a silicon nitride chip. *Opt. Lett.*, 36 (17):3398–3400, 2011.

[97] M G A Paris, F Illuminati, A Serafini, and S De Siena. Purity of Gaussian states: Measurement schemes and time evolution in noisy channels. *Phys. Rev. Lett.*, 68:012314, 2003.

[98] K Petermann. *Laser Diode Modulation and Noise*. Kluwer Academic Publishers, 1988.

[99] Eagleyard Photonics. Relative intensity noise of distributed feedback laser. Application note. URL `http://www.eagleyard.com/fileadmin/downloads/app_notes/app_note_rin_1-5.pdf`.

[100] T P Purdy, R W Peterson, and C A Regal. Observation of Radiation Pressure SHot Noise on a Macroscopic Object. *Science*, 339:801–804, 2013.

[101] T P Purdy, P-L Yu, R W Peterson, N S Kampel, and C A Regal. Strong optomechanical squeezing of light. *Phys. Rev. X*, 3:031012, 2013.

[102] D Rabus. *Integrated Ring Resonators: The Compendium*. Springer Verlag, 2007.

[103] L Razzari, D Duchesne, M Ferrera, R Morandotti, S Chu, B E Little, and D J Moss. CMOS-compatible integrated optical hyper-parametric oscillator. *Nature Photon.*, 4:41–45, 2009.

[104] K F Renk. *Basics of Laser Physics*. Springer Verlag, 2012.

[105] S Reynaud, C Fabre, E Giacobino, and A Heidmann. Photon noise reduction by passive optical bistable systems. *Phys Rev A*, 40(3):1440–1446, 1889.

[106] I D Rukhlenko, M Premaratne, and G P Agrawal. Effective mode area and its optimization in silicon-nanocrystal waveguides. *Opt. Lett.*, 37(12):2295–2297, 2012.

[107] A H Safavi-Naeini and O Painter. Optomechanical Crystal Devices. In M Aspelmeyer, T J Kippenberg, and F Marquardt, editors, *Cavity Optomechanics*, Quantum Science and Technology, pages 195–231. Springer Berlin Heidelberg, 2014.

[108] A H Safavi-Naeini, J Chan, J T Hill, T P M Alegre, A Krause, and O Painter. Observation of Quantum Motion of a Nanomechanical Resonator. *Phys. Rev. Lett.*, 108(033602), 2012.

[109] A H Safavi-Naeini, S Gröblacher, J T Hill, J Chan, M Aspelmeyer, and O Painter. Squeezed light from a silicon micromechanical resonator. *Nature*, 500:185–189, 2013. doi: doi:10.1038/nature12307.

[110] J J Sakurai. *Modern Quantum Mechanics*. Addison-Wesley Publishing, Revised edition, 1994.

[111] B E A Saleh and M C Teich. *Fundamentals of Photonics*. John Wiley & Sons, 1991.

[112] A Schliesser, G Anetsberger, R Reviére, O Arcizet, and T J Kippenberg. High-sensitivity monitoring of micromechanical vibration using whispering gallery mode resonators. *New J. Phys.*, 10:095015, 2008.

[113] A Schliesser, R Reviére, G Anetsberger, O Arcizet, and T J Kippenberg. Resolved-sideband cooling of a micromechanical oscillator. *Nature Phys.*, 4: 415–419, 2008.

[114] R Schoelkopf. Noise and Quantum Measurement. Lecture note from Boulder School for Condensed Matter and Materials Physics, Physics of Mesoscopic Systems, 2005. URL `http://boulder.research.yale.edu/Boulder-2005/Lectures/Schoelkopf/Schoelkopf_Lecture_1_Final.pdf`.

[115] R E Scholten. Enhanced laser shutter using a hard disk drive rotary voice-coil actuator. *Rev. Sci. Instrum.*, 78:026101, 2007.

[116] M O Scully and M S Zubairy. *Quantum Optics*. Cambridge University Press, 1997.

[117] R M Shelby, M D Levenson, S H Perlmutter, R G DeVoe, and D F Walls. Broad-Band Parametric Deamplification of Quantum Noise in an Optical Fiber. *Phys. Rev. Lett.*, 57:691–694, 1986.

[118] A Sizmann and G Leuchs. The optical Kerr effect and quantum optics in fibers. *Progress in Optics*, 39:373–469, 1999.

[119] R. E. Slusher, L. W. Hollberg, B. Yurke, J. C. Mertz, and J. F. Valley. Observation of squeezed states generated by four-wave mixing in an optical cavity. *Phys. Rev. Lett.*, 55:2409–2412, 1985.

[120] S Spillane. *Fiber-coupled Ultra-high-Q Microresonators for Nonlinear and Quantum Optics*. PhD thesis, California Institute of Technology, 2004.

[121] W Stutius and W Streifer. Silicon nitride films on silicon for optical waveguides. *Appl. Opt.*, 16:3218–3222, 1977.

[122] A Z Subramanian, P Neutens, A Dhakal, R Jansen, T Claes, X Rottenberg, F Peyskens, S Selvaraja, P Helin, B Du Bois, K Leyssens, S Severi, P Deshpande, R Baets, and P , Van Dorpe. Low-Loss Singlemode PECVD Silicon Nitride Photonic Wire Waveguides for 532-900 nm Wavelength Window Fabricated Within a CMOS Pilot Line. *IEEE Photon J.*, 5:2202809, 2013.

[123] A Sv Sudbø. Film mode matching: a versatile numerical method for vector mode field calculations in dielectric waveguides. *Pure Appl. Opt.*, 2:211–233, 1993.

[124] X Sun, J Zheng, M Poot, C W Wong, and H X Tang. Femtogram doubly clamped nanomechanical resonators embedded in a high-q two-dimensional photonic crystal cavity. *Nano Lett.*, 12:2299–2305, 2012.

[125] J D Teufel, T Donner, M A Castellanos-Beltran, J W Harlow, and K W Lehnert. Nanomechanical motion measured with an imprecision below that at the standard quantum limit. *Nature Nanotech*, 4:820–823, 2009.

[126] J D Teufel, T Donner, D Li, J W Harlow, M S Allman, K Cicak, A J Sirois, J D Whittaker, K W Lehnert, and R W Simmonds. Sideband cooling of micromechanical motion to the quantum ground state. *Nature*, 475:359–363, 2011.

[127] The LIGO Scientific Collaboration. A gravitational wave observatory operating beyond the quantum shot noise limit. *Nature Phys.*, 7:962–965, 2011.

[128] The LIGO Scientific Collaboration. Enhanced sensitivity of the LIGO gravitational wave detector by using squeezed states of light. *Nature Photon.*, 7: 613–619, 2013.

[129] J D Thompson, B M Zwickl, A M Jayich, F Marquardt, S M Girvin, and J G E Harris. Strong dispersive coupling of a high-finesse cavity to a micromechanical membrane. *Nature*, 452:72–75, 2008.

[130] A S Villar. The conversion of phase to amplitude fluctuations of a light beam by an optical cavity. *Am. J. Phys.*, 76:922–929, 2008.

[131] D F Walls and G J Milburn. *Quantum Optics*. Springer, 1995.

[132] C Wang, M J Burek, Lin Z, V Atikian, H A amd Venkataraman, I-C Huang, P Stark, and M Lončar. Integrated high quality factor lithium niobate microdisk resonators. *Opt. Express*, 22:30924–30933, 2014.

[133] A G White, Lam P K, D E McClelland, H-A Bachor, and W J Munro. Kerr noise reduction and squeezing. *J. Opt. B: Quantum Semiclass. Opt.*, 2:553–561, 2000.

[134] M Xiao, L-A Wu, and H J Kimble. Precision Measurement beyond the Shot-Noise Limit. *Phys. Rev. Lett.*, 59:278–281, 1987.

[135] H Yonezawa, K Nagashima, and A Furusawa. Generation of squeezed light with a monolithic optical parametric oscillator: Simultaneous achievement of phase matching and cavity resonance by temperature control. *Opt. Express*, 18:20143–20150, 2010.